Analysis of Periodic and Random Capacitively-Loaded Loop (CLL) Metamaterial Structures for Antenna Enhancement Applications

John Adams Hodge II

Thesis submitted to the faculty of the Virginia Polytechnic Institute and State University
in partial fulfillment of the requirements for the degree of

Master of Science
in
Electrical Engineering

Amir I. Zaghloul, Chair
Gary S. Brown
William A. Davis

May 14, 2014
Falls Church, VA

Keywords: Metamaterials, Antennas, Random, Capacitively-Loaded Loops (CLL), Negative Refraction, Loaded Dipole

Analysis of Periodic and Random Capacitively-Loaded Loop (CLL) Metamaterial Structures for Antenna Enhancement Applications

John Adams Hodge II

ABSTRACT

After being theorized by Veselago in 1967, recent developments in metamaterials over the last two decades have allowed scientists and researchers to physically demonstrate that artificial composite media can be engineered to exhibit exotic material properties, such as negative refractive index, by exploiting features in arrays of sub-wavelength unit inclusions. These unconventional electromagnetic properties are realized through the coupling of the microscopic unit inclusions, which govern the macroscopic properties of the structure. After demonstrating that a periodic array of capacitively-loaded loop (CLL) inclusions paired with continuous wire results in negative refraction, this study performs numerical simulations to characterize random metamaterial structures. These structures consist of CLLs that are randomized in both position and orientation. In addition, this thesis introduces an innovative antenna enhancing structure consisting of capacitively-loaded loop (CLL) metamaterial elements loaded radially around a standard dipole antenna at an electrically small distance. As a result of this innovative arrangement, the dipole antenna is easily transformed into a directive mechanically scanned antenna with high realized gain. The desired directivity and gain can be tuned based on the number of radial CLL fins placed around the dipole. Interactions between the antenna and metamaterial elements result in significant enhancement of the maximum radiated field amplitude and front-to-back ratio. This innovative CLL-loaded dipole antenna is compared to the conventional Yagi-Uda antenna. The structures presented in this thesis are modeled using full-wave simulation, and one antenna structure is experimentally verified as a proof-of-concept.

Acknowledgements

Foremost, I would like to thank my advisor, Prof. Amir Zaghloul, for the continuous support of my Masters Degree study and research, and for his patience, motivation, enthusiasm, and knowledge. Besides my advisor, I would like to thank the rest of my thesis committee, Prof. Gary Brown and Prof. Bill Davis, for their assistance, support, and difficult questions.

My sincere thanks also goes to Theodore Anthony for his patience and countless hours of teaching and assistance at ARL. Without his help, I would have only been able to complete a fraction of the work that I have done.

I would also like to thank the Antenna Team at the United States Army Research Lab for their support of my research, providing technical knowledge, providing me with a year-long internship, and for allowing me to use their hardware, technical resources, and software as a guest researcher. Thank you to Steve Weiss for his technical input, sharing of antenna knowledge, and for allowing me to perform research at ARL. Thank you to Eric Adler for being my supervisor while at ARL. Thank you to Keefe Coburn, Steve Keller, Chris Milligan, and all of the others who have provided me with feedback and research ideas.

In addition to internship support by the United States Army Research Laboratory, work in this thesis was also supported by a research grant number W911NF-11-2-0050 from the Army Research Office.

Thanks to my undergraduate research advisor, Prof. Steve Cummer at Duke University, for helping to prepare me for graduate level research and teaching the course that sparked my interest in metamaterials. Also, thanks to Dr. Gaopeng Lu who spent many hours assisting and teaching me research skills during my undergraduate years.

I would like to thank my friend Reins for all of his enthusiasm and encouragement throughout the entire process.

Last but not least, I would like to thank my family, John, Sharon, and David Hodge, for their support, care, and encouragement as I pursued my degree.

Table of Contents

List of Figures

List of Tables

Chapter 1: Introduction to Wave Propagation in Complex Media

1.1 Introduction

Over the last two decades, there has been a considerable surge in interest in the scientific community for using sub-wavelength structures or inclusions to develop novel electromagnetic materials that mimic the response of known materials or provide new material response functions not conventionally found in nature. These materials are generally referred to as metamaterials because they are artificially engineered structures, which gain their electromagnetic material properties from physical structure as opposed to intrinsic material composition. Much of the previous work done on metamaterials has focused on developing and understanding the fundamental physics of certain metamaterial structures [1, 2, 3, 4, 5]. Recently, a shift has occurred, and the focus of many research efforts in metamaterials is now driven by the demand for practical engineering applications for next generation devices, especially within the defense and communications industries [6]. In the field of electromagnetics, metamaterials tend to be classified as artificial dielectrics or complex media.

One of the materials that can be created in nature is plasma, which can exhibit negative permittivity. Plasma is an ionized gas of which a significant number of its charged particles interact strongly with electromagnetic fields and make it electrically conductive [7]. With metamaterials, the goal is to use microscopic inclusions to mimic and realize similar interactions with the electromagnetic fields. One of the major goals of metamaterial research is to physically realize double negative (DNG) medium. Veselago showed through analytical formulation, that for wave propagation through a DNG medium, the direction of the power density flow (Poynting vector) is opposite to the wave propagation (phase vector) [7]. He referred to such materials as left-handed. These exotic properties have created much scientific interest in metamaterial research.

In this introduction, background information will be given on electromagnetic wave propagation in complex media, the behavior and realization of metamaterials, and on the retrieval techniques of constitutive parameters from complex media. The purpose of the background information in this introductory chapter is to summarize previous relevant research on metamaterials and provide a frame of reference to analyze the periodic, random, and CLL-enhanced dipole metamaterial structures presented in this thesis.

1.2 Propagation in Complex Media

As with all electromagnetic problems, the propagation of waves through a metamaterial or complex media can be defined by Maxwell's equations. Maxwell's equations in a linear media can be written in phasor form as follows

$$\begin{aligned} \nabla \times \bar{E} &= -j\omega\mu\bar{H} - \bar{M} \\ \nabla \times \bar{H} &= j\omega\mu\bar{E} + \bar{J} \\ \nabla \cdot \bar{D} &= \rho \\ \nabla \cdot \bar{B} &= 0. \end{aligned} \tag{1.1}$$

The constitutive relations are

$$\begin{aligned} \overline{D} &= \varepsilon\overline{E} \\ \overline{B} &= \mu\overline{H}. \end{aligned} \tag{1.2}$$

If the medium is source-free, linear, isotropic, and homogeneous, Maxwell's curl equations reduce in phasor form to [8]

$$\begin{aligned} \nabla \times \overline{E} &= -j\omega\mu\ \overline{H} \\ \nabla \times \overline{H} &= j\omega\varepsilon\ \overline{E}. \end{aligned} \tag{1.3}$$

This constitutes two equations and two unknowns, $\overline{E}$ and $\overline{H}$. Using both of these equations, we can deduce a single equation that will lead us to a solution to the wave equation using

$$\nabla \times \nabla \times \overline{E} = -j\omega\mu\nabla \times \overline{H} = \omega^2\mu\varepsilon\overline{E}. \tag{1.4}$$

Using vector identities to simplify, it is possible to deduce the Helmoltz equation in a source free region ($\nabla \cdot \overline{E} = 0 ; \nabla \cdot \overline{H} = 0$) as

$$\nabla^2 \overline{E} + \omega^2 \mu \varepsilon \overline{E} = 0$$
$$\nabla^2 \overline{H} + \omega^2 \mu \varepsilon \overline{H} = 0. \tag{1.5}$$

From these equations we can clearly define a lossless propagation constant

$$k = \omega \sqrt{\mu \varepsilon} \tag{1.6}$$

where k is a function of frequency (ω), electric permittivity (ε), and magnetic permeability (μ). As a product of these results, materials are commonly characterized by either the complex permittivity and permeability or by the complex refractive index and impedance.

Through a similar derivation, the propagation of an electromagnetic wave through a lossy medium can be described by its complex propagation constant

$$\gamma = \alpha + j\beta = j\omega \sqrt{\varepsilon \mu} \sqrt{1 - j \frac{\sigma}{\omega \varepsilon}}. \tag{1.7}$$

This equation fits into the wave equation as follows if we assume that the electric field only has an $\hat{x}$ component and is uniform in the x and y directions [8] such that

$$\frac{\partial^2 E_x}{dz^2} - \gamma^2 E_x = 0$$
$$E_x(z) = E^+ e^{-\gamma z} + E^- e^{+\gamma z}. \tag{1.8}$$

The imaginary component of the complex propagation, β, defines the propagation of the wave through a medium and the real part of the complex propagation constant, α, defines the rate at which the wave attenuates. A wave vector in a medium can be defined as

$$k^2 = \omega^2 \mu \varepsilon \tag{1.9}$$

where the electric field can be defined as $E = \hat{x} E_0 e^{-jkz} e^{+j\omega t}$.

Refraction at the interface between two media is described by Snell's Law, which states

$$n_1 \sin \theta_i = n_2 \sin \theta_t. \tag{1.10}$$

1.3 Classifications of Complex Media

The majority of conventional media have ε≥1 and μ≥1. The different types of complex media can be classified as follows:

Double Positive (DPS) -> +ε,+μ

Epsilon Negative (ENG) -> -ε,+μ

Mu Negative (MNG) -> +ε,-μ

Double Negative (DNG) -> -ε,-μ

If $|n| < 1.0$, the material can be used for transformation optics and cloaking because the phase velocity can be made greater than the speed of light. In this study, primarily DPS and DNG classes of metamaterials will be considered due to properties shown in Figure 1.1.

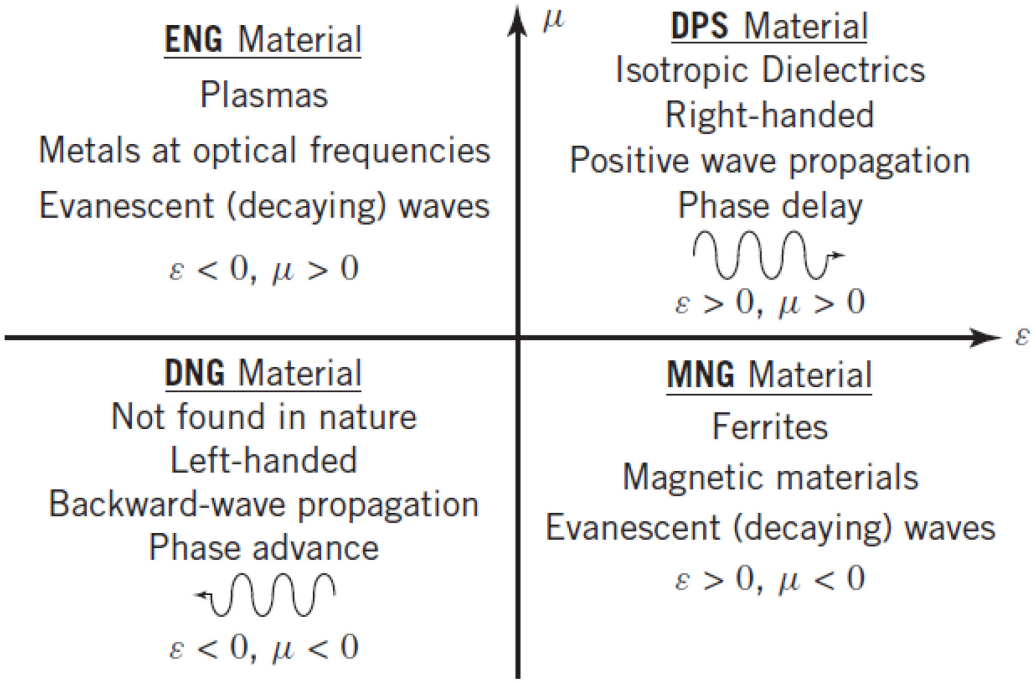

Figure 1.1: Classifications of Metamaterials [7] (used by permission from Wiley, publ.)

1.4 Metamaterial Characterization

While metamaterials have been a hot topic of electromagnetic research, there is no universally accepted definition of a metamaterial. As stated in the introduction, metamaterials are generally thought of as a class of engineered materials tuned to exhibit beneficial electromagnetic responses not conventionally found in nature [7]. One of the major distinctions of artificial metamaterials is that the material properties are derived from the physical structure of sub-wavelength inclusions or scatters, rather than the chemistry of physical materials. The material

response created by the metamaterial unit-elements is not observed in their constituent materials. The inhomogeneous metamaterial structure appears as a homogeneous slab to the incident wave when the unit inclusions, or scattering elements, that make up the metamaterial have dimensions much less than a wavelength. In the microwave frequency regime, these dimensions tend to be ~λ/10; however, some metamaterial unit scatterers can be as large as ~λ/3 depending on the shape. Metamaterial inclusions considered in this paper are resonant, such that all scattering elements are frequency scalable and can be tuned to a desired operating frequency. Just as the atomic response and polarization of atoms defines the response of convention DPS materials, the sub-wavelength unit inclusions or scattering element of a metamaterial determine its material response. The metamaterial response is defined by the composition, dimension, shape, and orientation of the inclusion or scattering element.

1.5 Summary of Important Wave-Medium Interaction Parameters

$$\text{Lossless Propagation Constant: } k = \omega\sqrt{\varepsilon\mu} \tag{1.11}$$

$$\text{Speed of Light in a Vacuum: } c = 1/\sqrt{\varepsilon_0\mu_0} \tag{1.12}$$

$$\text{Free Space Impedance: } \eta_0 = \sqrt{\mu_0/\varepsilon_0} \tag{1.13}$$

$$\text{Intrinsic Impedance of a Medium: } \eta = \frac{j\omega\mu}{\gamma} = \sqrt{\frac{\mu}{\varepsilon}} = \eta_0\sqrt{\frac{\mu_r}{\varepsilon_r}} \tag{1.14}$$

$$\text{Wavelength in a Medium: } \lambda = \frac{2\pi}{\beta} = \frac{2\pi}{\omega\sqrt{\mu\varepsilon}} = \frac{\lambda_0}{\sqrt{\mu_r\varepsilon_r}} \tag{1.15}$$

$$\text{Phase Change Over Propagation Distance: } |\Delta\phi| = |kd| = |\omega\sqrt{\mu\varepsilon}d| \tag{1.16}$$

$$\text{Phase Velocity: } v_p = \frac{\omega}{\beta} = \frac{1}{\sqrt{\mu\varepsilon}} = \frac{c}{\sqrt{\mu_r\varepsilon_r}} \tag{1.17}$$

$$\text{Group Velocity: } v_g = \frac{\partial\omega}{\partial\beta} \tag{1.18}$$

$$\text{Index of Refraction: } n = \frac{kc}{\omega} = \sqrt{\frac{\varepsilon}{\varepsilon_0}}\sqrt{\frac{\mu}{\mu_0}} \tag{1.19}$$

It is easy to see that if we have control of ε and μ of a bulk material at given frequencies, it is possible to engineer and design new devices that can manipulate incoming electromagnetic waves as desired in many ways. The rest of this thesis will focus on how metamaterials can create exotic material responses using these equations for novel applications with a special emphasis on antennas.

1.6 Lorentz's Model for Material Response

While materials are often described by a constant frequency independent value of the permittivity and permeability, in reality all material properties are frequency dependent [9]. Understanding the relationship between material polarization and the effective constitutive relations inside a material will provide a framework for understanding the dispersive material response for metamaterials and complex dielectric media. In Maxwell's equations for bound media, the material polarization is expressed in Maxwell's equations as follows

$$\vec{D} = \varepsilon_0 \vec{E} + \vec{P} = \varepsilon_0 \varepsilon_r \vec{E} + \varepsilon_0 \chi_L \vec{E} = \varepsilon_0 (1 + \chi_L) \vec{E} \tag{1.20}$$

where $\vec{E}$ is the free-space electric field response, $\vec{P}$ is the polarization response from the material, and χ_L is the electric susceptibility. From this equation, we can observe two important relations where $\vec{P} = \varepsilon_0 \chi_L \vec{E}$ and $\varepsilon = \varepsilon' - j\varepsilon'' = \varepsilon_0 \varepsilon_r = \varepsilon_0 (1 + \chi_L)$. These two equations for the electric response of a material will go a long way in aiding our understanding and ability to engineer metamaterials to give a desired frequency response. To model the response of a metamaterial, a frequency-dispersive Drude model is used to represent the negative permittivity of the infinite wires, and a frequency-dispersive Lorentz model is utilized for the representation of the negative permeability of the split-rings [4, 7, 10, 1].

In the absence of an electric field, an electron in a dielectric material will be in an unpolarized state. However, when an electric field is applied, a force is created in the direction of the electric field on the nucleus causing the electron cloud to become displaced. This electric force creates an electric dipole moment causing the material to become polarized. The displacement force of $\vec{E}$ is analogous to displacing the mass on a classical harmonic oscillator [11]. This phenomenon can be described by the Lorentz model, which is derived by a description of the electron motion in terms of a driven, damped harmonic oscillator. This model describes

the temporal response of a component of the polarization field of the medium to the same component of the electric field as

$$\frac{d^2}{dt^2}P_i + \Gamma_L \frac{d}{dt}P_i + \omega_0^2 P_i = \varepsilon_0 \chi_L E_i \tag{1.21}$$

The first term on the left accounts for the acceleration of the charges, the second accounts for the damping mechanisms of the system with damping coefficient L, and the third accounts for the restoring forces with the characteristic frequency $f_0 = \omega_0/(2\pi)$ [9]. The driving term exhibits a coupling coefficient χ_L.

In the frequency domain, where $\partial/\partial t \rightarrow j\omega$, the Equation 1.21 becomes

$$P_i(\omega) = \frac{\chi_L}{-\omega^2 + j\Gamma_L\omega + \omega_0^2}\varepsilon_0 E_i(\omega). \tag{1.22}$$

Overview of Lorentz Dielectric Response

Governing Drude Oscillator Equation

$$m\frac{\partial^2 \vec{r}}{\partial t^2} + m\Gamma\frac{\partial \vec{r}}{\partial t} + m\omega_0^2\vec{r} = -q\vec{E} \tag{1.23}$$

inertia; loss; restoring force; applied electric force

Resulting Dielectric Function

$$\varepsilon_r = 1 - \frac{\omega_p^2}{\omega_0^2 - \omega^2 - j\omega\Gamma} \tag{1.24}$$

$$\omega_p^2 = \frac{Nq^2}{\varepsilon_0 m} \tag{1.25}$$

In these equations, m is mass, Γ is the dampening factor, N is number of particles, and q is charge per particle.

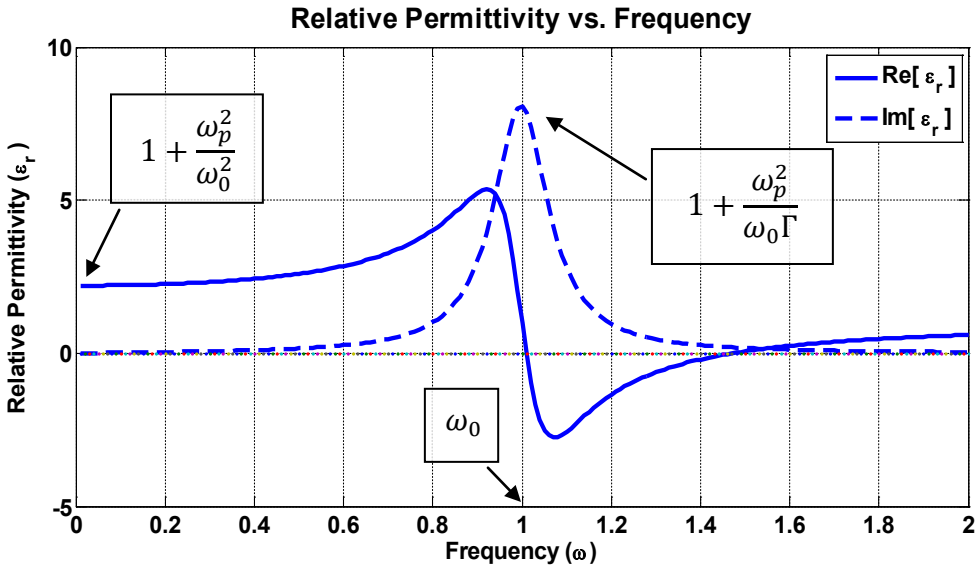

Figure 1.2: Response of Lorentz Oscillator Model for Dielectrics [11]

In the Drude model, which is used to model metals, the restoring force acting on electrons is assumed to be zero. In this case, the Lorentz model reduces to

$$\frac{d^2}{dt^2}P_i + \Gamma_D \frac{d}{dt}P_i = \varepsilon_0 \chi_D E_i \qquad \chi_{e,\text{Drude}}(\omega) = \frac{\chi_D}{-\omega^2 + j\Gamma_D \omega} \tag{1.26}$$

where the couple coefficient is represented by the plasma frequency as defined by $\chi_D = \omega_p^2$. With a positive coupling coefficient, the Drude model can produce a negative real-part of permittivity if $\omega < \sqrt{\omega_p^2 - \Gamma_D^2}$.

Overview of Lorentz-Drude Response

Governing Drude Oscillator Equation

$$m\frac{\partial^2 \vec{r}}{\partial t^2} + m\Gamma\frac{\partial \vec{r}}{\partial t} + \cancel{m\omega_0^2 \vec{r}} = -q\vec{E} \tag{1.27}$$

Electrons are not bound so restoring force is zero.

Resulting Dielectric Function

$$\varepsilon_r = 1 - \frac{\omega_p^2}{\omega^2 + j\omega\Gamma} \tag{1.28}$$

$$\omega_p^2 = \frac{Nq^2}{\varepsilon_0 m} \tag{1.29}$$

In these equations, m is mass, Γ is the dampening factor, N is number of particles, and q is charge per particle.

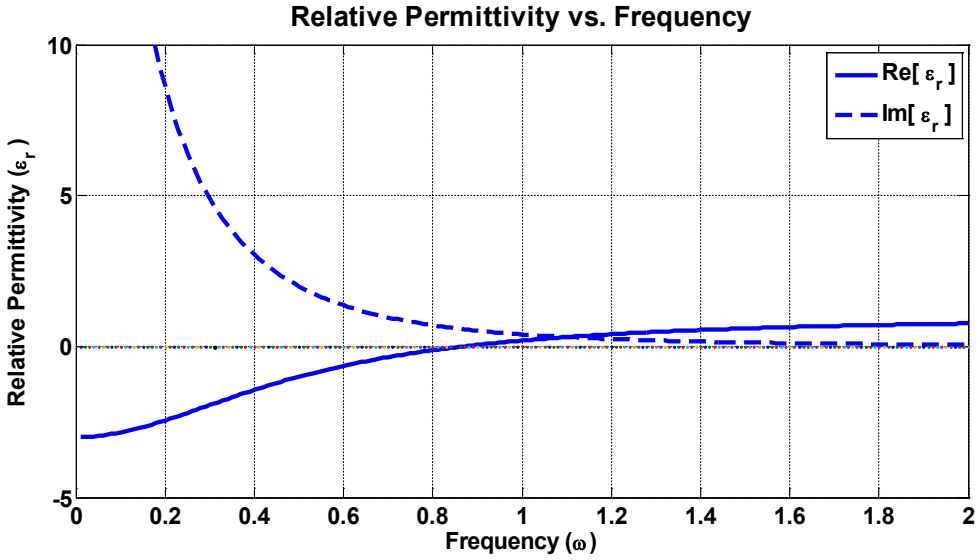

Figure 1.3: Drude Model for Metals [11]

Similar analysis for the Lorentz model can be done for magnetic material response by replacing the electric quantities with magnetic quantities. The magnetization field components Mi and the magnetic susceptibility χ_m equations are obtained from the polarization and electric susceptibility expression by replacing $E_i \rightarrow H_i$, $P_i/\varepsilon_0 \rightarrow M_i$ [9]. The frequency-dependent magnetic permeability is expressed as $\mu(\omega) = \mu'(\omega) - j\mu''(\omega) = \mu_0(1 + \chi_m(\omega))$, where $'$ indicates the real part and $''$ indicates the imaginary part. Instead of creating an electric dipole to achieve an electric response, a magnetic dipole can be used to achieve a negative permeability response. Magnetic dipoles do not exist in nature; however, it was shown by Pendry *et al.* that this response could be engineered using metamaterials [5].

Summary of Constitutive Relations

$$\varepsilon_r(\omega) = 1 + \chi_L(\omega) \rightarrow \boldsymbol{D} = \varepsilon_0 \varepsilon_r(\omega)\boldsymbol{E} \quad (1.30)$$

$$\mu_r(\omega) = 1 + \chi_m(\omega) \rightarrow \boldsymbol{B} = \mu_0 \mu_r(\omega)\boldsymbol{H} \quad (1.31)$$

Summary of Lorentz Model Results

Lorentz Dielectric Model: $\varepsilon_r(\omega) = 1 + \chi_L(\omega) = 1 + \frac{\omega_p^2}{\omega_0^2 - \omega^2 - j\omega\Gamma_L}$; $\omega_p^2 = \frac{Nq^2}{\varepsilon_0 m_e}$ (1.32)

Lorentz-Drude Model for Metals: $\varepsilon_r(\omega) = 1 + \chi_L(\omega) = 1 - \frac{\omega_p^2}{\omega^2 + j\omega\Gamma_L}$; $\omega_p^2 = \frac{Nq^2}{\varepsilon_0 m_e}$ (1.33)

where q is charge, N is number of particles per volume, and m_e is electron mass.

1.7 2TDLM Theory

A hybrid model based on the Lorentz model has been introduced in several metamaterial studies known as the two-time-derivative Lorentz metamaterial (2TDLM) model. The 2TDLM model [12, 9, 13, 14, 15] is expressed as follows:

$$\frac{d^2}{dt^2}P_i + \Gamma_L \frac{d}{dt}P_i + \omega_0^2 P_i = \varepsilon_0 \chi_\alpha \omega_p^2 E_i + \varepsilon_0 \chi_\beta \omega_p \frac{d}{dt}E_i + \varepsilon_0 \chi_\gamma \frac{d^2}{dt^2}E_i$$
$$\chi_{e,\mathrm{2TDLM}}(\omega) = \frac{\chi_\alpha \omega_p^2 + j\chi_\beta \omega_p \omega - \chi_\gamma \omega^2}{-\omega^2 + j\Gamma_L \omega + \omega_0^2} \tag{1.34}$$

This general second-order model incorporates all of the standard Lorentz model behaviors, including resonance at ω_0, while allowing for additional driving mechanisms that are important when considering time-varying phenomena [9]. This model satisfies the Kramers-Kronig relation and is causal if $\chi_\gamma > -1$.

1.8 Engineering a Negative Electric Response

In 1961, Rotman published a paper describing how artificial dielectrics could be created to give a plasma-like dispersive response [16]. As stated by Rotman himself, a plasma in the absence of dc magnetic fields is representable, from an electromagnetic viewpoint, as a lossy dielectric with a complex index of refraction whose real part is less than one. In the same paper, Rotman showed that an array of lossy metallic rods placed inside of a parallel-plate waveguide or media could produce electrical properties, such as intrinsic impendence and propagation constant, which mimic a dispersive plasmonic medium.

From this work we can conclude that an artificial media can be created consisting of an array of periodically spaced continuous metallic wires that are fixed, such that the wires align with the electric field of the incoming waves (generally assigned the x-direction). Additionally, two and three-dimensional lattices of continuous metal wires have been shown to extend the observed electric effects to waves with electric fields in the y and z directions, respectively.

Using the metallic wire lattice, an artificial material with the effective electric permittivity response modeled by a Drude dielectric can be realized. Using information given in Equation 1.35 and Figure 1.4, the radius of individual wires and spacing between wires can be tuned to give a Drude response within a desired frequency band. Below the cutoff frequency, defined by ω_p, electromagnetic waves are not able to propagate, and incident waves will experience total reflection. By following the Drude dispersion curve, the metallic wire lattice can be utilized to exhibit an effective medium response with the real part of $\varepsilon<0$.

$$\omega_{p,eff}^2 = \frac{2\pi c^2}{a^2 \ln[a/(2r)]} \tag{1.35}$$

Figure 1.4: Metal Wires to Realize Effective Negative Permittivity [11, 5, 16, 17]

1.9 Engineering a Negative Magnetic Response

While the understanding of how to engineer an artificial negative electric response with metal wires had been well understood for several decades, the same could not be said for engineering an artificial negative magnetic response for many years. Even though Veselago's 1967 prediction assumed a material with both negative effective permittivity and permeability, nobody knew how to create the artificial negative effective permeability inclusion. Using the Lorentz model, a magnetic dipole response is needed to generate $-\mu$ [11].

Metamaterial research took a giant step forward in 1999 when Sir John Pendry proposed a physically realizable method to realize negative effective permeability in the microwave regime using conductive elements [5]. Pendry was able to show that a medium composed of split metallic rings would macroscopically act as magnetic dipoles, allowing the artificial composite material to exhibit a strong magnetic response near the resonant frequency of these split-ring structures [6]. These split metallic rings are commonly known in the metamaterials community

as split ring resonators (SRRs) and will be referred to as such in this thesis. The split in the SRR creates a capacitive gap with capacitance defined by C. Similarly, the current flowing around the metallic ring creates a self-inductance defined by L. For this reason, the SRR can be analyzed as an LC circuit, which explains the resonate response as [8]:

$$f_0 = \frac{\omega_0}{2\pi} = \frac{1}{2\pi\sqrt{LC}} \tag{1.36}$$

Due to the resonant response, large currents flow through the loop and a strong magnetic field is generated [6]. A magnetic dipole in generated due to the current creating magnetic polarizibility. Using the SRR as an engineering tool, we can design the size, shape, and orientation of an SRR or a similar conducting loop to design magnetic dispersion curves for specific applications. The frequency response can be tuned to achieve either positive or negative values of μ over a given frequency range.

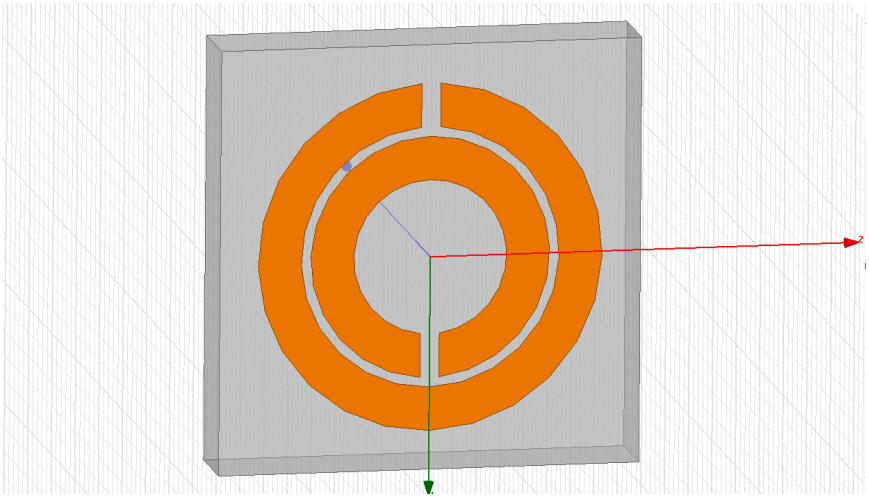

Figure 1.5: SRRs to Realize Effective Negative Permeability [11, 5]

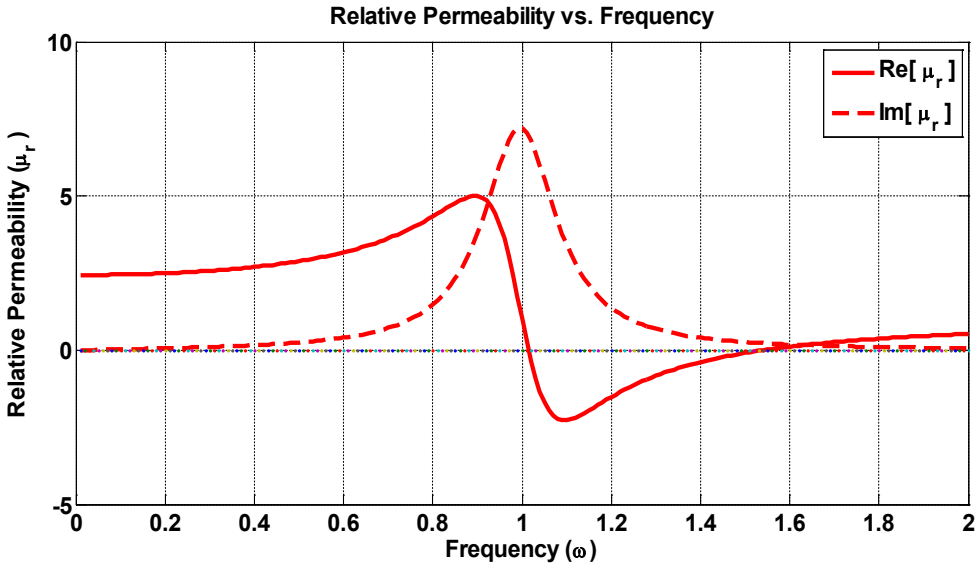

Figure 1.6: Effective Negative Permeability Response Realized by Resonant SRR [11, 5]

1.10 S-parameter Retrieval Method: Transmission and Reflection

A metamaterial structure or an effective medium can be characterized by its effective constitutive parameters. However, the constitutive parameters of the material cannot be directly calculated or measured, so a retrieval technique must be applied. Parameter retrieval of effective media tends to be one of the most difficult aspects of metamaterial research. Several popular methods include the S-parameter retrieval method, homogenization by field averaging [10], T-matrix parameter retrieval, and refractive index retrieval through phase response [18]. The most commonly used method, which is the method used in this paper, is S-parameter retrieval [19, 20].

The basis of the S-parameter retrieval method is that a finite metamaterial slab produces a complex reflection and transmission response. For any observed metamaterial transmission and reflection response, a homogeneous slab of the same thickness will produce the same complex transmission and reflection response if assigned the correct constitutive material parameters (ε_{eff} and μ_{eff} or n_{eff} and η_{eff}). The S-parameter retrieval technique is complicated due to complex branching, which will be discussed later in this chapter. This work primarily uses Chen's

technique [19] for calculation of the constitutive parameters from the S-parameter data by implementing a proprietary MATLAB code developed by LaRouche [21].

Summary of Retrieval Equations using Chen's Technique [19, 9]:

$$S_{11} = \frac{(1-t^2)r}{1-r^2t^2};\ S_{21} = \frac{(1-r^2)t}{1-r^2t^2};\ r = \frac{\eta-\eta_0}{\eta+\eta_0};\ t = e^{jk_0nd} \tag{1.37}$$

$$\eta \pm \sqrt{\frac{(1+S_{11})^2-S_{21}^2}{(1-S_{11})^2-S_{21}^2}} \tag{1.38}$$

$$n' = \frac{1}{k_0 d}\left(\mathrm{Im}[\ln t] + 2\pi m\right) \tag{1.39}$$

$$n'' = -\frac{1}{k_0 d}\mathrm{Re}[\ln t] \tag{1.40}$$

$$\mu = n\eta \quad \varepsilon = n/\eta \tag{1.41}$$

$$|n'\eta''| \leq n''\eta' \tag{1.42}$$

$$S_{11} = \frac{\eta-\eta_0}{\eta+\eta_0}\frac{1-e^{-j2kd}}{1-[(\eta-\eta_0)/(\eta+\eta_0)]^2e^{-j2kd}} \tag{1.43}$$

$$S_{21} = \frac{4\eta\eta_0}{(\eta+\eta_0)^2}\frac{e^{-jkd}}{1-[(\eta-\eta_0)/(\eta+\eta_0)]^2e^{-j2kd}} \tag{1.44}$$

To settle some of the complex branching issues, a passive material will be assumed. As long as no active circuit components are introduced in the effective media, this assumption will be correct. The passive material assumption means that the resistive part of impedance must be positive to not imply gain, and the complex part of *n*, also known as the extinction coefficient, must be positive for field decay to convey loss in the material rather than gain [19]. All of the signs and branches chosen in the S-parameter retrieval technique must be chosen to fulfill the passive material assumptions. These assumptions are summarized as follows

$$\begin{aligned} &\mathrm{Re}[\eta] \geq 0 \\ &\mathrm{Im}[n] \geq 0. \end{aligned} \tag{1.45}$$

The S-parameter retrieval technique used in this study will be summarized. The metamaterial structure is first defined in the HFSS CAD environment. Using HFSS or another full-wave electromagnetic simulation software, the structure is simulated to obtain the two-port S-parameters. Similarly, if a physical structure is being measured, the S-parameters can be obtained using antennas and a vector network analyzer. Once S-parameters have been obtained, a transfer function is applied to extract material properties or constitutive parameters. From this data, the metamaterial slab's effective refractive index, permittivity, permeability, and phase reflection can be calculated over a range of frequencies.

1.11 Negative Index of Refraction

To achieve a negative index of refraction ($n < 0$), we require that ε and μ be simultaneously negative at a given frequency [4]. As stated above $n = \sqrt{\varepsilon_r \mu_r}$ inside of a bulk medium. A simple analysis may assume that $n = \sqrt{(-1)|\varepsilon_r|(-1)|\mu_r|} = \sqrt{\varepsilon_r \mu_r}$ for a DNG medium with $\varepsilon_r, \mu_r < 0$. However, this is an incorrect analysis, which has been verified physically through experimentation [22]. For the lossless case, we will now express permittivity and permeability as $\varepsilon = |\varepsilon| e^{j\phi_E}$ and $\mu = |\mu| e^{j\phi_M}$ where ϕ_E and ϕ_M will take on a value of either 0 or π. The equation for the index of refraction now becomes as follows

$$n = \sqrt{|\varepsilon_r||\mu_r|} e^{j/2(\phi_E + \phi_M)} \tag{1.46}$$

Using this equation, ϕ_E and ϕ_M must both be equal to π result in $n < 0$. From this analysis, it is shown that when $\varepsilon_r, \mu_r < 0$, the proper expression for the refractive index is $n = -\sqrt{|\varepsilon_r||\mu_r|}$, since $e^{j\pi} = -1$ [6, 23]. From this analysis, we can also see that when μ and ε have opposite signs, *n* becomes imaginary and the wave inside the material will be evanescent [24].

The work of Veselago remained dormant for about 30 years, and it was not until the late 1990s when Pendry and his colleagues suggested that DNG materials could be created artificially by using periodic structures [7, 5]. Not long after Pendry, Smith and his collaborators [7, 1, 25, 2, 26, 22] built materials that exhibited DNG characteristics.

In academic literature, metamaterials that exhibit a negative index of refraction are referred to by many different names including double negative materials (DNG), NRI (negative refractive index), NIM (negative index material), BW (backward) media, and left-handed (LHM) media, to name a few [7]. In this paper, these materials will be referred to as DNG metamaterials with a few possible exceptions. While there are many different names for a material displaying a negative index of refraction, all of these names imply that the real part of ε and μ are less than zero over a given frequency range. A large portion of the research performed on metamaterials in recent years has focused on exploring, realizing, and verifying DNG materials. The reason that DNG metamaterials have attracted considerable interest is that, unlike DPS, ENG, and MNG metamaterials, DNG metamaterials exhibit exotic material properties not found in nature [4].

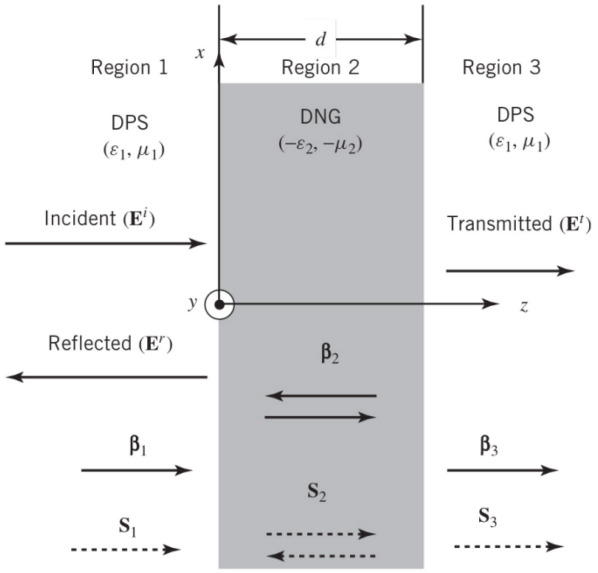

Figure 1.7: Reflection and transmission through a DNG slab [7]
(used by permission from Wiley, publ.)

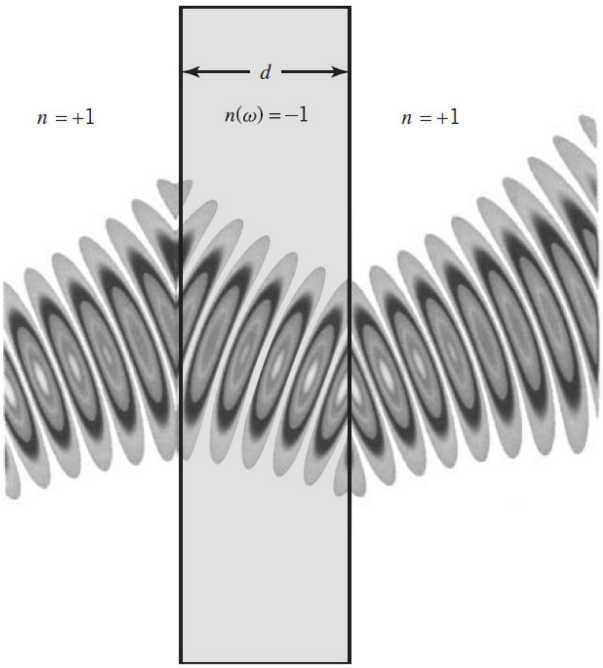

Figure 1.8: Wave propagation through a DNG slab with n(ω)=-1 [7]
(used by permission from Optical Express, publ.)

Exotic properties of a DNG metamaterial include negative refraction angle, backwards wave propagation, phase advancement, reversed Doppler shift, and reversed Cerenkov radiation [1].

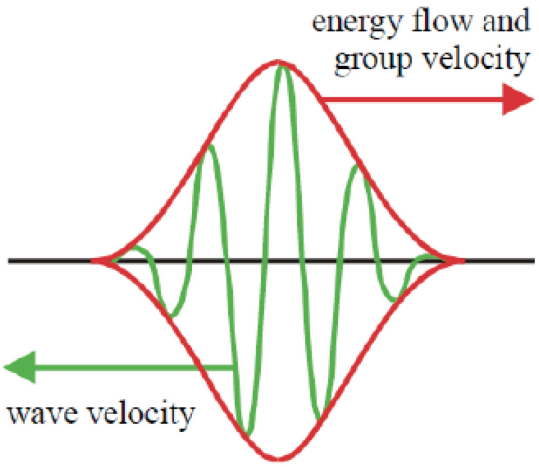

Figure 1.9: Depiction of wave velocity opposite to energy flow in a DNG media[27] (used by permission from Taylor & Francis, publ.)

Mathematically, the refractive index inside of a DNG medium can be expressed as [7]

$$n^2 = \varepsilon_r \mu_r \Longrightarrow n = \pm\sqrt{\varepsilon_r \mu_r} = \pm\sqrt{(-|\varepsilon_r|)(-|\mu_r|)} = \pm\left(j\sqrt{|\varepsilon_r|}\right)\left(j\sqrt{|\mu_r|}\right) \quad (1.47)$$

$$n^2 = \pm j^2\sqrt{|\varepsilon_r \mu_r|} = \mp\sqrt{|\varepsilon_r \mu_r|}. \quad (1.48)$$

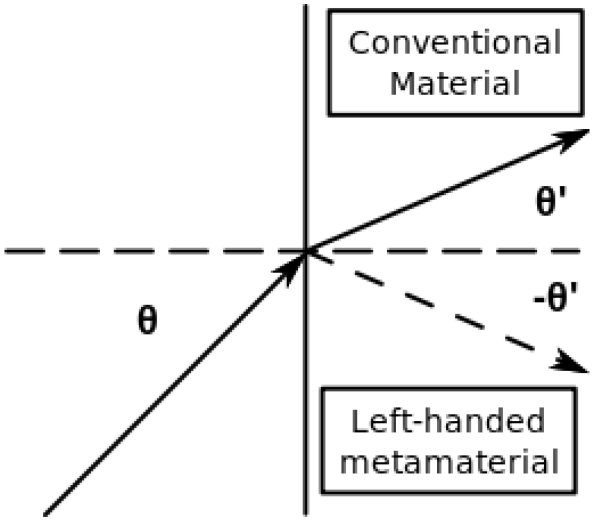

Figure 1.10: Depiction of Negative Refraction at a Dielectric Interface [28] (used by permission from Wilson via Wikimedia Commons)

Snell's Law at the interface of a DPS media and a DNG media can be described as [9]:

$$\theta_{refl} = \theta_{inc} \quad (1.49)$$

$$\theta_{trans} = \operatorname{sgn}(n_2)\sin^{-1}\left(\frac{n_1}{|n_2|}\sin\theta_{inc}\right) \quad (1.50)$$

1.12 Artificial Magnetic Conductors and Applications to Antennas

Metamaterials can be engineered to act as artificial magnetic conductors (AMCs), which are similar to electromagnetic bandgap surfaces (EBG) in that they produce near zero phase reflection. This property is extremely useful in realizing low profile antennas because an AMC antenna backplane can be placed much closer than a traditional metallic backplane while still producing an in-phase reflection resulting in constructive interference with the transmitting antenna.[29, 30, 31].

Using metamaterial realizations, such as the AMC for antenna applications, it has been reported that the integration of materials with radiating elements can increase the radiated power, enhance the gain, and tune the frequency of operation [30, 7].

Chapter 2: Characterization of Periodic CLL Structures

2.1 Introduction

The first step of this research analyzed the proposed capacitively-loaded loop (CLL) metamaterials in a periodic structure. A single metamaterial unit cell is simulated using periodic boundary conditions, effectively creating an infinite periodic array of metamaterial in the vertical and horizontal directions. The effective material is analyzed by extracting the effective permittivity and permeability of the metamaterial slab from its scattering data. The reflection and transmission properties of the CLL-based metamaterial structure were obtained directly from numerical simulations using ANSYS's High-Frequency Structure Simulator (HFSS), a full-wave finite element solver.

The CLL used in simulation was engineered to resonate at a frequency near 15 GHz; however, the dimensions of the unit cell were scaled to resonate at any desired frequency. The dimensions of the cell are shown in Figure 2.1. The metallic loop and wire are both made of copper, and the dielectric slab in-between the loop and the wire is FR4 epoxy ($\varepsilon = 4.4$, $\mu = 1$, dielectric loss tangent $\delta = 0.02$) with a thickness of 1.3mm.

In HFSS, the metamaterial slab was placed in between two vertically oriented waveports with a free space buffer of several wavelengths between each waveport and the slab. To create an infinite array, perfect electric (PEC) boundary conditions were placed on the top and bottom of the cell and perfect magnetic (PMC) boundary conditions on the sides, as seen in Figure 2.2.

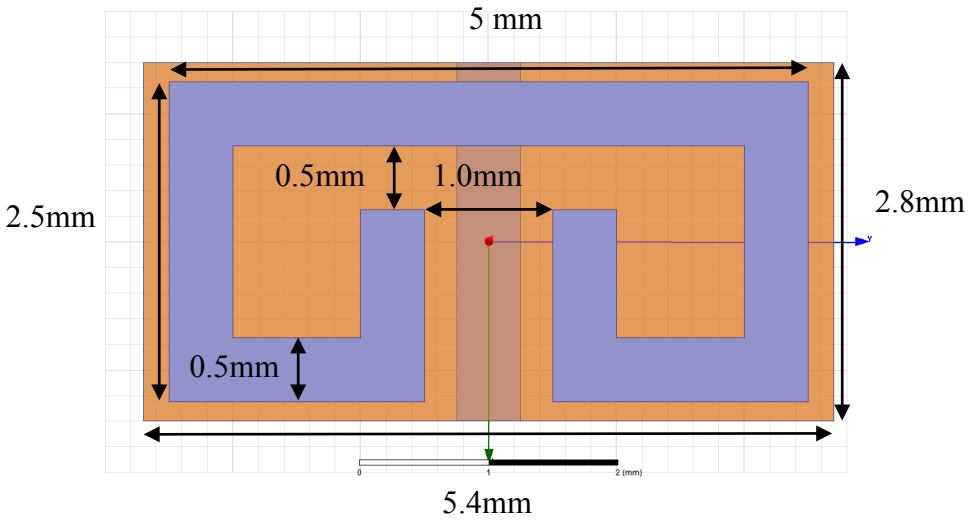

Figure 2.1: Dimensions of CLL Inclusion Used in This Study

The scattering parameters of the CLL were obtained using HFSS in multiple configurations with propagation perpendicular and parallel to the CLL and with and without continuous metal wire paired with the loop. Mutiple orientations and variations of this scattering element will be discussed in this chapter.

2.2 Verification of Constitutive Parameter Extraction Method

To verify our HFSS simulation set-up and our implementation of the S-parameter retrieval technique, a well known published SRR and continuous wire combination was replicated and simulated [20]. The simulated S-parameters, shown in Figure 2.3 and Figure 2.4, and extracted constitutive parameters, shown in Figure 2.5, were compared to published data to verify and increase confidence in the retrieval technique. The results of this work are compared to published results, shown in Figure 2.6. The agreement of both S-parameters and constitutive parameters with published data is very good. Additional published metamaterial structures were also successfully simulated for purposes of verification, but are not included in this thesis.

Figure 2.2 depicts the different boundaries and the simulation set-up used to obtain S-parameters in HFSS. A second waveport (not pictured) is adjacent to the propagating waveport shown in the upper right of Figure 2.2. The metamaterial inclusion is placed in the center of the unit-cell. Perfect electric conducting (PEC) boundaries on the top and bottom of the cell fixed the orientation of the electric field to be vertical, and PEC walls create an infinite array vertically.

The perfect magnetic conducting boundaries (PMC) on the sides extend the infinite array effect, effectively repeating the cell infinitely in both horizontal directions. The depth of the cell, in the dimension in the direction of propagation ($-\hat{z}$) shown as the red axis in Figure 2.2, is finite.

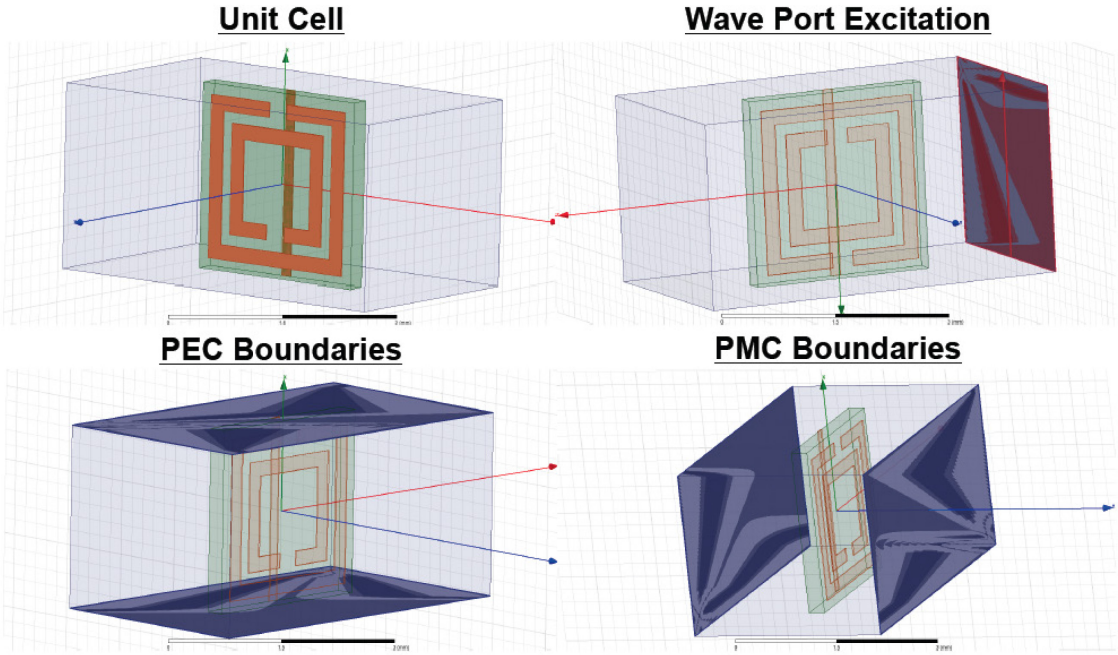

Figure 2.2: Depiction of HFSS Simulation Set-up for Typical SRR w/ Continuous Wire

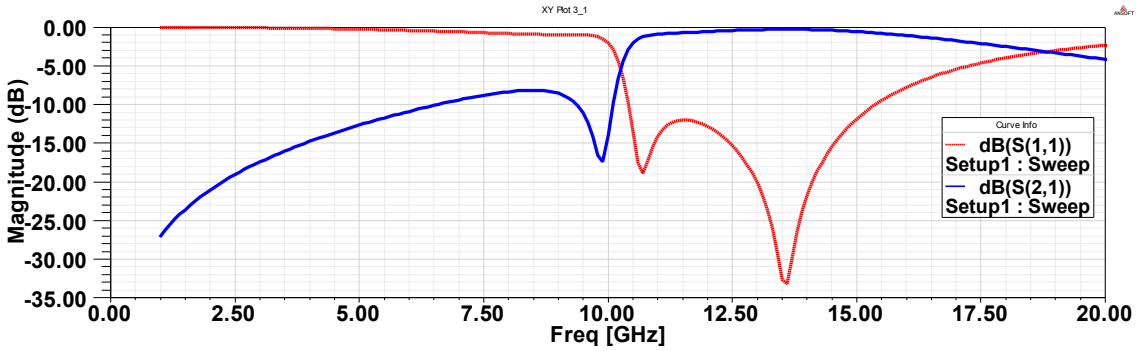

Figure 2.3: S-parameter Magnitude Response for SRR w/ Continuous Wire

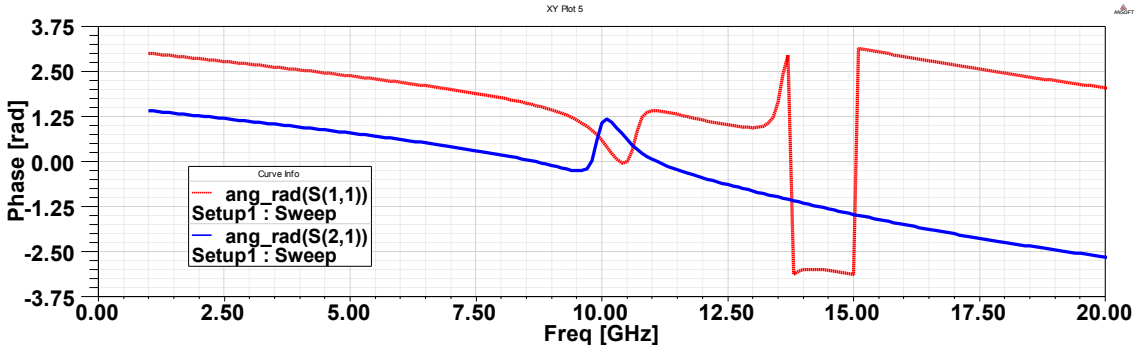

Figure 2.4: S-parameter Phase Response for SRR w/ Continuous Wire

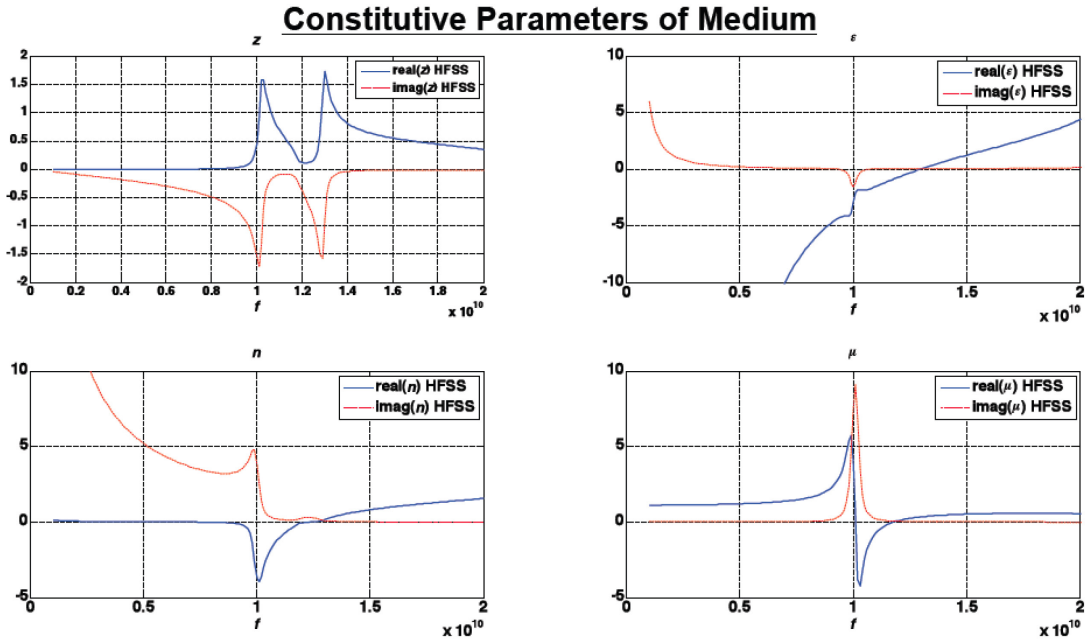

Figure 2.5: Constitutive Parameter Response for SRR w/ Continuous Wire

Paper: Electromagnetic parameter retrieval from inhomogeneous metamaterials

Authors: Smith, Vier, Koschny, and Soukoulis

Journal: Physical Review E 71, 2005

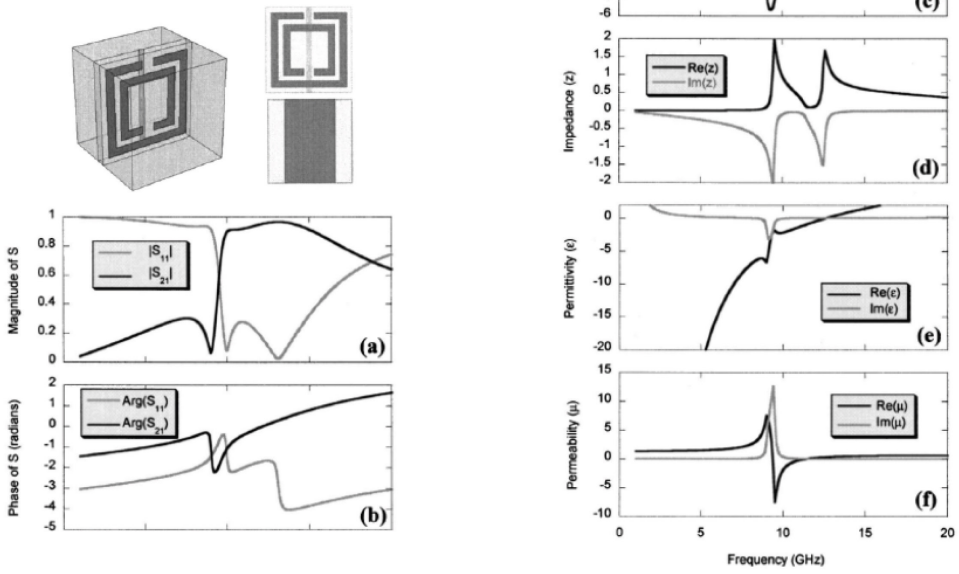

Figure 2.6: Published Results for (a) S-parameter Magnitude; (b) S-parameter Phase; (c) Refractive Index; (d) Impedance; (e) Permittivity; and (f) Permeability [20]

2.3 Simulation of Periodic CLL Structures

The unit-cell with PEC and PMC boundaries will be utilized in HFSS to obtain simulated S-parameters for various structures shown in this chapter.

2.3.1 Infinite Dielectric Block

For purposes of comparison, the first simulation was of a finite depth FR4 dielectric slab with a material thickness of 1.3mm. With PEC vertical boundaries and PMC horizontal boundaries, the simulated slab is effectively infinite in the horizontal and vertical dimensions. As with all of the PEC/PMC unit cells, the TEM wave is able to propagate, unlike standard metallic waveguide. In addition, the simulation of a homogeneous FR4 dielectric slab, shown in Figure 2.7, will allow us to observe the material loss, shown in
Figure 2.8.

In the HFSS simulation of a FR4 dielectric slab shown in

Figure 2.7 with ϵ=4.4, μ=1, and a thickness of d=1.3mm is simulated between two wave ports using PEC vertical boundaries and PMC horizontal boundaries. This test is done to verify the constitutive parameter extraction method using the complex S-parameters, shown in

Figure 2.8 and Figure 2.9. As expected, the intrinsic material losses of the dielectric increases with frequency. At very low frequencies, nearly full transmission is shown with S_{21} close to 0dB. However, S_{21} drops with frequency until transmission of S_{21} is ~-2dB at 30GHz. The extraction technique is successfully validated by calculating the permeability to b ϵ_{sim} = 4.2, μ_{sim} = 1, and n_{sim} = 2.1, shown in Figure 2.10.

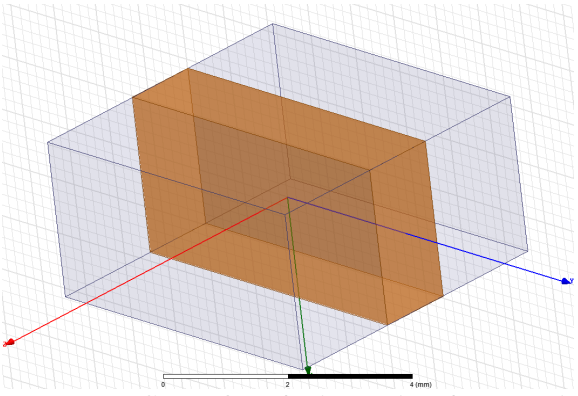

Figure 2.7: Homogeneous Slab of FR4 Dielectric w/o Metallic Loop or Wire (Propagation in the –z; PEC in ±x; PMC in ±y)

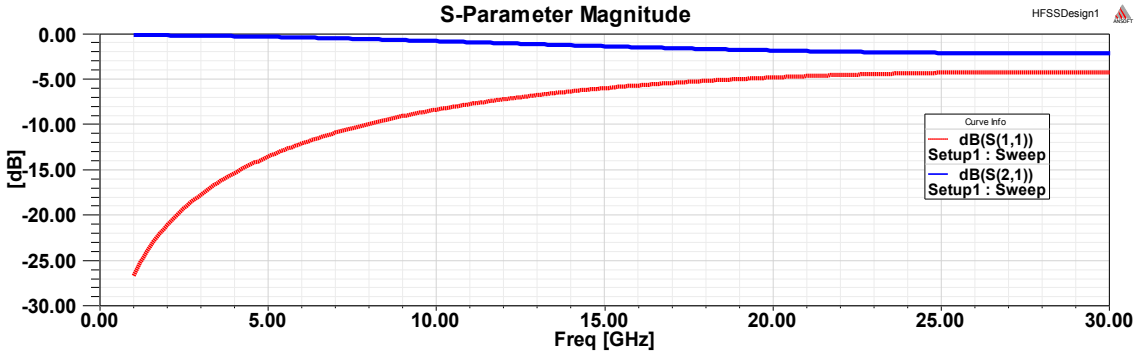

Figure 2.8: S-parameter Magnitude for Homogeneous Slab of FR4 Dielectric w/o Metallic Loop or Wire

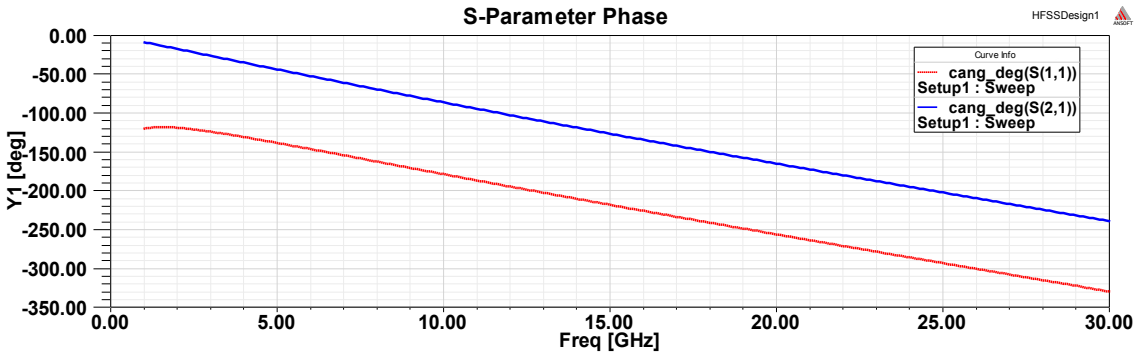

Figure 2.9: S-parameter Phase for Homogeneous Slab of FR4 Dielectric w/o Metallic Loop or Wire

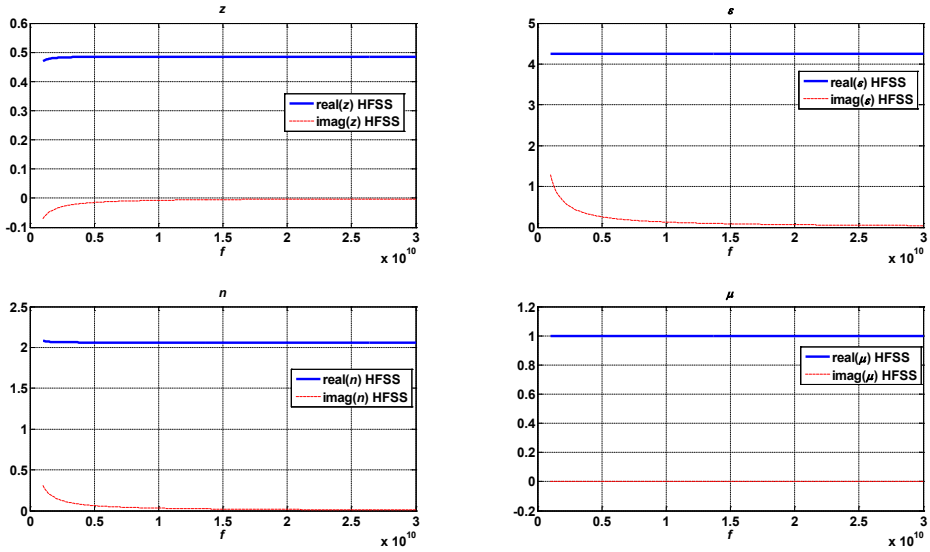

Figure 2.10: Constitutive Parameters for Homogeneous Slab of FR4 Dielectric w/o Metallic Loop or Wire

2.3.2 Periodic CLL w/o Wire (Parallel to Propagation Orientation)

Before simulating a combination of the CLL and the wire, we seek to characterize the magnetic response of the CLL under test. PEC boundaries are in the $\pm\hat{x}$ direction (green) and PMC boundaries are in the $\pm\hat{y}$ direction (blue). Propagation is in the $-\hat{z}$ direction (red) in Figure 2.11. The S-parameters of this CLL structure are shown in Figure 2.12 and Figure 2.13.

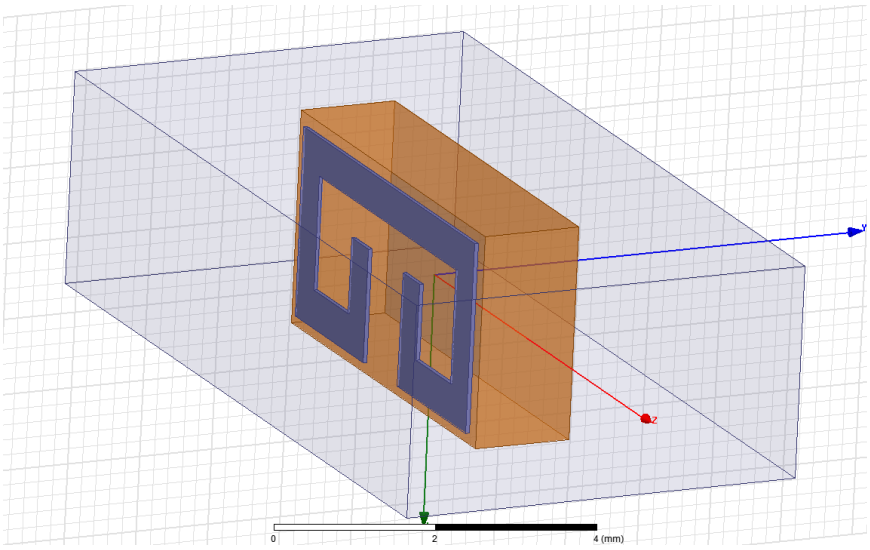

Figure 2.11: CLL w/o Wire (Parallel Propagation Orientation)

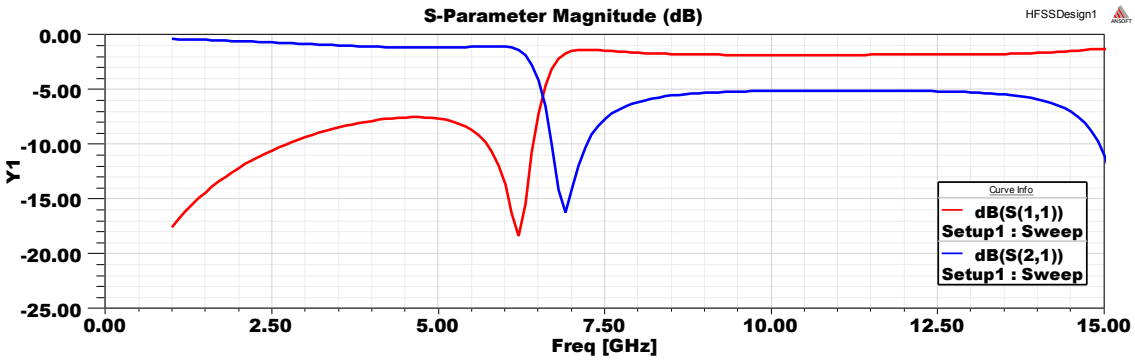

Figure 2.12: S-parameter Magnitude for CLL w/o Wire (Parallel Propagation Orientation)

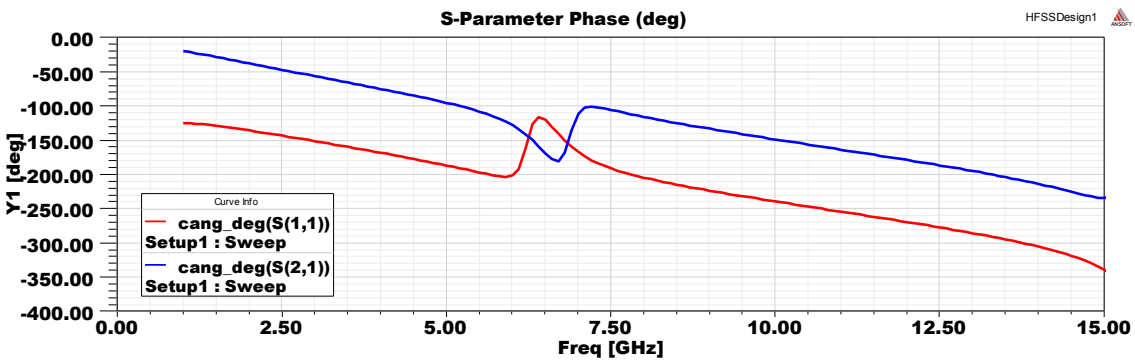

Figure 2.13: S-parameter Phase for CLL w/o Wire (Parallel Propagation Orientation)

The constitutive parameters for the infinite periodic array of the CLLs and FR4 dielectric without wire, shown in Figure 2.14, are used to characterize this electromagnetic structure. The permeability response, μ, successfully shows the typical Lorentz response with Re[μ]<0 for a given frequency range. The epsilon response, ε, shows a weak Lorentz-like response that does not exhibit Re[ε]<0 within the same frequency band. The calculated index of refraction, *n*, also shows a classic Lorentz response, however, Re[*n*] does not drop below zero as expected. While not dropping below zero, the real-part of the refractive index is Re[*n*]<1 in the resonant frequency band of interest. This makes the CLL potentially useful for transformation optics and cloaking applications, since phase velocity can become faster than the speed of light in this Re[*n*]<1 frequency band.

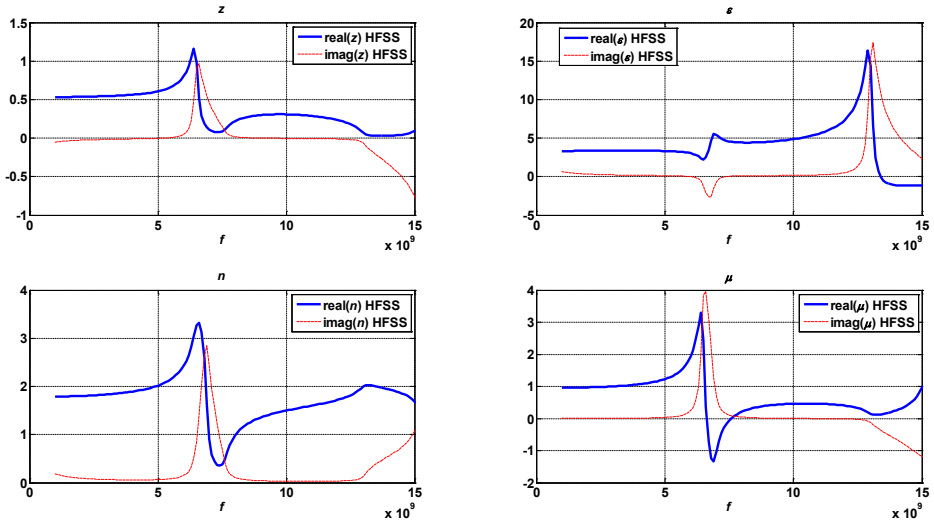

Figure 2.14: Constitutive Parameters for CLL w/o Wire (Parallel Propagation Orientation)

2.3.3 Three Layers of Periodic CLL w/o Wire (Parallel to Propagation Orientation)

A negative magnetic response was observed for a single layer of CLLs over a given frequency band. However, for practical applications, these cells may need to be periodically arrayed in the direction of propagation. For this reason, it is important to show that a negative magnetic response for the CLL can be realized by a metamaterial with multiple layers of CLLs. In Figure 2.15, a structure consisting of three layers of periodic CLLs without wires in parallel to propagation orientation is shown.

The S-parameters of this structure are shown in Figure 2.16 and Figure 2.17. It is observed that there is a stronger depth in the S_{21} resonance for three layers of CLLs when compared to a single layer. The negative μ response, shown in Figure 2.18, remains in approximately the same frequency band. In addition, the refractive index increases from $n<2$ to $n>3$ at the resonant frequency for the three layer case. These trends may be important to keep in mind when we analyze the random metamaterial structures in the next chapter.

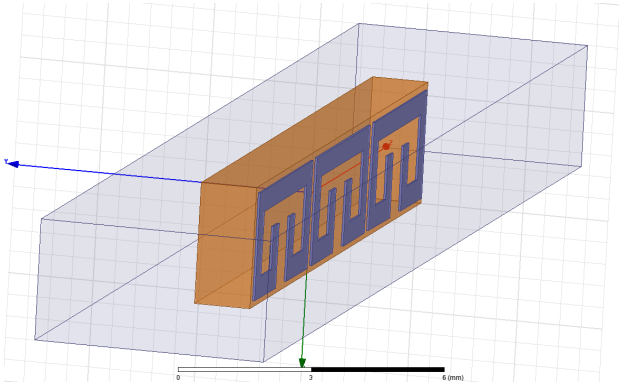

Figure 2.15: Three Layers of Periodic CLLs w/o Wire (Parallel to Propagation Orientation)

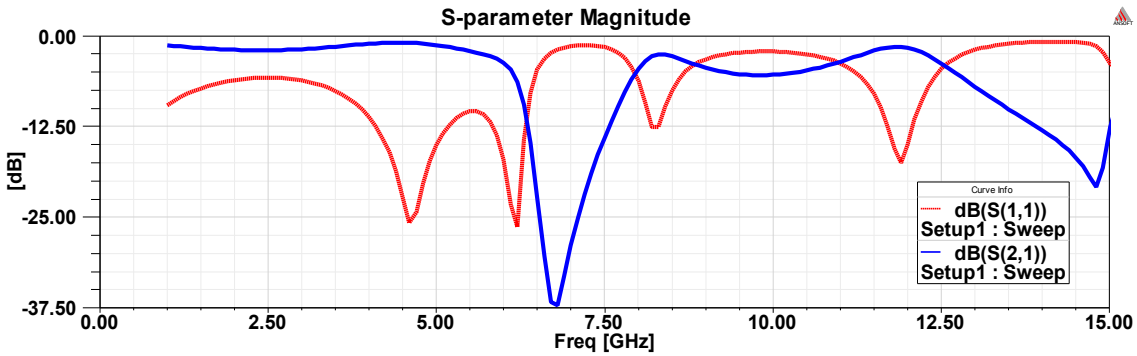

Figure 2.16: S-parameter Magnitude of Three Layers of Periodic CLL w/o Wire (Parallel to Propagation Orientation)

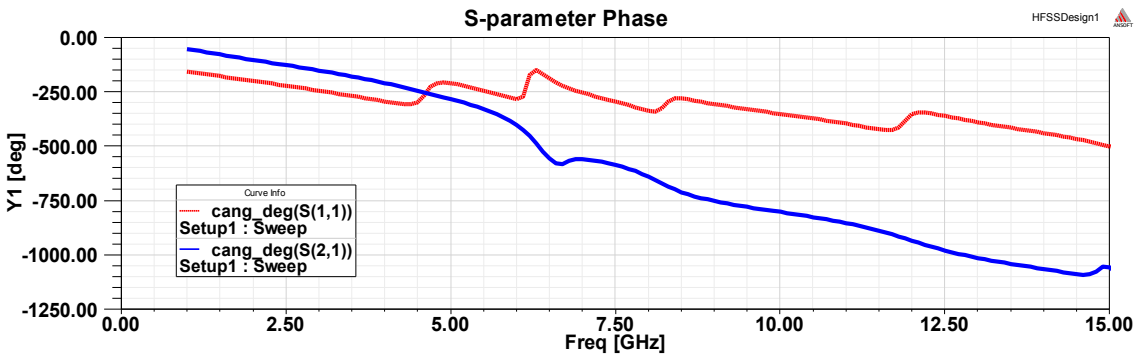

Figure 2.17: S-parameter Phase of Three Layers of Periodic CLL w/o Wire (Parallel to Propagation Orientation)

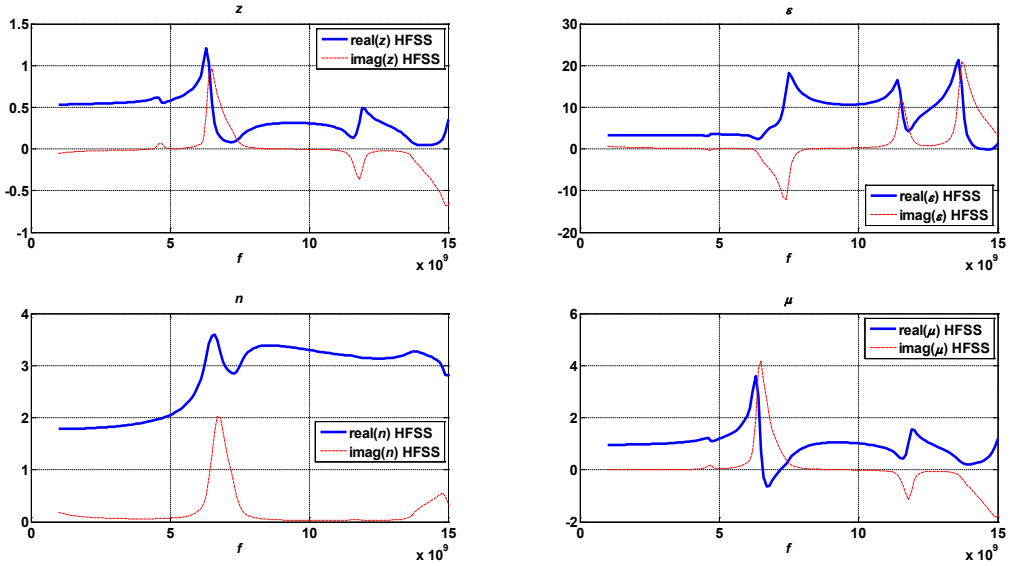

Figure 2.18: Constitutive Parameters for Three Layers of Periodic CLL w/o Wire (Parallel to Propagation Orientation)

2.3.4 Periodic CLL w/o Wire (Perpendicular to Propagation Orientation)

The CLL in perpendicular orientation without a wire is depicted in Figure 2.19 and Figure 2.20. The scattering parameters of this simulated structure show a large dip in transmission at resonance where S_{21} is -29.5dB at 13.5GHz, shown in Figure 2.21. In addition, there is a local peak in transmission directly after the resonance where S_{21} is -1.0dB at 17.4GHz. It is also important to note that there is near full transmission as the frequency approaches zero. In addition, a phase advance, a characteristic of negative refraction, of approximately 182^{o} degrees is observed from 13.0GHz to 14.0GHz, as shown in Figure 2.22. The scattering parameters of the CLL are similar to that of the standard SRR that it was modeled after.

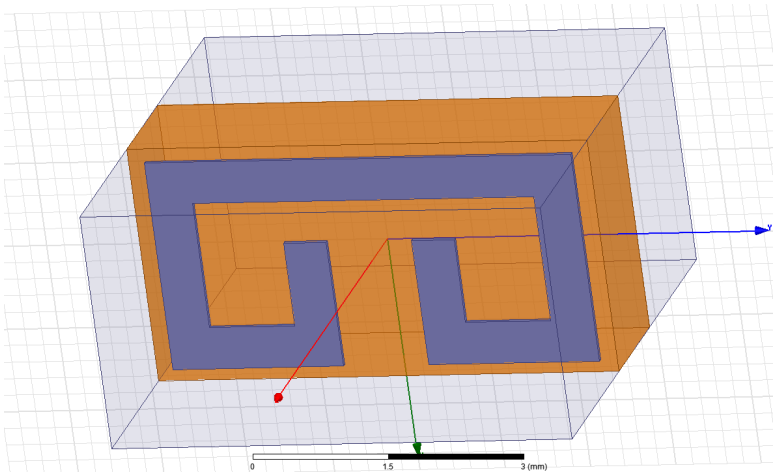

Figure 2.19: Periodic CLL w/o Wire (Perpendicular to Propagation Orientation)

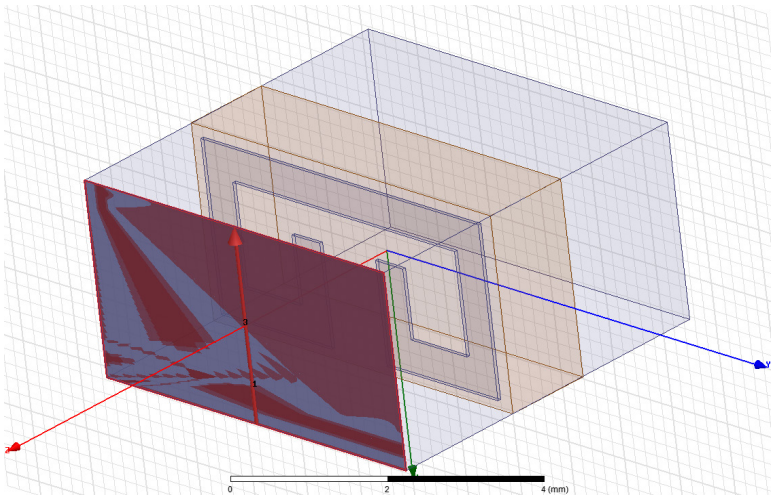

Figure 2.20: Depiction of Transmitting Waveport in HFSS for Periodic CLL w/o Wire (Perpendicular to Propagation Orientation)

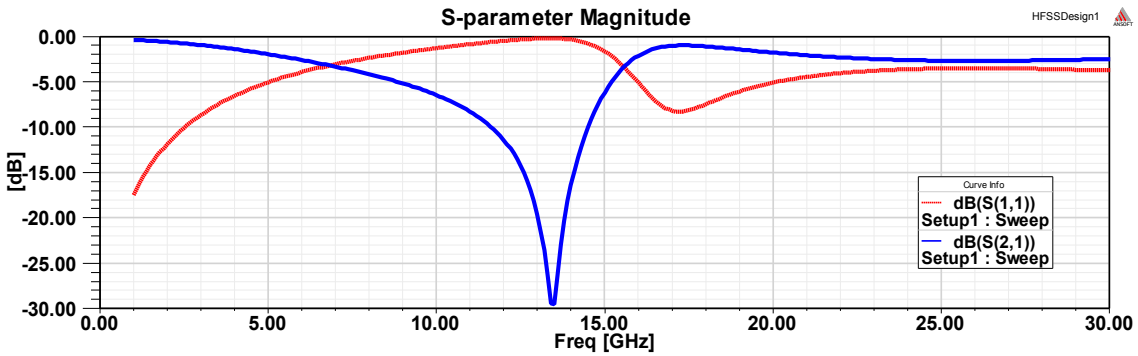

Figure 2.21: S-parameter Magnitude for Periodic CLL w/o Wire (Perpendicular to Propagation Orientation)

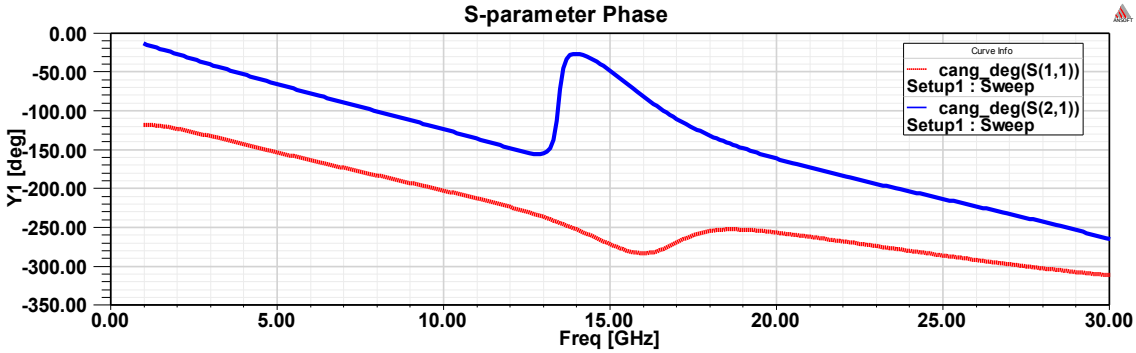

Figure 2.22: S-parameter Phase for Periodic CLL w/o Wire (Perpendicular to Propagation Orientation)

The response of the CLL without wire in the perpendicular orientation is interesting. Given that the magnetic flux curls around the X-Y (green-blue) axis in Figure 2.19, a limited magnetic response is expected from this cell because the magnetic field is not able to couple as well with the loop. The μ calculation for this CLL orientation results in a near zero μ at resonance. This CLL could be useful for specific engineering applications, such as certain microwave absorbing metasurfaces that require μ near zero. At the resonant frequency, Re[μ] is actually negative with a magnitude <0.05, shown in Figure 2.23. Given that the magnitude of Re[μ] is so small, it is possible that the below zero result is within the error of the simulation. For this reason, further analysis will need to be done to verify the Re[n]<0 result in the resonant region. The retrieval calculation shows a discontinuity between the +Re[n] and -Re[n], which causes skepticism [32]. The ε response of this CLL is very similar to that of a cut-wire, which follows the Lorentz oscillator model for dielectrics where the restoring force is present [33]. The calculated magnitude of Re[ε] is >50 just below resonance and is Re[ε] ~-50 just below the resonant frequency, which would be useful if either an extremely high or low Re[ε] response is desired. It should also be noted that the normalized intrinsic impedance is <0.1 in the resonant region leading to the observed high reflectivity of the metamaterial in the resonant region. For practical engineering application requiring transmission, the loss will need to be improved.

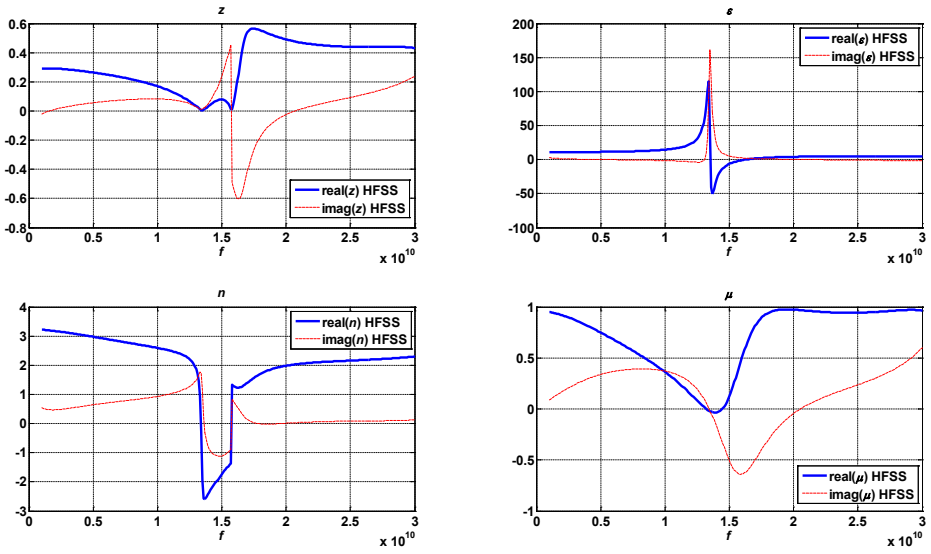

Figure 2.23: Constitutive Parameters for Periodic CLL w/o Wire (Perpendicular to Propagation Orientation)

2.3.5 Cut Wire w/o Loop

The infinite array of cut-wire case is simulated by creating a 0.1mm gap between the copper wire and the PEC boundaries on the top and bottom, shown in Figure 2.24. This simulation was done to determine the electromagnetic response that is contributed by the cut-wire.

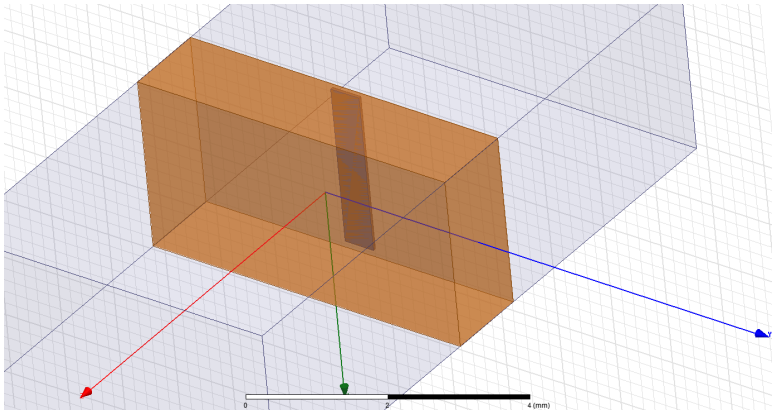

Figure 2.24: FR4 Dielectric and Continuous Wire w/o Metallic CLL Loop

The array of cut-wires allows strong transmission at low frequencies and shows a deep resonance with high reflection at 23.7GHz, shown in Figure 2.25. This behavior is consistent with the Lorentz dispersion model. Additionally, the S-parameter phase response is shown in Figure 2.26.

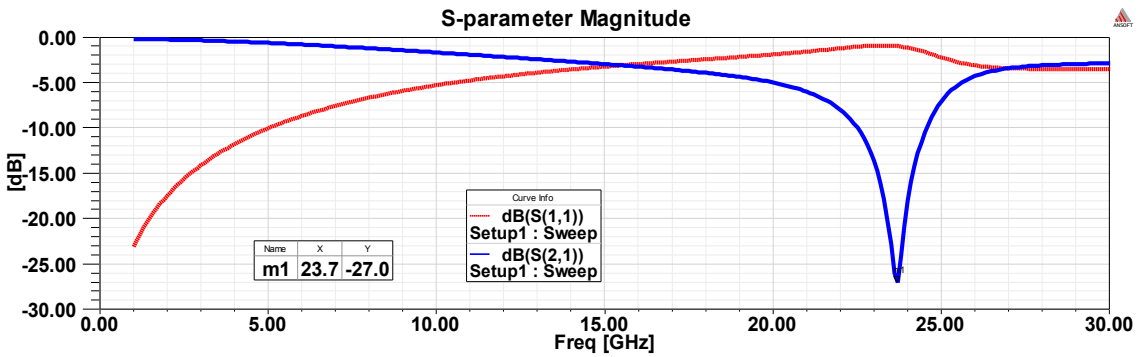

Figure 2.25: S-parameter Magnitude for FR4 Dielectric and Continuous Wire w/o Metallic CLL Loop

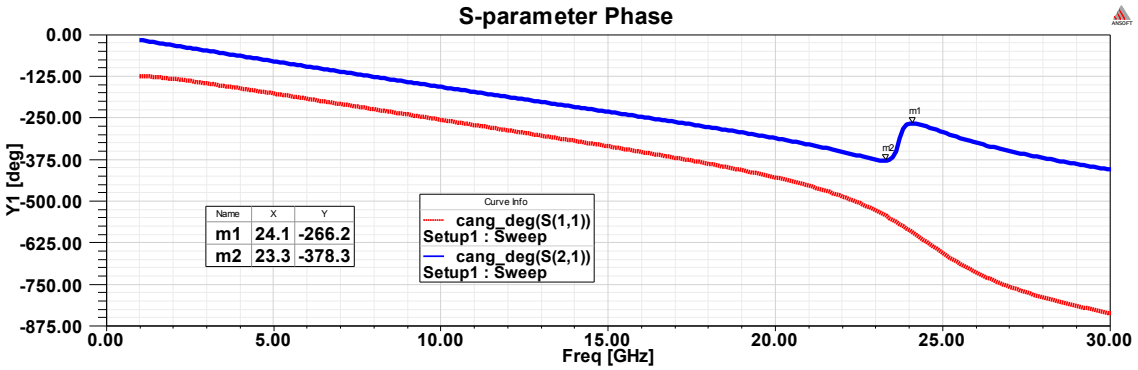

Figure 2.26: S-parameter Phase for FR4 Dielectric and Continuous Wire w/o Metallic CLL Loop

2.3.6 Continuous Wire w/o Loop

While much of the focus of this study is on the shape of the CLL, which can provide the negative magnetic response, the continuous wire and dielectric w/o CLL simulation results are shown to provide a better description of each metamaterial element's contribution. An infinite periodic array of FR4 dielectric and continuous metal wire without a metallic CLL loop is shown in Figure 2.27. The simulated S-parameters of this structure are shown in Figure 2.28 and Figure 2.29.

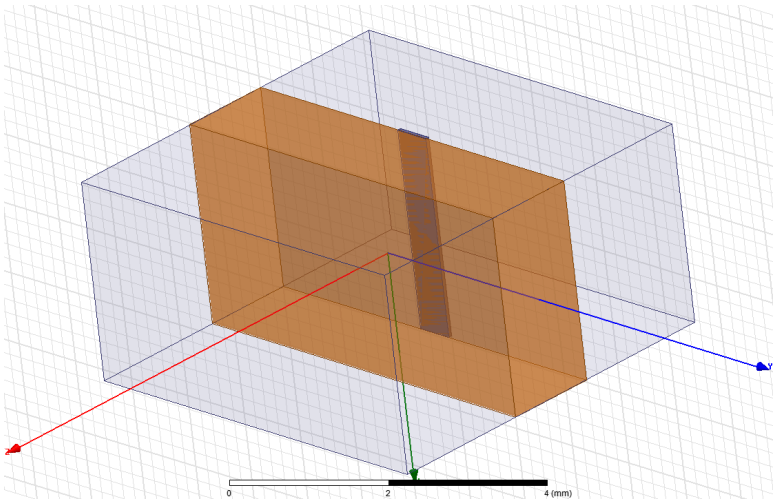

Figure 2.27: FR4 Dielectric and Continuous Wire w/o Metallic CLL Loop

Following the Drude model for metals, as predicted by Rotman [16], the infinite array of continuous metal wires provides near-zero transmission at very low frequencies, shown in Figure 2.28. The plasma frequency for this continuous wire structure is approximately f_p =16.5GHz, indicating the Re[ε] response should be below zero if $f < f_p$. In Figure 2.28, the S_{21} transmission begins to drop as frequency increases above the plasma frequency, most likely due to the material losses of the FR4 dielectric. Figure 2.29 shows the S-parameter phase response for this structure. Additionally, Figure 2.30 summarizes the difference in the dispersive Re[ε] response from the infinite arrays of continuous and cut-wire.

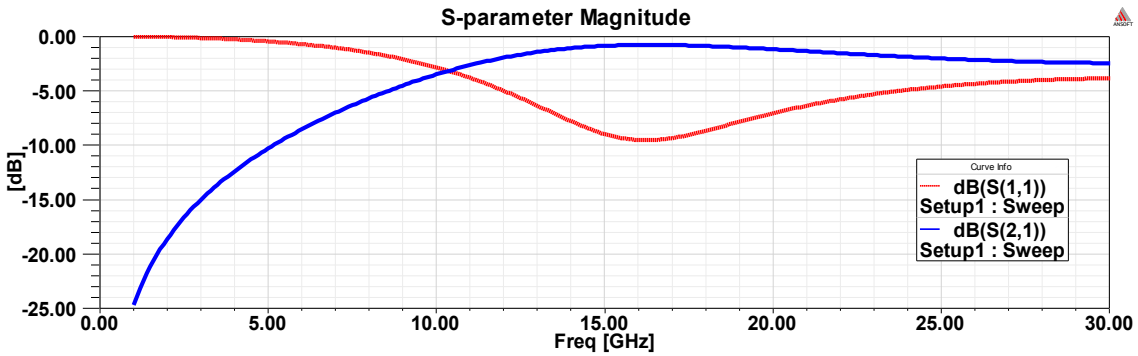

Figure 2.28: S-parameter Magnitude for FR4 Dielectric and Continuous Wire w/o Metallic CLL Loop

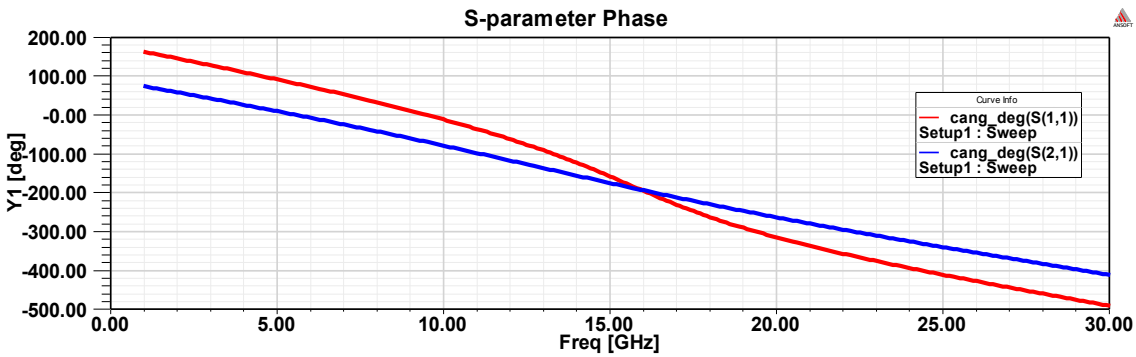

Figure 2.29: S-parameter Phase for FR4 Dielectric and Continuous Wire w/o Metallic CLL Loop

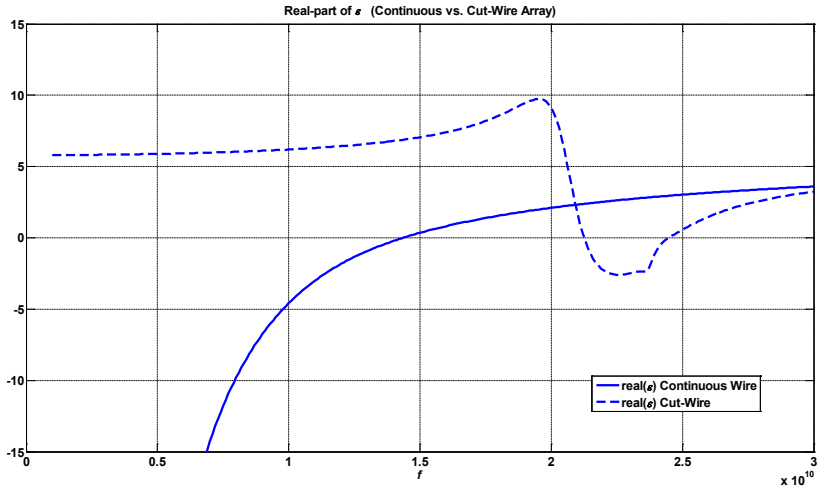

Figure 2.30: Comparison of Simulated Re[ε] vs. Frequency for Continuous and Cut-Wire Periodic Array Cases

2.3.7 Periodic CLL w/ Cut-Wire (Parallel Orientation)

It is assumed that the behavior of the CLL is similar to that of the SRR. If this assumption is true, the CLL will need to be paired with a continuous wire to produce a negative index of refraction in the resonant region. To investigate this assertion, the CLL will be paired with both continuous and cut-wire, and the effective material responses will be compared. The results of the cut-wire case are shown first below. This simulation is distinguished as cut-wire because the wire does not make contact with the PEC boundaries, as shown in Figure 2.31 and Figure 2.32.

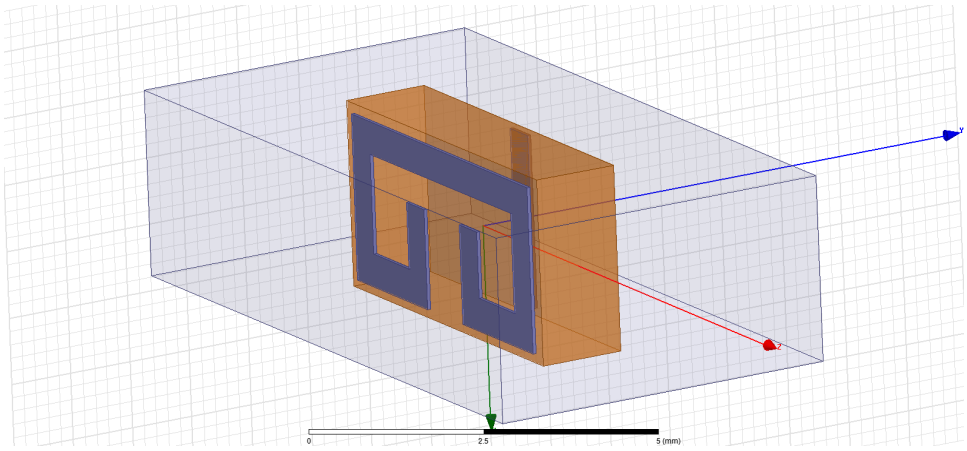

Figure 2.31: Periodic CLL w/ Cut-Wire (Parallel Orientation; 0.1mm Gap Between Wire and PEC Boundary; Propagation in –z direction (red); E-field Vertically Aligned Along x-axis (green))

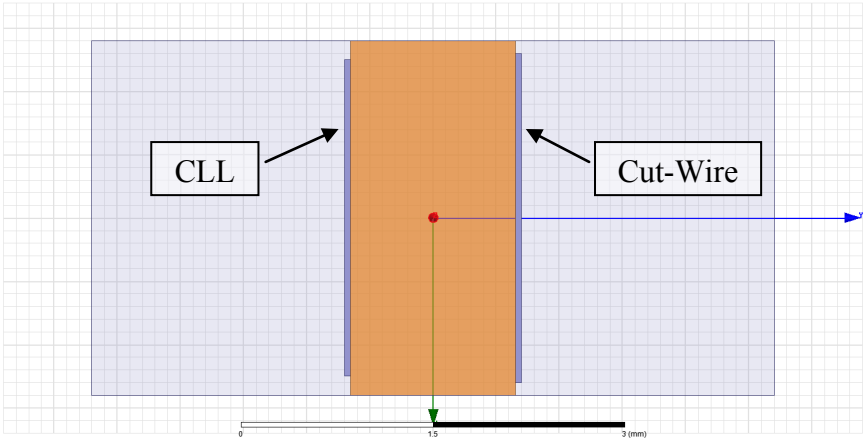

Figure 2.32: Periodic CLL w/ Cut-Wire (Parallel Orientation; 0.1mm Gap Between Wire and PEC Boundary; Propagation in –z direction (into page); E-field Vertically Aligned)

The S-parameter response for this structure is shown in Figure 2.33 and Figure 2.34. The first S_{21} resonance occurs at 6.9GHz where the S_{21} transmission falls to -16.7dB. As expected, Lorentz shaped responses are observed for both μ and ε in Figure 2.35. While the magnetic response of the structure is strong, resulting in Re[μ]<0 in the resonant range, the electric response is weaker with Re[ε]>0 in the region of interest below 15GHz. Given the ε is positive in the region that μ is negative at ~7GHz, the refractive index drops to Re[n]<1 while remaining above zero. As discussed in the previous chapter, $|n|<1$ is useful for many transformation optics and cloaking applications. This cell would work great for those applications; however, the presence of the wire would not be necessary. However, negative index of refraction is not observed for the CLL with cut-wire case.

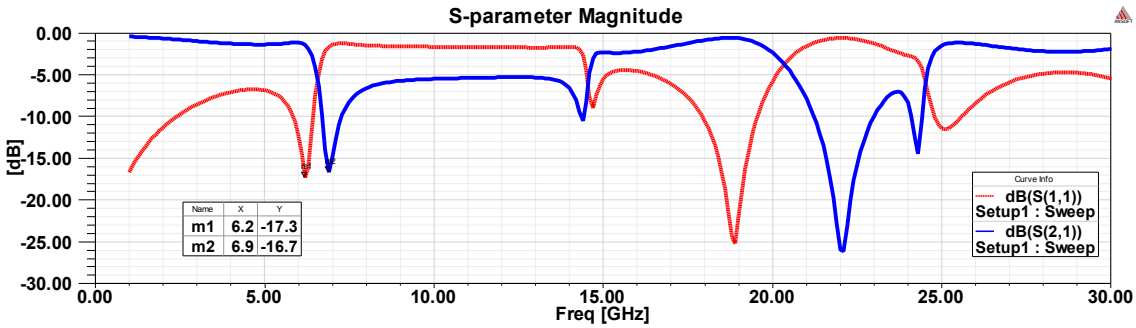

Figure 2.33: S-parameter Magnitude for Periodic CLL w/ Cut-Wire (Parallel Orientation)

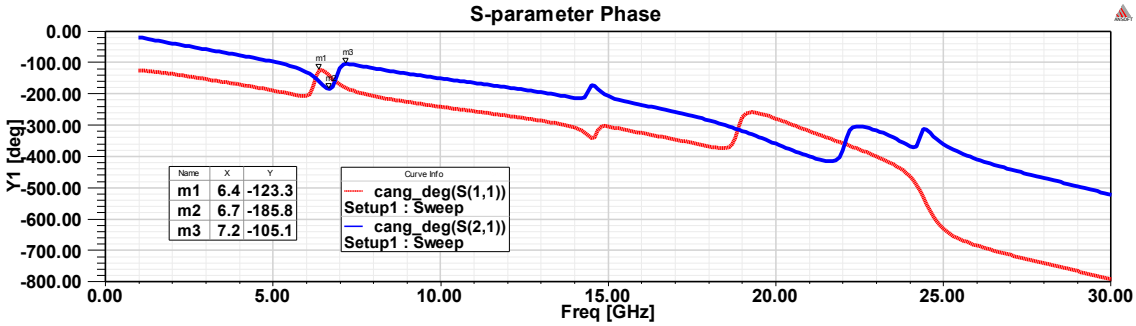

Figure 2.34: S-parameter Phase for Periodic CLL w/ Cut-Wire (Parallel Orientation)

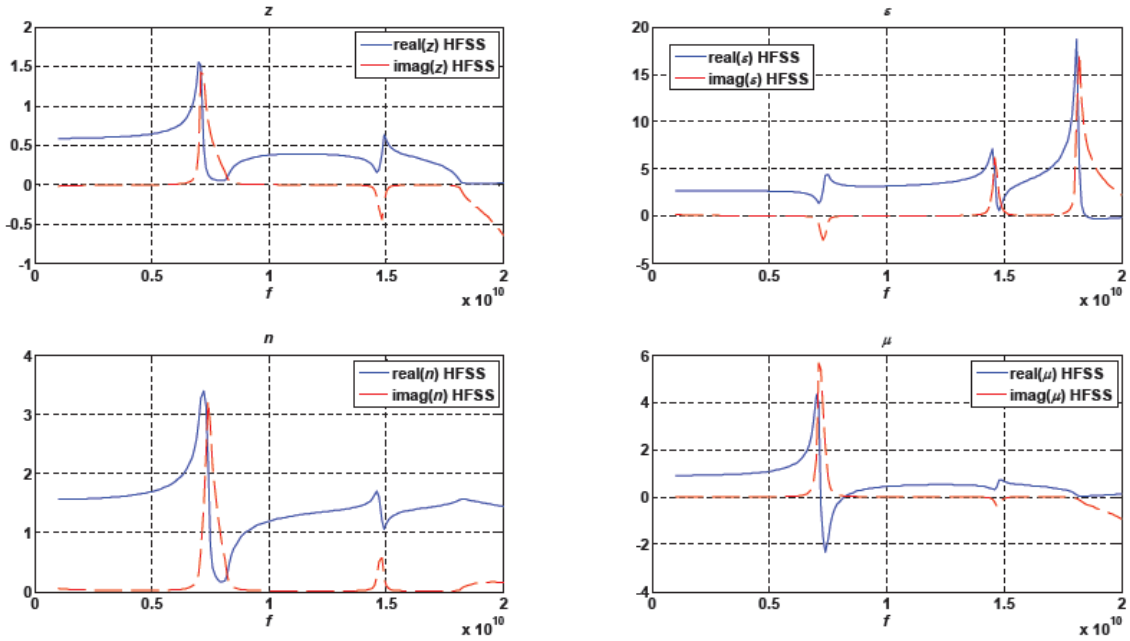

Figure 2.35: Constitutive Parameters for Periodic CLL w/ Cut-Wire (Parallel Orientation)

2.3.8 Periodic CLL w/ Continuous-Wire (Parallel Orientation)

The infinite periodic array of CLLs with continuous-wire in parallel orientation, shown in Figure 2.36, is the structure that is expected to give the best negative refraction response. As shown in Figure 2.37, the wire is made continuous because it makes contact with the top and bottom PEC boundaries. The assignments of the PEC boundary and the transmitting waveport with a vertically oriented E-field are depicted in Figure 2.38. The receive waveport on the other side of the box in Figure 2.38 is not shown. The meshing of this structure used for simulation in HFSS is shown in Figure 2.39. The current distribution along the CLL with continuous-wire structure at 6.5GHz is shown in Figure 2.40.

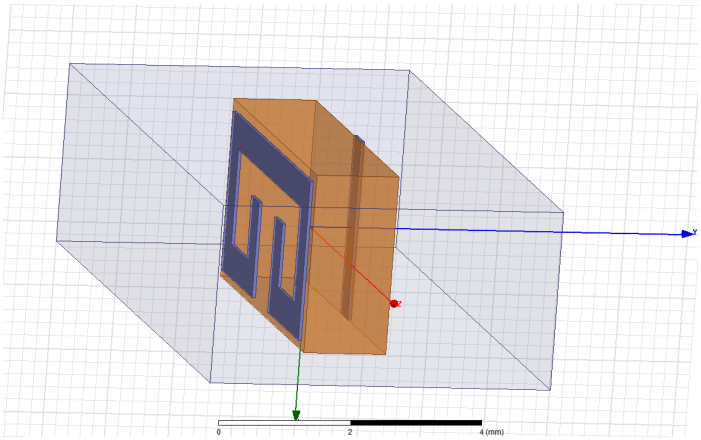

Figure 2.36: Periodic CLL w/ Continuous-Wire (Parallel Orientation) (Propagation in the –z; PEC in ±x; PMC in ±y)

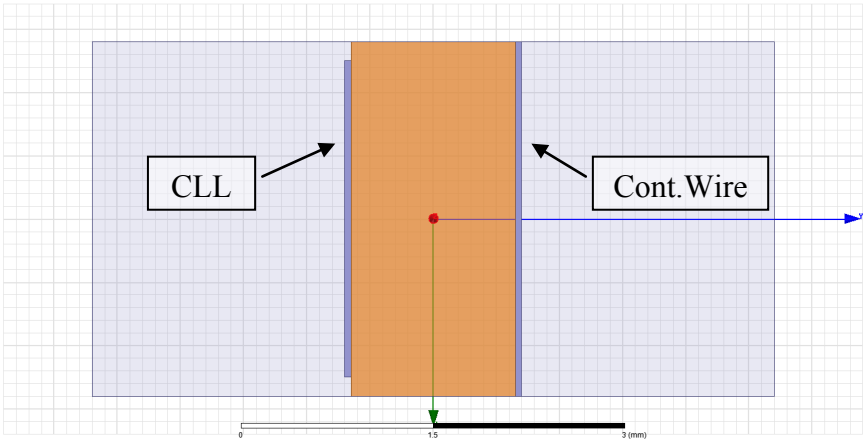

Figure 2.37: View in Propagating Direction for Periodic CLL w/ Continuous-Wire (Parallel Orientation)

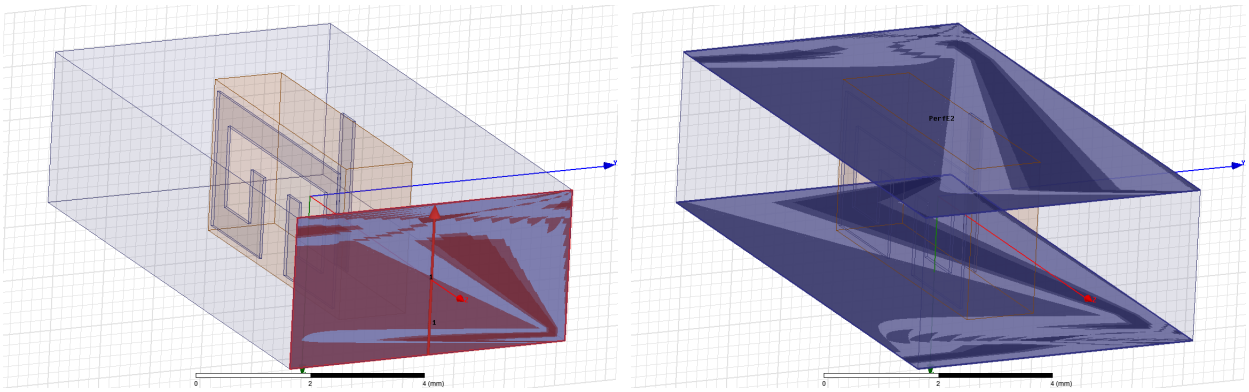

Figure 2.38: Transmitting Waveport and PEC Vertical Boundaries for Propagating Direction for Periodic CLL w/ Continuous-Wire (Parallel Orientation)

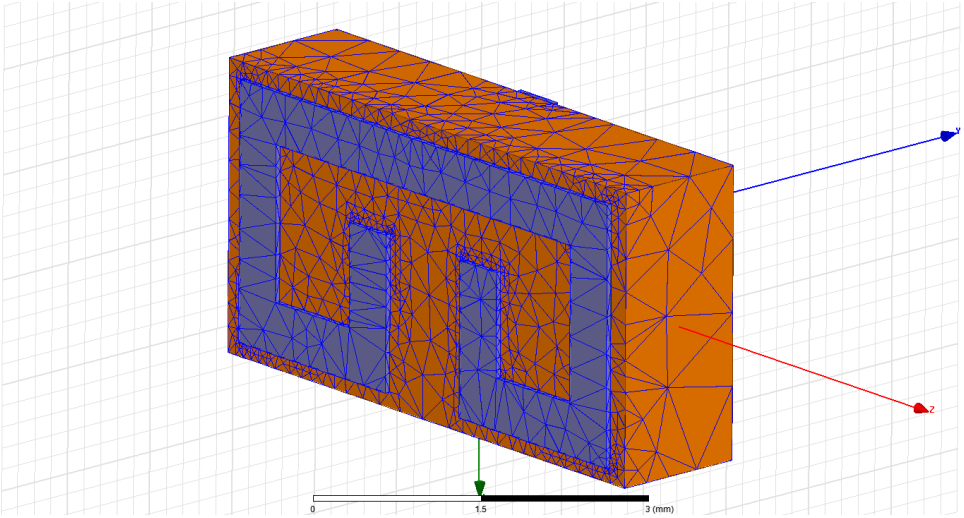

Figure 2.39: Adaptive Meshing in HFSS of Periodic CLL w/ Continuous-Wire (Parallel Orientation)

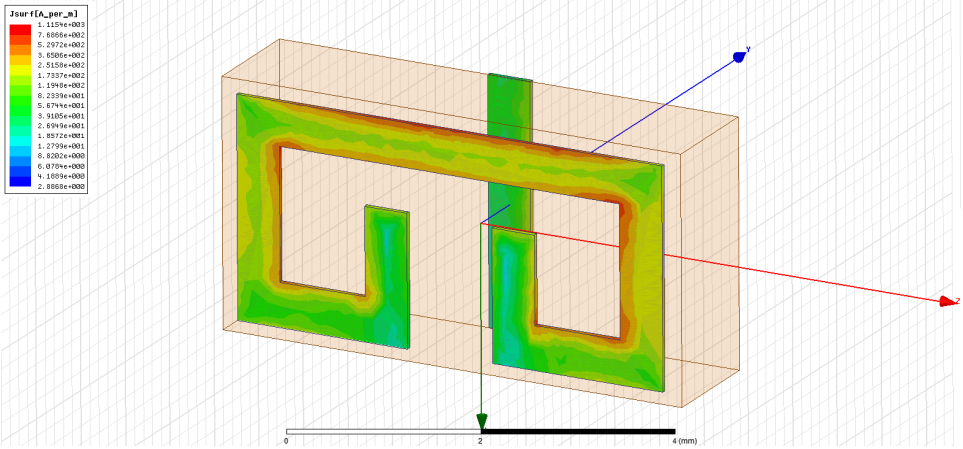

Figure 2.40: Log Distribution of Current of Periodic CLL w/ Continuous-Wire at 6.5GHz (Parallel Orientation)

The S-parameters for this structure are shown in Figure 2.41 and Figure 2.42. Following the Drude model, the transmission response below the 1st order resonance is very low. The 1st order S_{21} resonance for this structure occurs at 6.3GHz with a transmission of -14dB. In addition, there a small phase advance at this frequency.

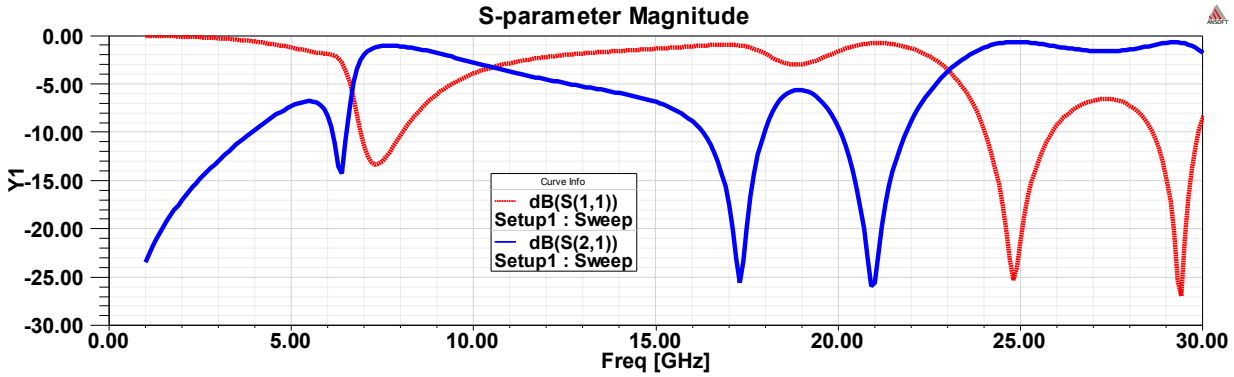

Figure 2.41: S-parameter Magnitude for Periodic CLL w/ Continuous Wire (Parallel Orientation)

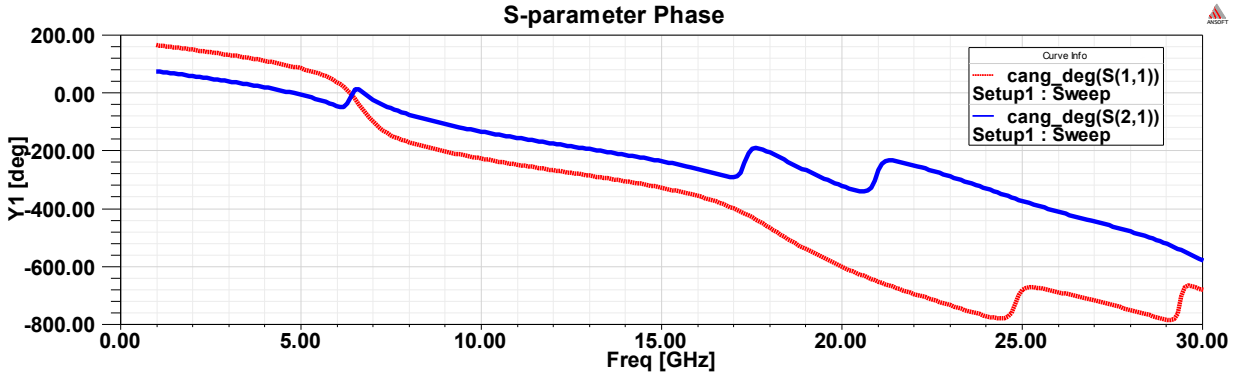

Figure 2.42: S-parameter Phase for Periodic CLL w/ Continuous Wire (Parallel Orientation)

The constitutive parameters of the structure, shown in Figure 2.43, are very interesting. The classic Lorentz response is seen in the real part of the permeability response. Over a given frequency band around the 1st order resonance at 6.3GHz, the CLL provides a $\mathrm{Re}[\mu]<0$ response as desired. In addition, the response of the continuous metal wire provides a $\mathrm{Re}[\varepsilon]<0$ over this same frequency band. As a result, the structure successfully achieves a finite band of negative refractive index at the frequency of the 1st order resonance, as shown in the bottom left corner of Figure 2.43. As a result, an incoming plane wave that interacts with the CLL and continuous wire periodic structure will exhibit a negative index of refraction, and the resulting exotic material properties, within the frequency band around 6.3GHz.

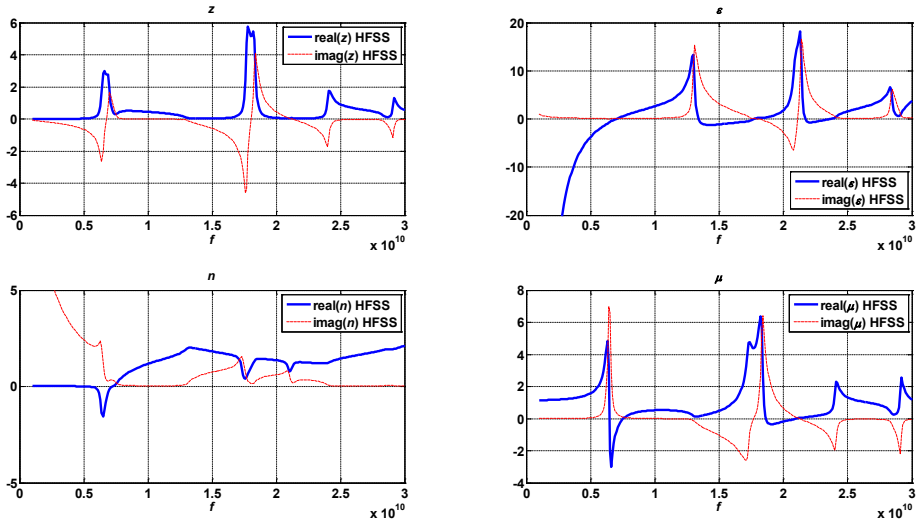

Figure 2.43: Constitutive Parameters for Periodic CLL w/ Continuous Wire (Parallel Orientation)

To gain further insight into the magnetic response from this CLL and continuous wire structure, the magnetic flux around the structure as the result of an incoming plane wave near and outside of resonance are plotted using HFSS and are shown in Figure 2.44. Below resonance at 2GHz, minimal coupling occurs between the CLL loop and the magnetic field. Much closer to resonance at 6.5GHz, the magnetic field couples very strongly around the loops on the two ends of the CLL.

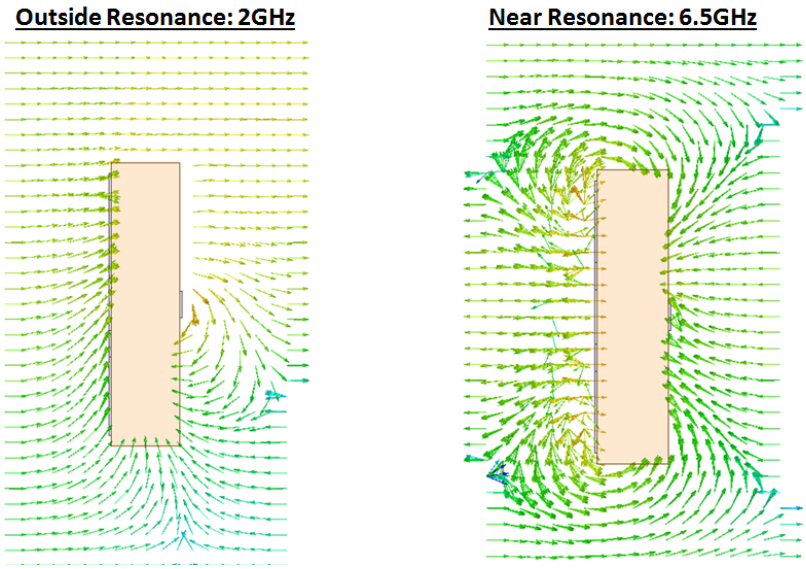

Figure 2.44: Depiction of Magnetic Flux around the CLL w/ Continuous Wire Outside of and Near Resonance

2.3.9 Three Layers of Periodic CLLs w/ Continuous-Wire (Parallel Orientation)

To measure the performance of multiple layers of the periodic CLLs with continuous wire in parallel orientation, three layers were simulated in HFSS as shown in Figure 2.45. The S-parameters of this structure are shown in Figure 2.46 and Figure 2.47. Additionally, the constitutive parameters for this multiple layer structure are shown in Figure 2.48. It is interesting to note that with multiple layers, the band exhibiting negative index of refraction seems to broaden. In addition, the constitutive parameter response curves seem to become more rounded with multiple layers as compared to the response with a single layer.

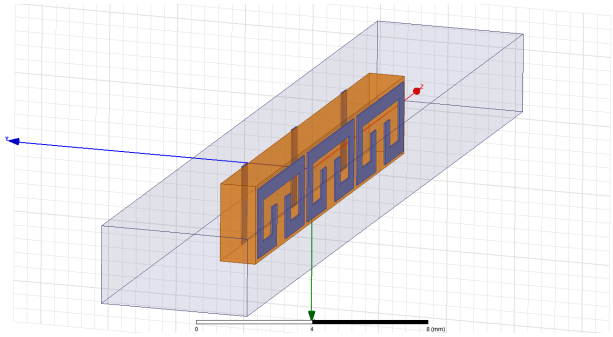

Figure 2.45: Three Layers of Periodic CLLs w/ Continuous-Wire (Parallel Orientation)

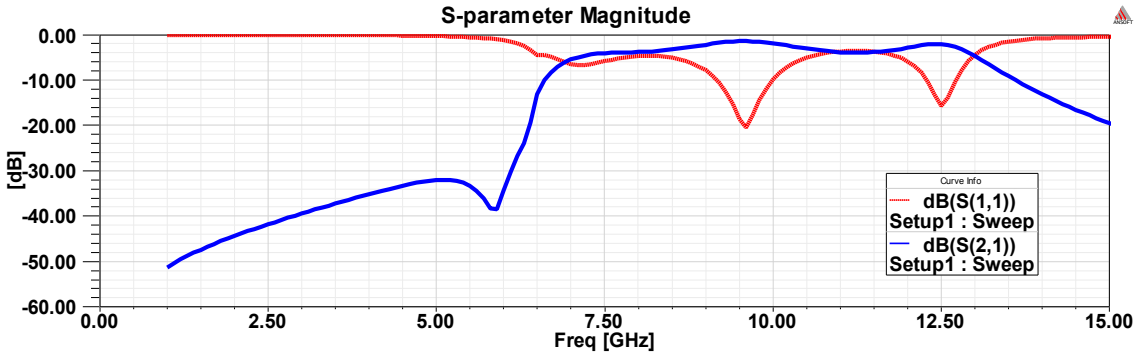

Figure 2.46: S-parameter Magnitude for Three Layers of Periodic CLLs w/ Continuous-Wire (Parallel Orientation)

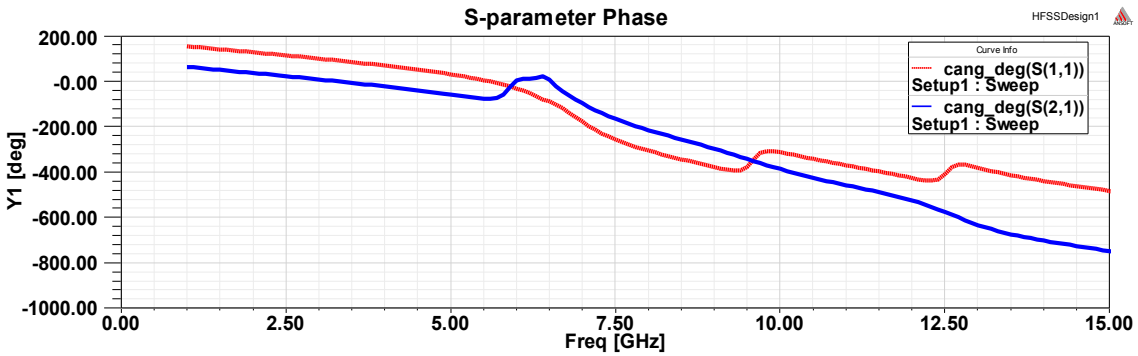

Figure 2.47: S-parameter Phase for Three Layers of Periodic CLLs w/ Continuous-Wire (Parallel Orientation)

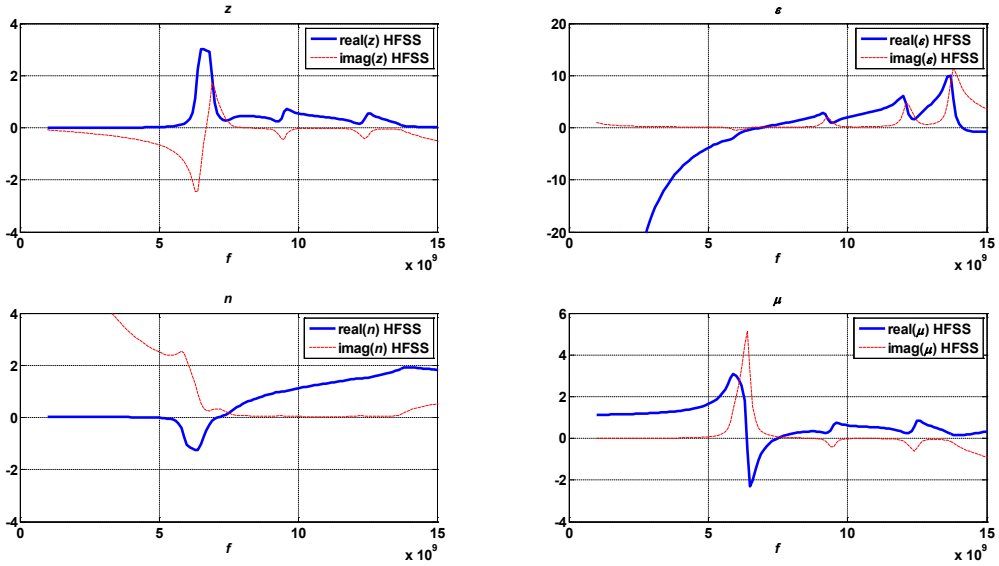

Figure 2.48: Constitutive Parameters for Three Layers of Periodic CLLs w/ Continuous-Wire (Parallel Orientation)

2.3.10 Periodic CLL w/ Continuous-Wire (Perpendicular to Propagation Orientation)

In addition to the parallel to propagation orientation, it is desirable to also achieve negative refraction in the perpendicular to propagation orientation. A periodic CLL with continuous-wire combination in the perpendicular to propagation orientation which was simulated in HFSS inside of the PEC/PMC unit cell configuration is shown in Figure 2.49. The simulated S-parameters are also shown in Figure 2.49. In this orientation, the 1st order S_{21} resonance is at 14.0GHz where the S_{21} transmission falls to -21dB. Interestingly, the 1st order resonance of the CLL in the perpendicular orientation is more than double in frequency the 1st order resonance of the CLL in

the parallel orientation. At the resonant frequency, a significant phase advance is seen in the S-parameter transmission phase response, shown in the bottom right corner of Figure 2.49. The calculated constitutive parameters are shown in Figure 2.50. The nature of the constitutive parameter response is fundamentally different from the responses that were calculated for the parallel to propagation orientation. For this structure, a negative index of refraction is calculated over a frequency band from 14GHz to 15GHz. The calculations show that the real part of permittivity and permeability are both negative at these frequencies. In this simulation, the Drude behavior for ε is not observed. It should be noted that the intrinsic impedance of this material configuration becomes very low near resonance. It should be noted that Im[ε]<0 and Im[μ]<0 are seen outside of resonance in this calculation, which breaks the passive material assumptions. However, Im[ε] and Im[μ] appear to return positive to meet the non-resonance passivity requirements as frequency becomes farther from resonance. For this reason, more analysis should be done on the parameter calculations in future works; however, the same parameter calculation technique was performed multiple times using the same retrieval method used for all other structures.

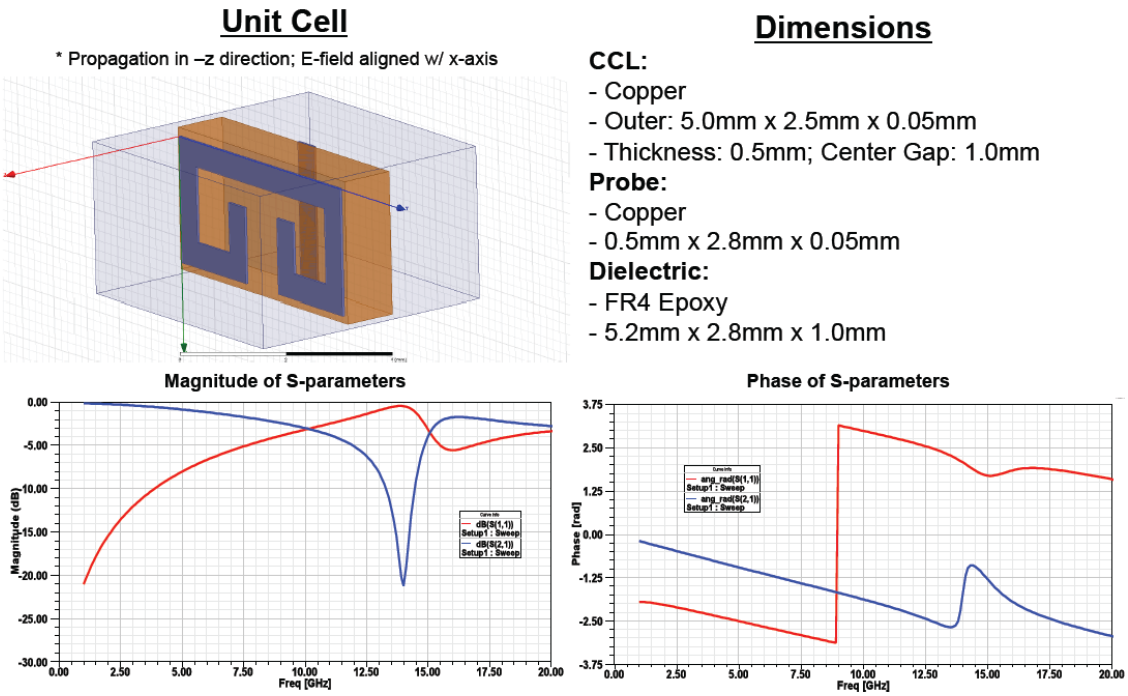

Figure 2.49: Structure and S-parameters for Periodic CLL w/ Continuous-Wire (Perpendicular to Propagation Orientation)

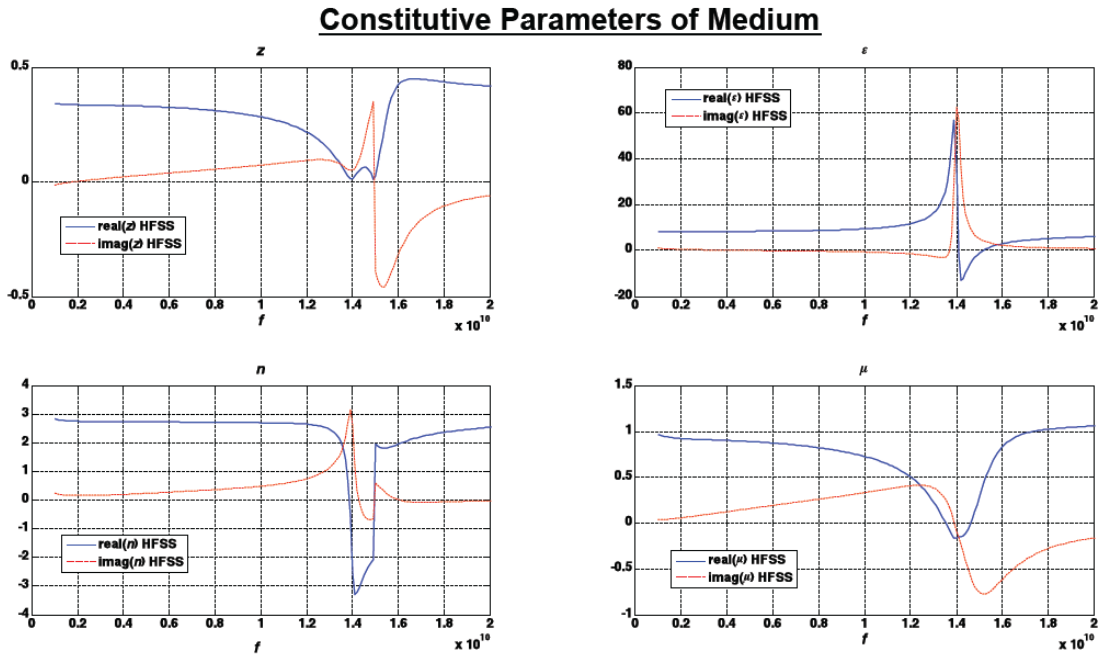

Figure 2.50: Constitutive parameters for Periodic CLL w/ Continuous Wire (Perpendicular to Propagation Orientation)

2.3.11 Artificial Homogeneous DNG Slab

For purposes of experimentation and comparison, a homogeneous dielectric slab was assigned constitutive parameter values of $\varepsilon_r = \mu_r = -1 \Rightarrow n = -1$. This slab with a depth of 1.3mm was also assigned very small, but non-zero, material loss. The slab was simulated in HFSS using the PEC/PMC boundary set-up to create a horizontally and vertically infinite array as was done in the previous metamaterial simulations. The simulated S-parameters were calculated, shown in Figure 2.51, and the constitutive parameters were extracted using the retrieval method. The extracted constitutive parameters, as shown in Figure 2.52, closely agree with the assigned parameters of the slab. It cannot be displayed in this paper, but when the electric field magnitude was animated in the time domain using HFSS, backwards wave propagation inside of the slab could be observed. While being an interesting test case in HFSS, this homogeneous DNG slab is not realizable in nature.

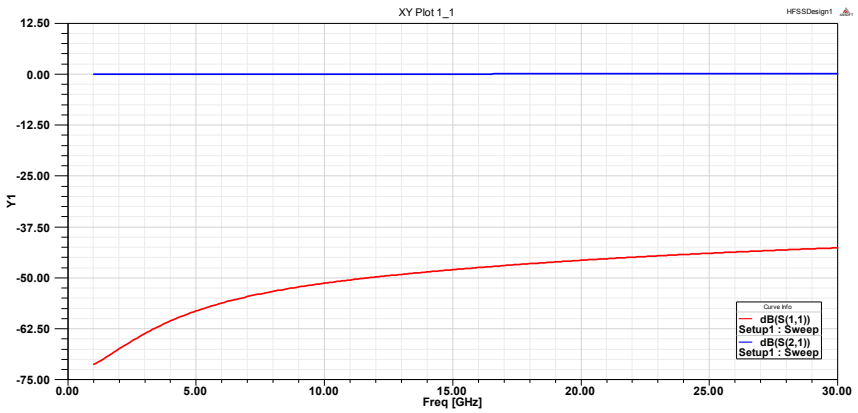

Figure 2.51: S-parameter Magnitude for Artificial Homogeneous DNG Slab Simulated in HFSS w/ Assigned Values of $\varepsilon_r = \mu_r = -1$

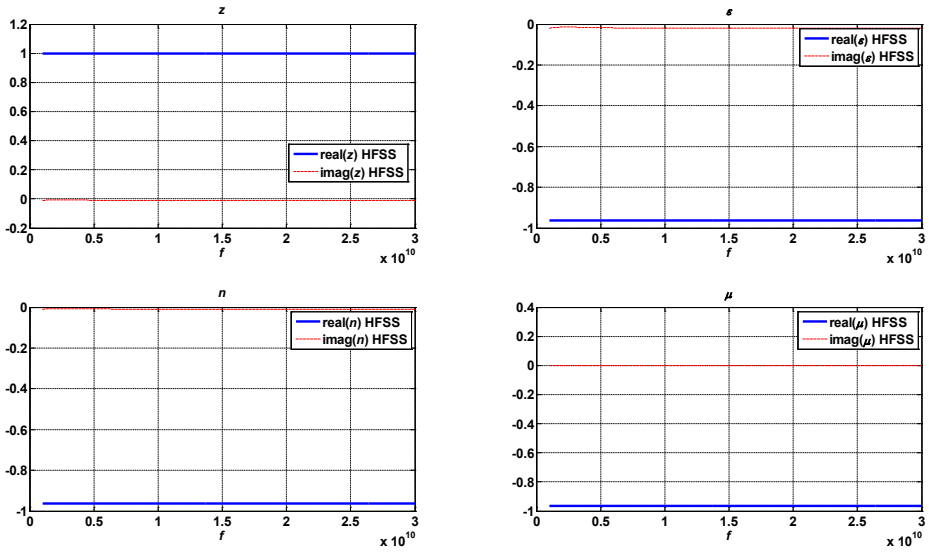

Figure 2.52: Constitutive Parameters for Artificial Homogeneous DNG Slab Simulated in HFSS w/ Assigned Values of $\varepsilon_r = \mu_r = -1$

2.4 Conclusion

The simulation results and extracted constitutive parameters of periodic metamaterial structures demonstrated in this chapter show good agreement with published theory. In addition, it was shown that the results follow the Lorentz and Drude models for permittivity and permeability.

While most studies focus on demonstrating material parameters for SRR metamaterials, this study demonstrated that the CLL, a less common variant of the SRR, also shows the ability to produce negative μ in the resonant frequency band. It was further demonstrated that the CLL produces negative refractive index over a narrow frequency band when paired with a metallic

continuous wire. It was also shown that DNG behavior was not demonstrated for the CLL paired with cut metallic wire, indicating that continuous wire was required for negative refraction with the CLL.

In addition, the retrieval technique for the CLL with continuous wire shows negative refraction at two different frequencies for the parallel and perpendicular orientations. This observation can be explained by the fact that the resonant frequency for the CLL differs based on orientation of the cell relative to an incident wave. This behavior could be used to engineer a device that can demonstrate negative refraction in two different distinct frequency bands based on orientation.

While demonstrating relatively high losses in the resonant region, it has been shown that the CLL is a robust magnetic metamaterial inclusion that can be used instead of the more common SRR. One advantage is that the CLL inclusions are generally larger than the Smith SRR that resonates at the same frequency, allowing for easier fabrication as frequency is scaled upwards.

Chapter 3: Random Metamaterial Structures

3.1 Introduction

It has been proposed that electromagnetic metamaterials—composite structured materials, formed either from periodic or random arrays of scattering elements—should respond to electromagnetic radiation as continuous materials, at least in the long wavelength limit [34]. However, nearly all of the research and analysis of metamaterials has been on artificially structured periodic inclusions that can be expressed in terms of homogenized material parameters [10]. However, there is nothing fundamental that limits metamaterial structures to consist of periodic inclusions [35, 34]. In this chapter, metamaterial structures with aperiodic or random inclusions will be analyzed. Despite the complex physical structure of metamaterial structures with inclusions that are randomized in position and orientation, the effective medium can be analyzed using a small set of averaged parameters, such as electric permittivity, magnetic permeability, refractive index, and wave impedance. The unit elements used in these aperiodic or random metamaterial structures are copper SRRs or CLLs, which are conducting resonant inclusions as seen in previous chapters of this work. Each inclusion is sub-wavelength by a factor of three or greater. Using common S-parameter retrieval techniques, it is possible to analyze the reflection and transmission coefficients calculated from transfer matrix simulations on finite lengths of electromagnetic metamaterials to determine the effective permittivity (ϵ) and permeability (μ) of the medium [34], regardless of internal periodic or aperiodic structure.

Many existing periodic metamaterial structures are anisotropic, but some practical applications require isotropic media. Attempt to create randomized structures with the same negative refractive properties as a periodic metamaterial structure, but with greater bandwidth, and less propagation loss. Much work has been done to optimize unit cell (SRR or CCL) designs, but little research has been done to study the effect of variations in cell arrangement on metamaterial properties.

The electromagnetic response of each CLL or SRR inclusion is very much orientation dependent with respect to an incoming incident plane wave. For this reason, the electromagnetic response of a random or aperiodic metamaterial structure can be viewed as a metallic or metallic-dielectric mixing problem in effective medium theory. Unit elements of periodic metamaterial structures are assumed to have identical electromagnetic properties. Conversely, the properties of the randomized metamaterial structure are an averaged composite of its constitutive elements which all vary by position and orientation. This analysis seeks to better understand the macroscopic permeability, permittivity, and other electromagnetic material properties of composite metamaterial structures consisting of many random or aperiodic elements.

3.2 Random Media Theories

3.2.1 Effective Medium Theory

Effective medium theory (EMT) seeks to describe the macroscopic properties of a composite medium made of multiple principle components [36]. At the constituent microscopic level, the values of properties defining the material can vary wildly and are very inhomogeneous. EMTs have been developed that can produce acceptable approximations to describe useful parameters and properties of the composite material as a whole. In this sense, effective medium approximations are generally descriptions of a composite material based on the known properties and the relative fractions of its constitutive components. Often times the effective medium theory is used because precise calculations of the many constituent values is nearly impossible. This is especially true for solving Maxwell's equations for a complex medium that is electrically large. Only recently has it become feasible to run numerical simulation of Maxwell's equations to solve local electric and magnetic fields, current distributions, and other microscopic quantities of interest for electromagnetic structures in a relatively efficient manner. Before this, effective medium theory had to be relied on much more heavily. However, these theories have limitations and generally ignore interactions between elements, limiting the accuracy of the models. The EMT models are generally most accurate when the particle size $r \ll \lambda$, otherwise scattering effects become much more significant and must be taken into account. For metamaterials comprised of conductive and possibly resonant elements for which adjacent element interactions

cannot always be ignored, analytical homogenizing mixing models are not always reliable or applicable [10]. Before reviewing the results of finite element simulations of several randomized and aperiodic metamaterial structures, several of the conventional EMT mixing models will be reviewed and analyzed.

3.2.2 Bruggeman Mixing Model

One of the most popular EMT models is Bruggeman's mixing model, which applies to mixtures of two or more media and makes no distinction between species, such as host or inclusion [37]. This model seems to be an appropriate description of the metamaterial structures that this study seeks to analyze. To determine the effective permeability of the macroscopic metamaterial structure, each unit-cell is assigned a bulk permeability based on its orientation relative to an incoming plane wave. Knowing the proportion of each unit-cell orientation in the composite medium, the macroscopic effective permeability can be solved for algebraically in a straightforward manner using the equation below. The same process can be used to solve for effective magnetic permeability using Equation 3.2 below where ε is substituted for μ. In this manner, if the constitutive parameters of individual unit-cells are known for a given composite medium, an approximation for the constitutive parameters of the medium can be calculated using the Bruggeman mixing model [38].

$$\sum_{i=1}^{n} f_i \frac{\varepsilon_i - \varepsilon_{eff}}{\varepsilon_i + 2\varepsilon_{eff}} = 0 \tag{3.1}$$

$$\sum_{i=1}^{n} f_i \frac{\mu_i - \mu_{eff}}{\mu_i + 2\mu_{eff}} = 0 \tag{3.2}$$

where μ_i and ε_i are the parameters of the constituent materials and f_i is the filling fraction of each element such that $\sum_{i=1}^{n} f_i = 1$.

3.2.3 Maxwell-Garnett Theory

The Maxwell-Garnett (MG) model is a common mixing model derived from the Clausius-Mossotti relation, in which a sufficiently dilute composite material is assumed such that a hierarchy of macroscopic and microscopic fields can be macroscopically defined [39]. Traditionally, the MG has been used to analyze effective mediums consisting of metal dispersions such as colloids, cermets, and discontinuous metal films [40]. However, the

underlying assumption of diluteness becomes suspect when investigating metamaterials which are composed of closely packed and strongly resonant structures [37].

$$\left(\frac{\varepsilon_{eff}-\varepsilon_m}{\varepsilon_{eff}+2\varepsilon_m}\right)=\delta_i\left(\frac{\varepsilon_i-\varepsilon_m}{\varepsilon_i+2\varepsilon_m}\right) \tag{3.3}$$

$$\varepsilon_{eff}=\varepsilon_m\frac{2(1-\delta_i)\varepsilon_m+(1+2\delta_i)\varepsilon_i}{(2+\delta_i)\varepsilon_m+(1-\delta_i)\varepsilon_i} \tag{3.4}$$

where ε_{eff} is the effective dielectric constant of the medium, ε_i is the one of the inclusions, and ε_m is the one of the matrix; δ_i is the volume fraction of the inclusions [10].

3.2.4 Clausius-Mossotti Relation

Another EMT related to Maxwell Garnett theory is the Clausius-Mossotti relation, developed by Italian physicist Ottaviano-Fabrizio Mossotti in 1850, which analyzes the relationship between the dielectric constants of two different media based on the material's atomic polarizability. The Clausius–Mossotti law applies to the dielectric constant of a dielectric that is perfect, homogeneous and isotropic [41]. The index of refraction of a mixture is not an average of its constituent indexes, but given in terms of the sum of the polarizabilities [42]. The Clausius-Mossotti (CM) equation states as follows

$$\text{Single solution: } 3\left(\frac{n^2-1}{n^2+2}\right)=N\alpha \tag{3.5}$$

$$\text{Mixture of Solutions: } 3\left(\frac{n^2-1}{n^2+2}\right)=\sum_i N_i\alpha_i \tag{3.6}$$

where N is the number of particles per unit volume; α is the atomic polarizability and n is the refractive index. As shown in the CM Equations 3.5 and 3.6, if the material is a dense mixture of several components, each will contribute to the polarization of the composite material [43]. When the electrically small (or atomic) unit elements are densely packed together, there will be strong interactions between neighboring elements creating local electric and magnetic fields. This description was derived from atomic gases and mixtures; however, it is derived from Maxwell equations and appears to provide insight into interactions between microscopic metamaterial elements in a given medium.

3.3 Simulation Constraints

Simulation is quite difficult using commercially available electromagnetic full-wave simulation software, such as HFSS, CST, and FEKO. Initial simulations required >100GB of RAM. Even with powerful hardware, simulations can take >24 hours. Some simulations are too large for successful completion on available hardware. Super-computer or large-scale distributed cluster access is desired for future work.

3.4 Random Media Simulation Technique

Faced with the computational challenges highlighted above, a quasi-random solution is proposed to approximate the performance of random metamaterial structures. The common S-parameter equations being used require a normally incident plane wave that scatters from a semi-infinite dielectric-magnetic slab of depth *d* in free-space [44]. If the composite material block in HFSS simulation is not semi-infinite, most of the radiation is scattered and not captured by the receive wave port. This drastically reduces the transmission magnitude, which directly affects the constitutive parameter calculation. In an extremely lossy structure, phase data can also become inaccurate if magnitude becomes sufficiently small. For this reason, periodic boundary conditions are advantageous for accurate material parameter extraction, because all of the transmitted energy not lost due to intrinsic material losses is received by the receive wave port. This would also be true to a metallic waveguide with vertical and horizontal PEC boundaries. However, the TEM modes will not propagate in a metallic waveguide, which creates a non-free space-like situation and changes the constitute parameter retrieval equations.

The solution proposed in this work is to simulate an electrically large finite block of random metamaterial using PEC vertical boundaries and PMC horizontal boundaries, effectively creating an infinite parallel plate waveguide. Initially, this approach seems counterintuitive because the structure under test is being infinitely arrayed in a periodic manner in the horizontal and vertical dimensions. However, if the block of random metamaterial elements is large enough, it should closely approximate an infinite random block of metamaterial. It is assumed that significant interactions between each microscopic element, such as a CLL or SRR, will be limited to local neighboring elements. If this assumption is correct, the PEC/PMC large cell simulations performed in HFSS will accurately simulate the S-parameters for random metamaterial media.

As the number of random metamaterial elements in an HFSS PEC/PMC simulation linearly increases, the required simulation time and required RAM for the computational simulation exponentially increases. The goal of this study is to simulate a number of different random metamaterial structures, and the available computational resources are limited, so methods that minimize simulation time are greatly preferred. In addition, by definition a random structure will follow a given random probability distribution. To perform a complete study, results from many random samples should preferably be averaged together.

In electrically small PEC/PMC unit-cell simulations which is analogous to an infinite parallel plate waveguide, only 1st order modes must be accounted for. However, when the size of the unit-cell is increased above $\lambda/2$ [45], higher order modes must be accounted for. Generally, an electrically large simulation of many metamaterial elements containing higher-order modes is too computationally intensive based on available hardware. In addition, the standard S-parameter retrieval techniques used in this study are most accurate when considering only 1st order modes [19].

Due to the constraints described above, a difficult trade-off is faced in terms of the number of random or aperiodic elements used in a given HFSS finite-element simulation. Larger blocks consisting of a greater number of elements are desired to more closely approximate an infinitely random structure; however, the computational constraints in terms of simulation time and computational power increase exponentially with the number of simulated metamaterial elements reaching the limits of available computational capabilities.

3.5 Random Metamaterial Simulations

3.5.1 Random Single-Cut Circular SRR Structure

The analysis of random metamaterials will begin with a straightforward structure consisting of randomly oriented and randomly positioned non-intersecting circular single-cut split ring resonators. As discussed in the earlier chapter on periodic metamaterial structures, the cut in the metallic ring transforms it into a SRR, which allows for a negative magnetic permittivity response at the resonant frequency of the loop. Each loop is sub-wavelength with a diameter of 4 mm, which is ~$\lambda/6$ of the resonant frequency. The macroscopic dimensions of the block of random circular SRRs is approximately 20mm x 20mm x 20mm. On average, the infinitely

arrayed random block consists of approximately 35 randomly oriented and positioned circular SRRs, as shown in Figure 3.1 and Figure 3.2. Based on the S-parameters results of the simulated random block of circular elements, the resonant frequency of the structure is at 11.8GHz. At the resonant frequency, transmission through the random metamaterial structure, defined by S_{21}, drops to -16.9dB, shown in Figure 3.3. Conversely, reflection of this structure increases ~15dB at the resonant frequency to a maximum of roughly ~-2dB. The S-parameter response observed for this structure is essentially that of a RF band reject surface of filter. In addition, there is phase advance at the resonant frequency, shown in Figure 3.4. Interestingly, the S_{21} phase is relatively flat over a wide frequency band, which is not seen in other simulations done in this study.

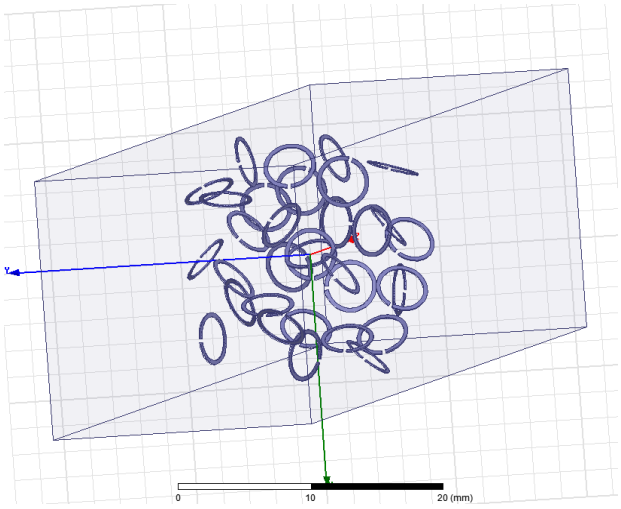

Figure 3.1: Random Block of Circular SRRs (Propagation in the –z; PEC in ±x; PMC in ±y)

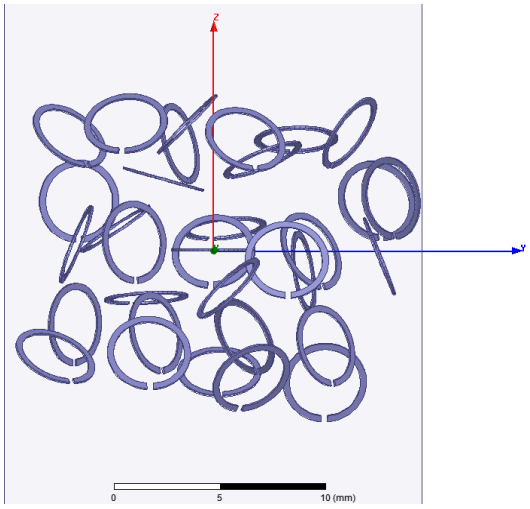

Figure 3.2: Top View Random Block of Circular SRRs (Propagation in the –z; PEC in ±x; PMC in ±y)

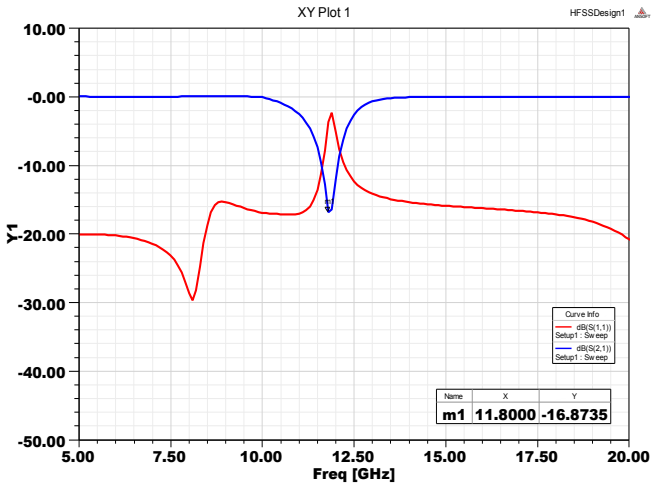

Figure 3.3: S-parameter Magnitude Response for Random Block of Circular SRRs

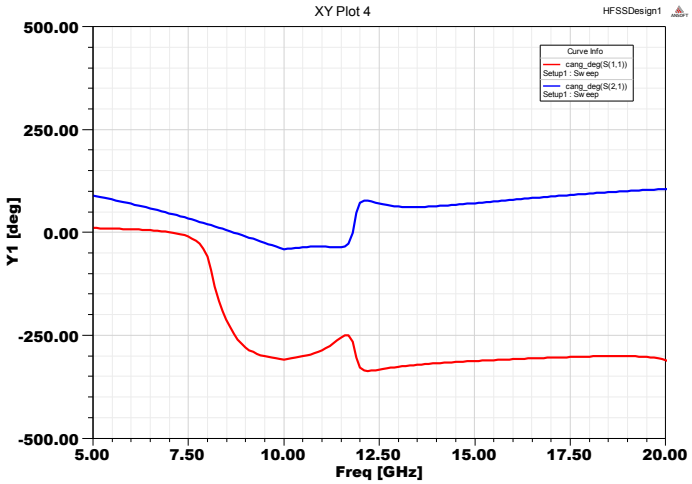

Figure 3.4: S-parameter Phase Response for Random Block of Circular SRRs

3.5.2 Thin Layer of Random CLLs

The next case that will be analyzed is a thin layer of random oriented and positioned CLLs w/ wire having a depth of only one or two unit-cells, shown in Figure 3.5, Figure 3.6, and Figure 3.7. Initially, a thin layer of random metamaterial was simulated because it contains a smaller number of unit-cells and can simulate in substantially less time. In addition, this study seeks to observe the effect of thickness of depth on the random metamaterial block. As shown in the S-parameter results seen in Figure 3.8 below, S_{21} transmission is very strong over a wide frequency, except at the resonance. This structure resonates at ~8.3 GHz, and the drop in transmission magnitude to -7.5dB is relatively weak compared to other structures analyzed in

this study. This result is logical because the resonance is presumably weaker at random orientations that are not perpendicular or parallel to the direction of propagation or electric field. In addition, the lack of depth gives the metamaterial less distance to interact with the incident wave. The relatively small amount of S_{21} phase advance in Figure 3.9 below supports this notion.

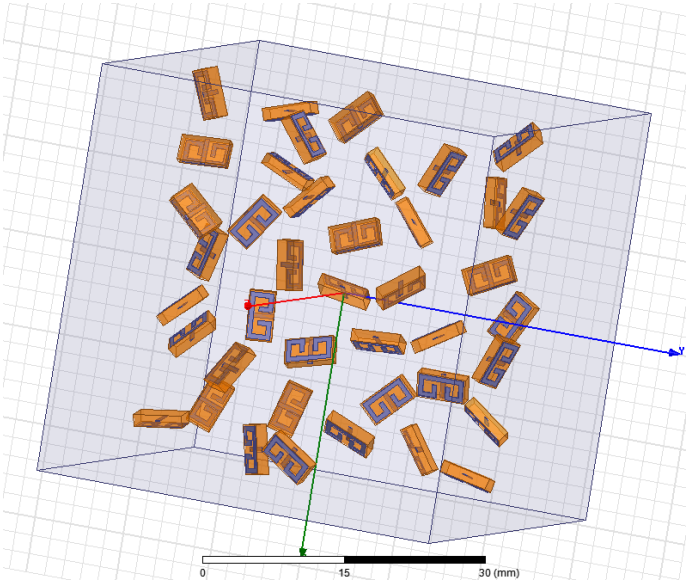

Figure 3.5: Thin Layer of Random CLLs w/ Wire (Prop in –z; PEC in ±x; PMC in ±y)

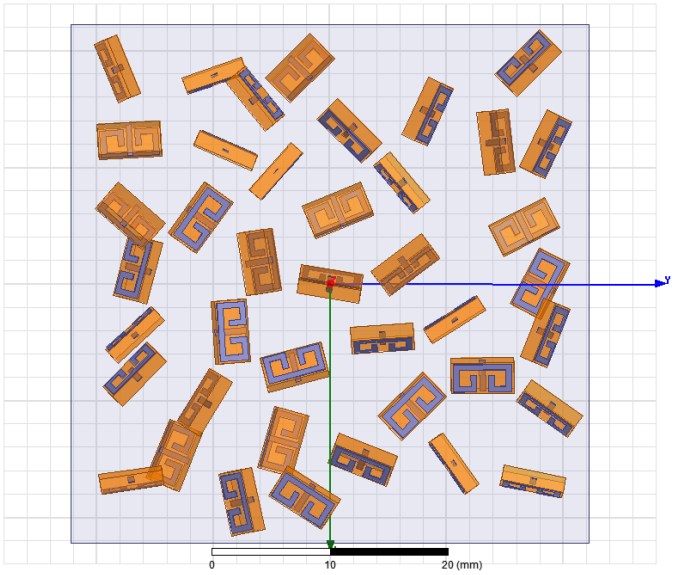

Figure 3.6: Front View of Thin Layer of Random CLLs w/ Wire (Prop in –z; PEC in ±x; PMC in ±y)

Figure 3.7: Side View of Thin Layer of Random CLLs w/ Wire (Prop in –z; PEC in ±x; PMC in ±y)

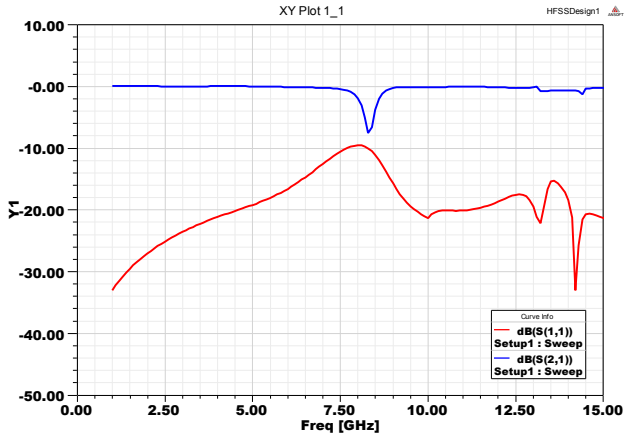

Figure 3.8: S-parameter Magnitude of Thin Layer of Random CLLs w/ Wire

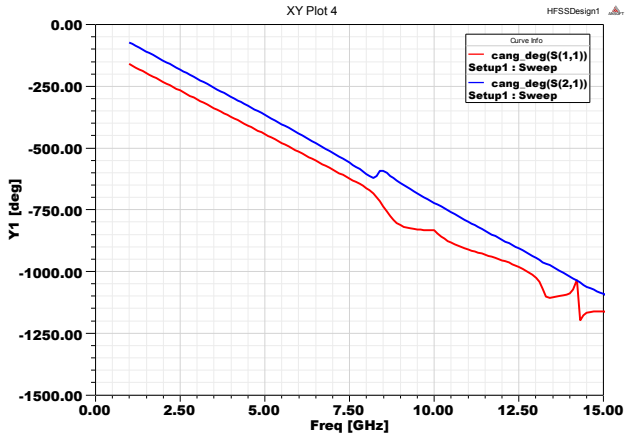

Figure 3.9: S-parameter Phase of Thin Layer of Random CLLs w/ Wire

The constitutive parameters calculated for this thin random CLL structure, shown in Figure 3.10, weakly follow the Lorentz-Drude model; however, the resonances are not strong enough to result in exotic properties, such as negative index of refraction. At the resonance there is a small dip in μ and a small increase in ε, but these deviations are not large enough to drastically change the index of refraction.

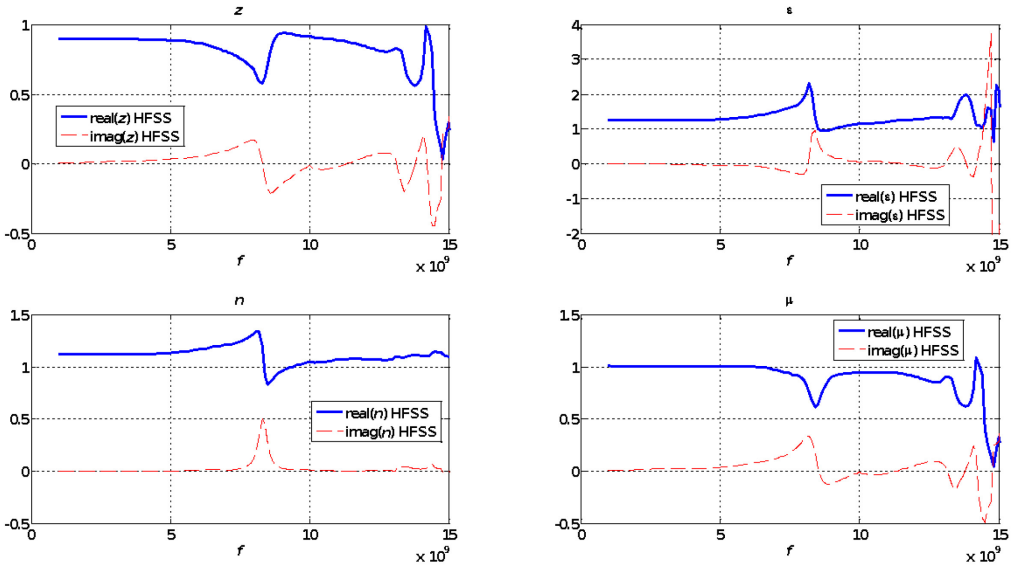

Figure 3.10: Constitutive Parameters of Thin Layer of Random CLLs w/ Wire

3.5.3 Thick Random Block of CLLs

The most natural random metamaterial structure analyzed in this chapter is an electrically large block of dense randomly oriented and randomly positioned CLLs with an electrically large thickness, shown in Figure 3.11. Additional views of the structure are shown in Figure 3.12 and Figure 3.13. The adaptive meshing used for simulation in HFSS is shown in Figure 3.14 and Figure 3.15. This CLL structure is most representative of CLLs being randomly distributed to box or confined region. The dimensions of this random metamaterial structure are 31.75mm x 31.75mm x 27.5mm consisting of 59 CLL metamaterial elements. With the increase in depth to $\sim 3/4\,\lambda$, compared to the previous block that was analyzed, the strength of the resonance and hence drop in S_{21} transmission is much greater, decreasing -30.5dB at 8.4GHz as shown in Figure 3.16. In addition, the S-parameter phase response is shown in Figure 3.17. This is the lossiest resonance observed in random metamaterial structures presented in this thesis.

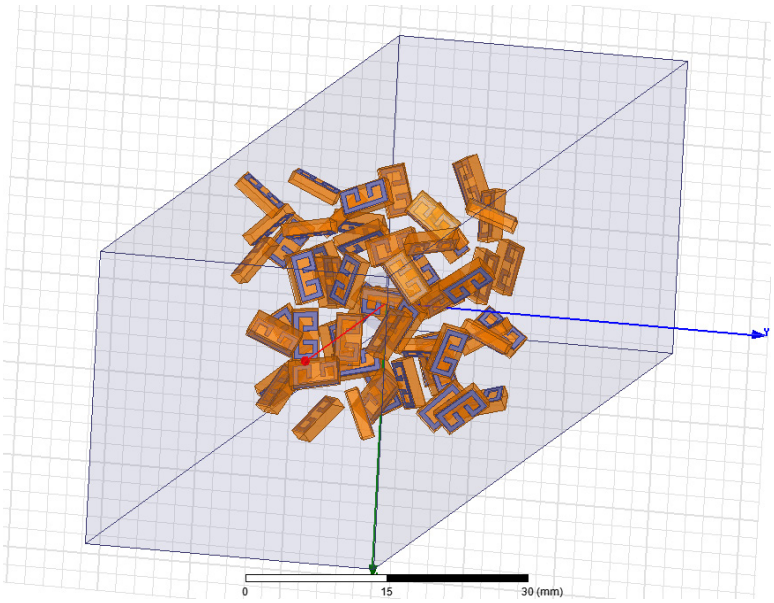

Figure 3.11: Random CLL Metamaterial Structure (Prop in –z; PEC in ±x; PMC in ±y)

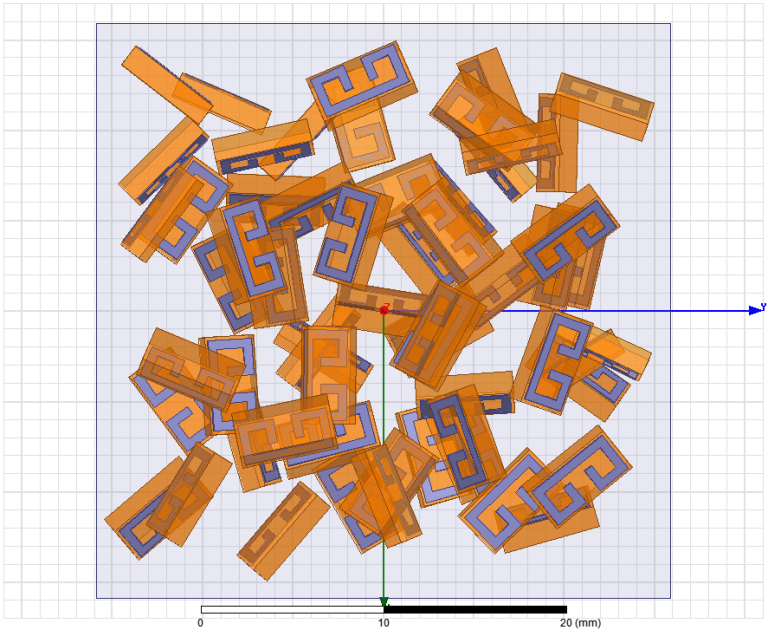

Figure 3.12: Front Random CLL Metamaterial Structure (Prop in –z; PEC in ±x; PMC in ±y)

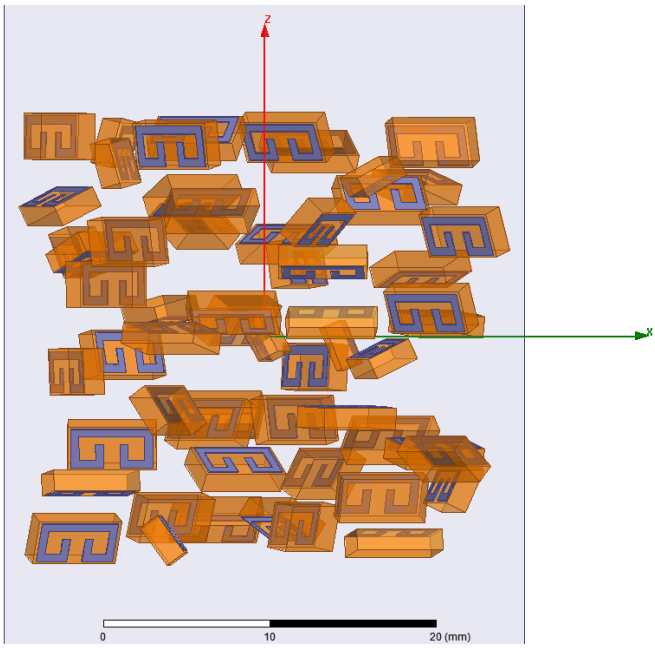

Figure 3.13: Top View Random CLL Metamaterial Structure (Prop in –z; PEC in ±x; PMC in ±y)

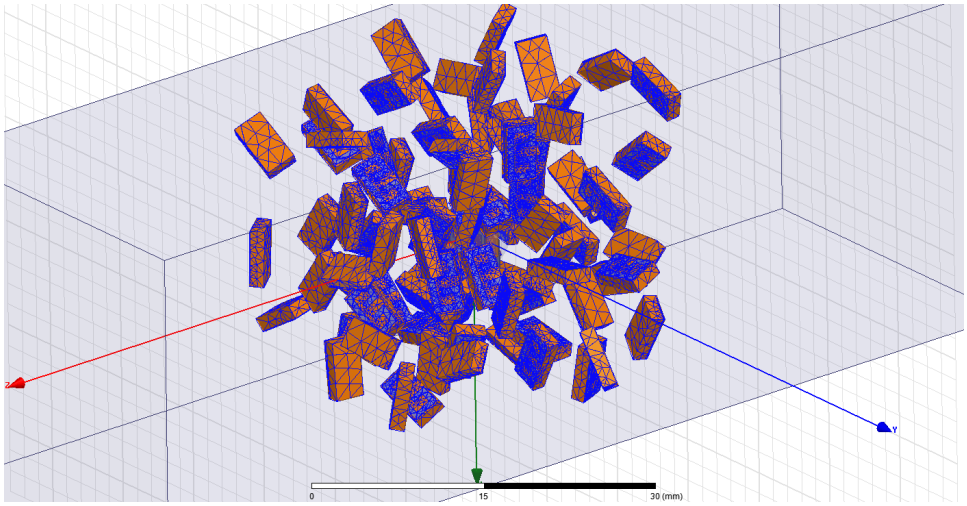

Figure 3.14: Adaptive Meshing in HFSS of Random CLL Metamaterial Structure

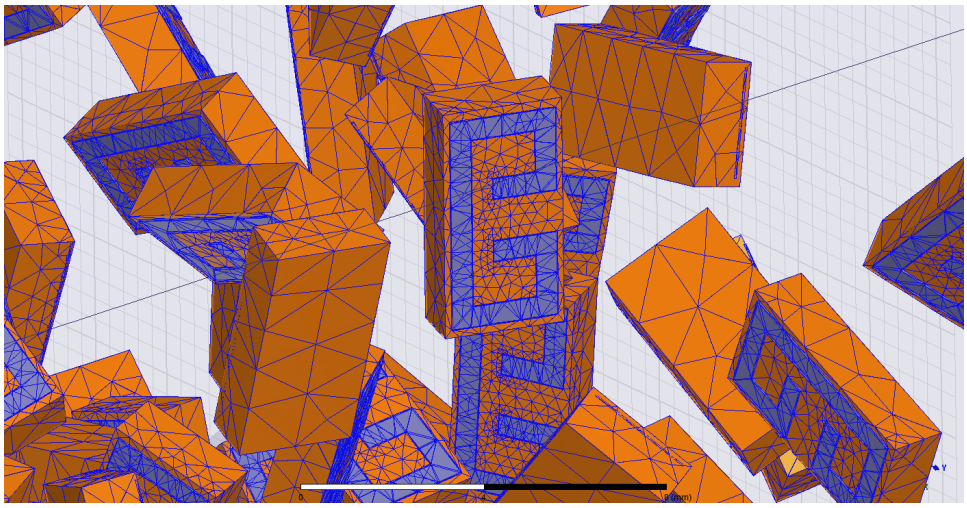

Figure 3.15: Adaptive Meshing in HFSS of Random CLL Metamaterial Structure (Zoomed-In)

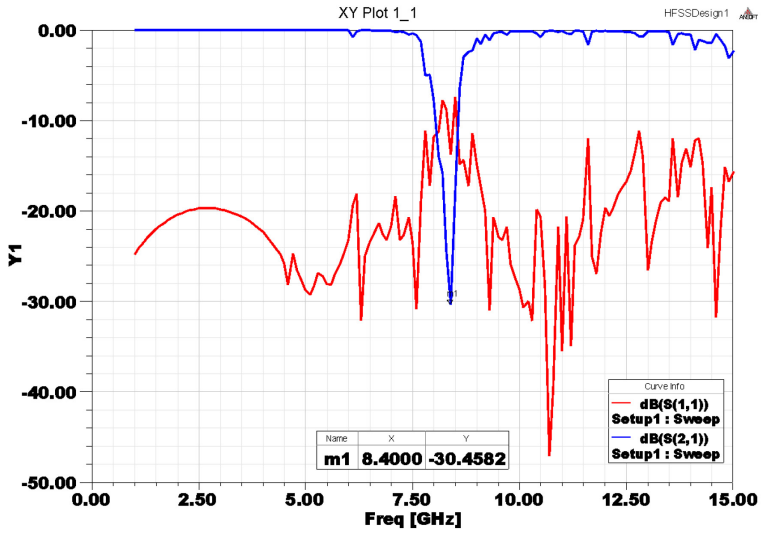

Figure 3.16: S-parameter Magnitude Response for Random CLL Metamaterial Structure

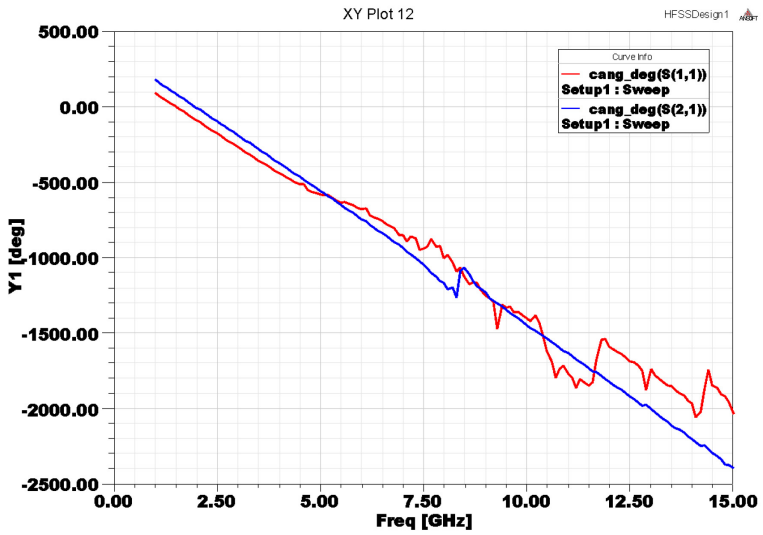

Figure 3.17: S-parameter Phase Response for Random CLL Metamaterial Structure

3.5.4 Planar Incident Random CLLs

For purposes of experimentation and to investigate different aspects of randomness on metamaterial and effective medium structure, several pseudo random metamaterial structures were simulated and compared to the structures with completely random orientation and position of microscopic unit-elements. One idea was to fix certain dimensions of position or orientation while allowing other dimensions to follow a randomized distribution. The first example is in the figure shown below. Each CLL in the structure is fixed such that it will be perpendicularly incident to the incoming plane wave while being completely random in position and radial rotation, as shown in Figure 3.18. Additional views are shown in Figure 3.19 and Figure 3.20. This was done under the hypothesis that performance of each local random element may improve if each element is perpendicular to the incident wave, such as in many periodic metamaterial simulations.

The dimensions of this metamaterial block are 45mm x 45mm x 13.4mm consisting of 94 CLL w/ wire elements with a piece of FR4 dielectric attached to each CLL. Same as the other random simulations, each inclusion has dimensions 5.4mm x 2.8mm x 1.3mm. The resonant frequency of this structure, as determined by S-parameter simulation results, is 8.2GHz. The S_{21} transmission is -17.0dB at this resonant frequency, as shown in Figure 2.21. At this frequency, the 13.4mm depth of the block is ~λ/3. The maximum dimension of each inclusion is ~λ/7. This structure also appears to have a 2nd weaker resonance around 14.2GHz where transmission drops to -6.0dB, as shown in Figure 2.21 below. The S_{21} transmission phase results for this structure

show very limited phase reversal, shown in Figure 2.22. However, the S_{11} reflection phase for this structure shows unnatural behavior including phase reversal.

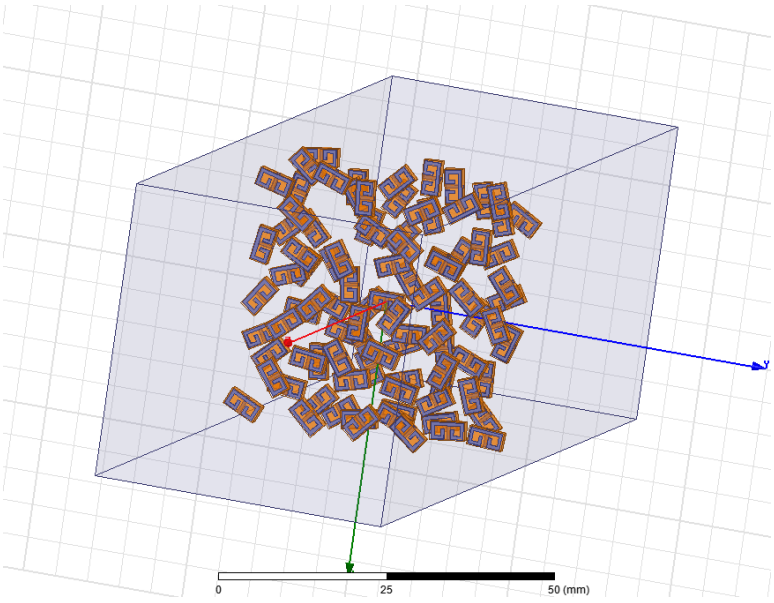

Figure 3.18: Planar Incident Random CLLs w/ Wire (Prop in –z; PEC in ±x; PMC in ±y)

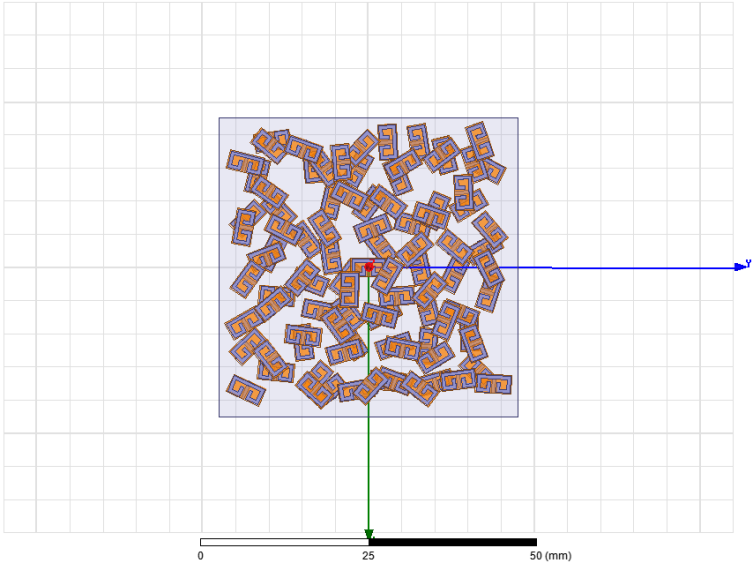

Figure 3.19: Front View Planar Incident Random CLLs w/ Wire (Prop in –z; PEC in ±x; PMC in ±y)

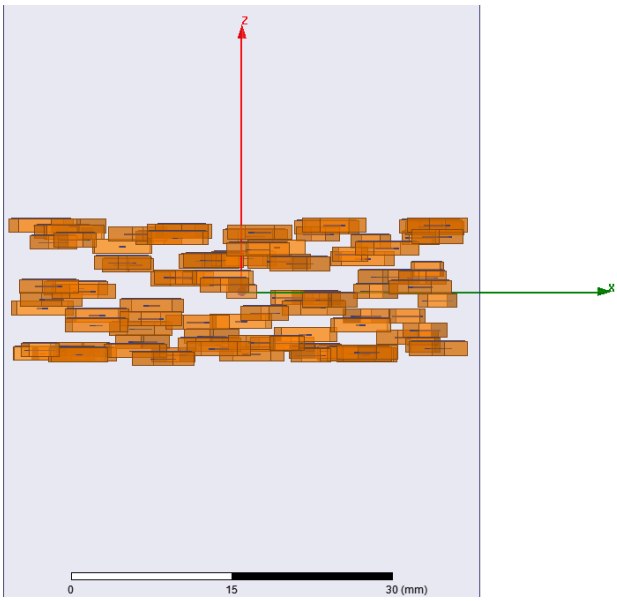

Figure 3.20: Top View Planar Incident Random CLLs w/ Wire (Prop in –z; PEC in ±x; PMC in ±y)

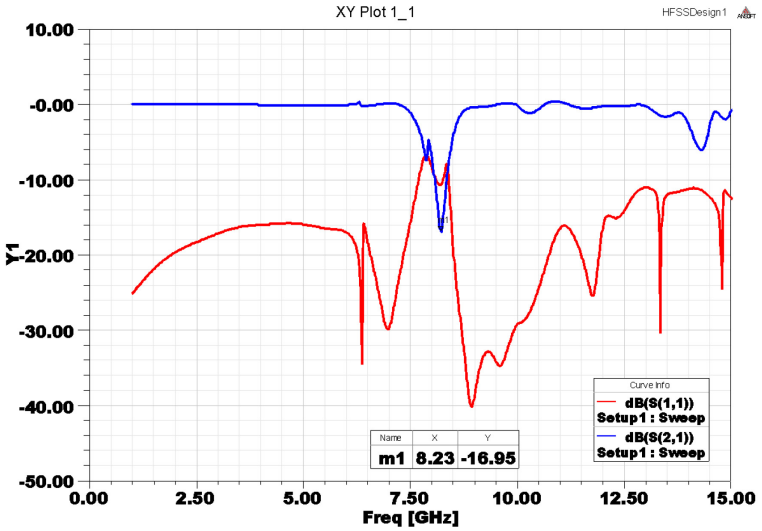

Figure 3.21: S-parameter Magnitude for Planar Incident Random CLLs w/ Wire

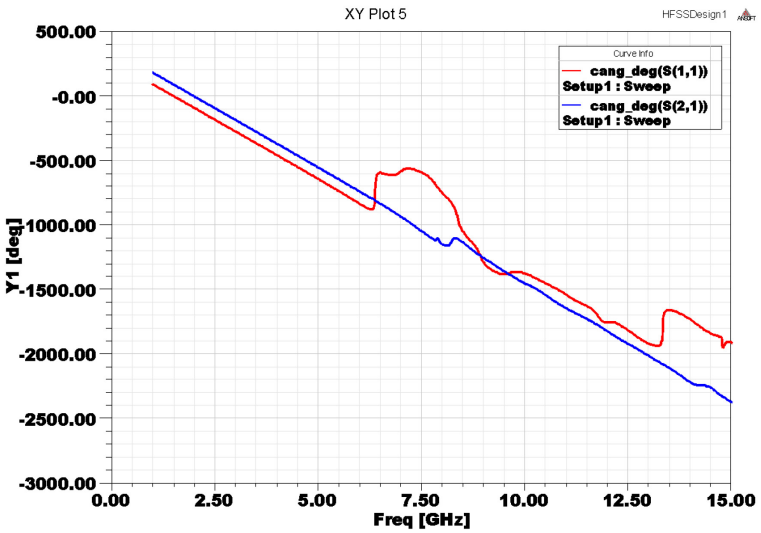

Figure 3.22: S-parameter Phase for Planar Incident Random CLLs w/ Wire

The constitutive parameter calculations, shown in Figure 2.23, should be viewed with a degree of skepticism because future work needs to be done to verify the validity of the parameter calculations in this situation. While these parameter calculations should be viewed with skepticism, they will be analyzed. The constitutive parameter extraction for this random metamaterial structure do not yield negative parameters; however, it does produce some interesting results. At the point of resonance, the index of refraction sharply increases from n = ~1 to n= ~3. This sort of composite metamaterial structure could provide a medium for which an increased index of refraction is desired above a specific resonant frequency. In addition, μ spikes to a value above 6 just above 10GHz, which could be useful for many high-μ applications in engineering.

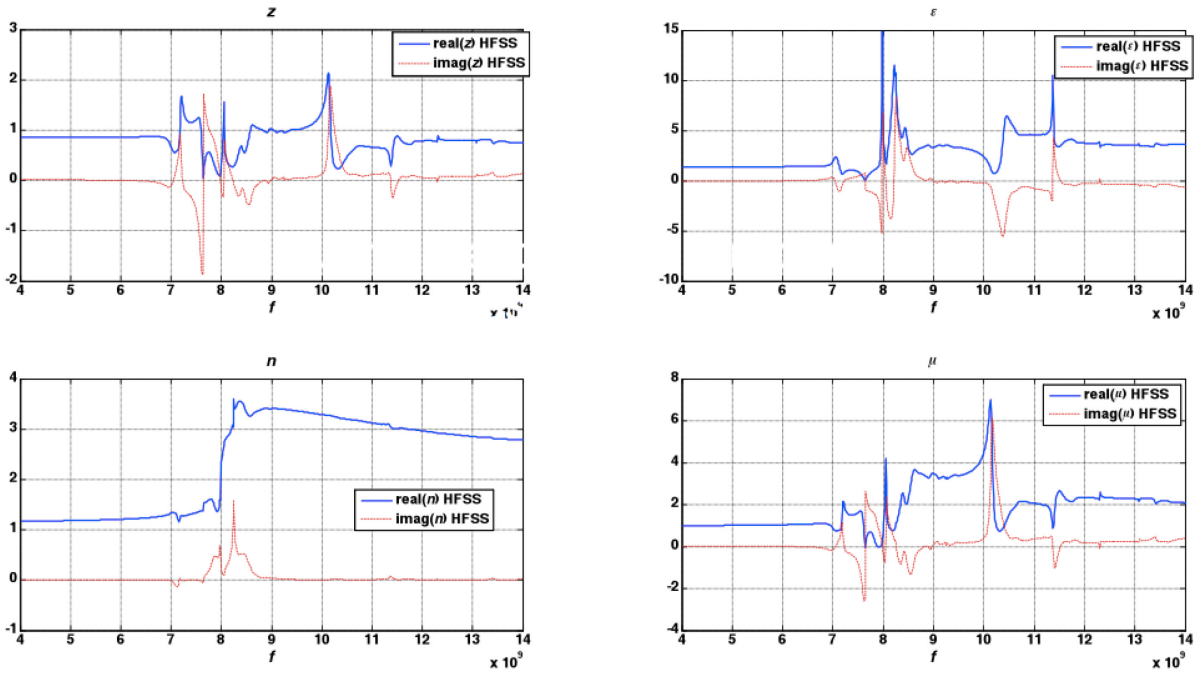

Figure 3.23: Constitutive Parameters for Planar Incident Random CLLs w/ Wire

3.5.5 Thick Random Block of CLLs w/o Periodic Boundary Conditions

The devised method of simulating electrically large blocks of random metamaterial inclusions with periodic boundary conditions to approximate an infinite random array has drawn skepticism by some. To help settle doubts, a large random block of 227 randomly positioned and oriented CLLs was simulated in HFSS with non-periodic radiation boundaries for comparison, shown in Figure 3.24. Additional views of this structure are shown in Figure 3.25 and Figure 3.26. The simulation results of the S-parameter magnitude without periodic boundary condition, shown in Figure 3.27, show a deep transmission resonance of -35.4dB at 8.4GHz. This is the same resonant frequency shown in simulations using the PEC/PMC periodic boundary technique, such as in Figure 3.16. To meet HFSS simulation guidelines, the perfectly absorbing radiation boundaries are greater than λ/4 away from the nearest CLL at the resonant frequency of 8.4GHz. Due to the free space gaps in between the CLLs and the radiation boundaries, diffraction effects can be seen in the S-parameter magnitude results in Figure 3.27. The presence of a strong resonance at 8.4GHz both with and without the periodic boundary conditions suggest that this is

a physically realizable resonance and not an artificial artifact of the HFSS simulation technique. The simulated S-parameter phase response for this structure is shown in Figure 3.28.

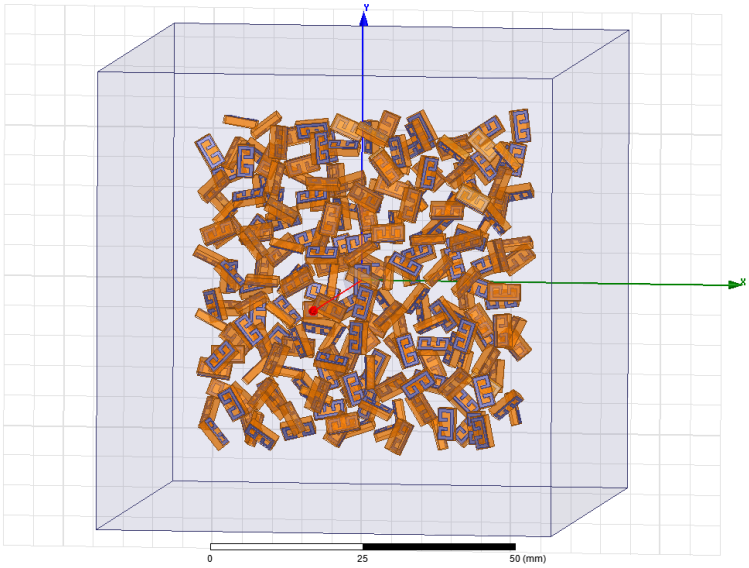

Figure 3.24: Thick Random Block of CLLs w/o Periodic Boundary Conditions (Prop in –z; Radiation Walls in ±x and ±y)

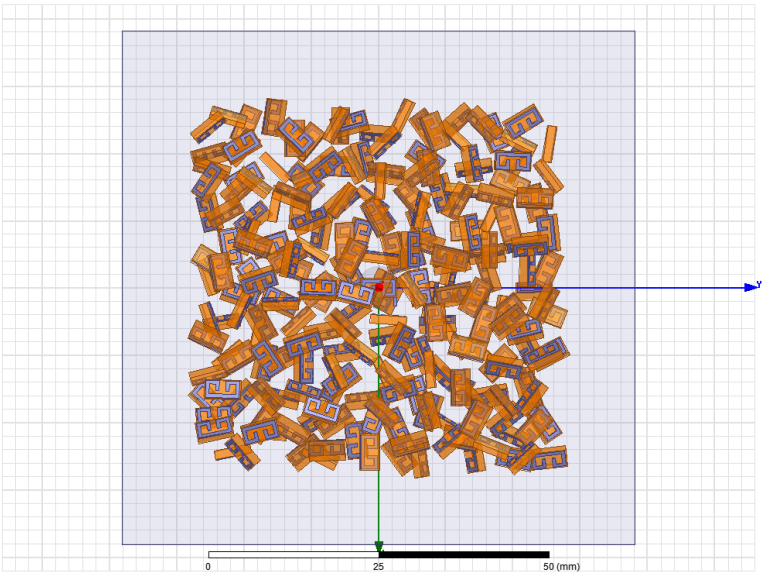

Figure 3.25: Front View of Thick Random Block of CLLs w/o Periodic Boundary Conditions (Prop in –z; Radiation Walls in ±x and ±y)

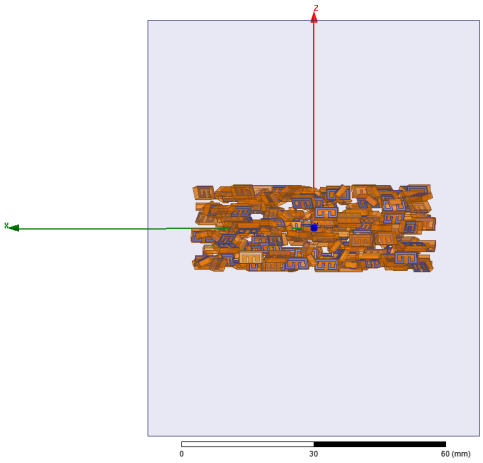

Figure 3.26: Top View of Thick Random Block of CLLs w/o Periodic Boundary Conditions (Prop in –z; Radiation Walls in ±x and ±y)

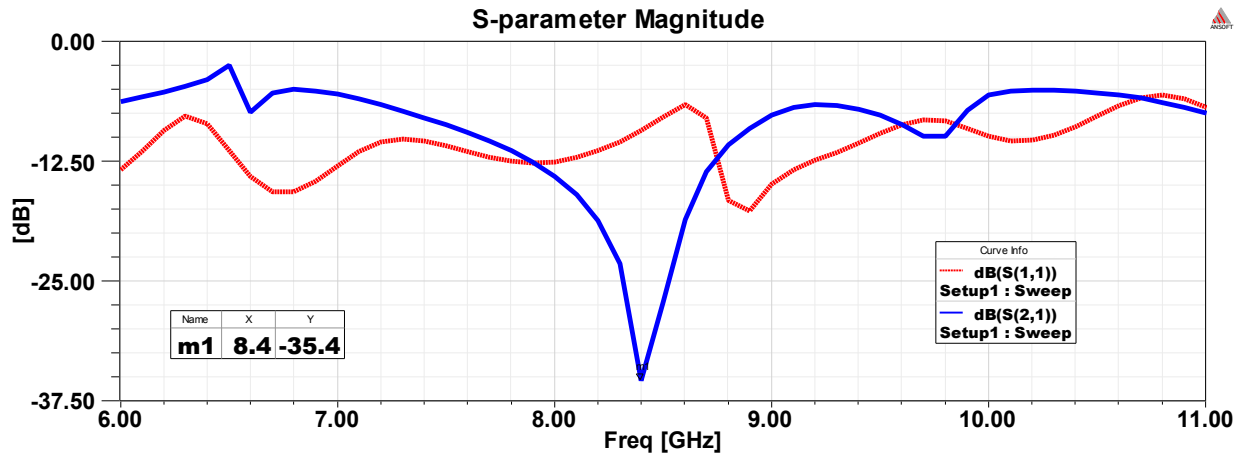

Figure 3.27: S-parameter Magnitude for Thick Random Block of CLLs w/o Periodic Boundary Conditions

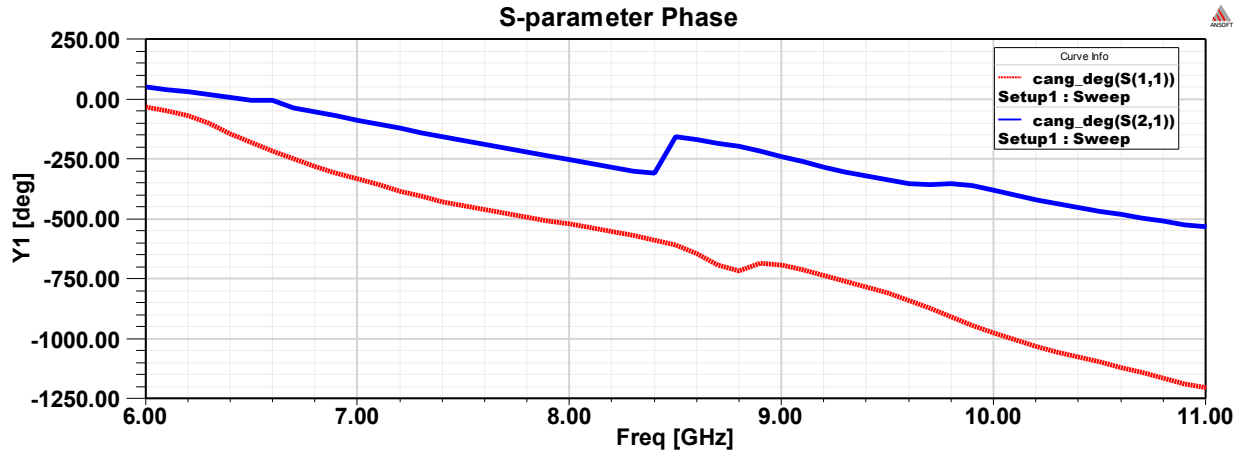

Figure 3.28: S-parameter Phase for Thick Random Block of CLLs w/o Periodic Boundary Conditions

3.6 Conclusion

Results presented in this chapter have not been able to successfully demonstrate a random metamaterial structure having a negative index of refraction. However, the other interesting resonant properties have been observed. Random metamaterial structures could potentially be used as RF wave filters or frequency selective surfaces (FSS) for specific frequency-dependent applications. Currently, simulating metamaterials filled with random or aperiodic inclusions has proven to be very difficult and forces many restrictions and limitations. Greater computational power or more sophisticated full-wave simulation software will be needed to analyze random metamaterial structures in even greater detail. We cannot say with certainty that random metamaterial structures do not produce negative parameters. More work needs to be done to improve the simulation and parameter extraction methods to obtain a greater level of certainty. However, this study of random metamaterial has produced interesting results that can be further studied in future works. Currently, no other published works are known to have performed full-wave simulations on metamaterials that are random in both position and orientation.

Chapter 4: CLL-Loaded Dipole Structure to Enhance Antenna Performance

4.1 Introduction

This chapter introduces an innovative antenna enhancing structure consisting of capacitively-loaded loop (CLL) metamaterial elements placed radially around a standard dipole antenna at an electrically small distance. As a result of this innovative arrangement, the dipole antenna is easily transformed into a directive mechanically scanned antenna with high realized gain. The desired directivity and gain can be tuned based on the number of radial CLL fins placed around the dipole. Interactions between the antenna and metamaterial elements result in significant enhancement of the maximum radiated field amplitude and front-to-back ratio. The structures presented are modeled using full-wave simulation, and one is experimentally verified as a proof-of-concept.

An area of particular focus of metamaterial application is to realize artificial magnetic conductors (AMCs) for a variety of antenna applications. An AMC is generally characterized by having a high impedance and high permeability [46]. An ideal AMC, also known as a perfect magnetic conductor (PMC), is a surface that exhibits a reflectivity of $\Gamma = +1$, as opposed to a PEC, which has a reflectivity of $\Gamma = -1$ [7]. The AMC surface can be engineered to produce near zero phase reflection, resulting in constructive interference of transmitted and reflected waves, regardless of distance to the antenna aperture [47, 30]. A slab exhibiting large intrinsic impedance will act as a broad bandwidth in-phase reflector, i.e., as an AMC [46], which is useful as an antenna backplane for low-profile antenna designs. While many studies have focused on using metamaterials to create planar AMC backplanes, few studies have focused on arranging elements around the antenna.

In this chapter, a realistic planar dipole antenna will be combined with CLL metamaterial structures in various configurations to enhance the performance of the conventional dipole antenna. Each CLL is of the same shape and size of those used in previous sections of this thesis.

Modeling and analysis of these integrated CLL-based dipole antenna structures were simulated using ANSYS High-Frequency Structure Simulator version 14.0 (HFSS v14.0). This study investigated how the printed dipole antenna could be strategically combined successfully with CLL fins to enhance antenna gain and directivity.

4.2 CLL Structure Design

The unit capacitively-loaded loop (CLL) element used in this study is similar to that presented by Erentok *et al.* [46] and has been scaled to resonate at 12.5GHz. The external dimensions of each unit CLL are *2.5mm* x *5.0mm*. This CLL design has been demonstrated in simulation to exhibit negative refraction (simultaneous $\varepsilon < 0$ and $\mu < 0$) when coupled with a metal probe.

This study demonstrates that a metamaterial structure consisting of CLL loops can be placed radially around a standard dipole antenna to make it directive in the H-plane, and significantly increases its realized maximum gain. The structure consists of pairs of radial fins around the dipole, in which each fin is a rectangular array of individual CLL elements. The distance between the dipole and the nearest edge of the CLL fin is r=1.66mm, which is ~0.08λ at f=20GHz, the approximate frequency of max realized gain.

Each radial fin consists of nine CLL elements in a 3 x 3 array. The two radial fins in each pair are oriented in the same direction, such that the dipole faces the open end of the CLLs in one direction and the closed end in the other direction. The most simple structure, as shown in Fig. 1a, consists of a planar dipole antenna on a dielectric plane with one pair of CLL fins, as described above, placed on either side of the dipole in the same plane. To further enhance the effects of the CLLs on the dipole antenna, the dielectric plane is removed, and greater multiples of radial CLL fin pairs are symmetrically placed around the axis of the dipole as shown later in this chapter in Figure 4.1.

4.3 Previous Work on AMC Block as Electrically Close Antenna Backplane

Previous work has shown that the same CLL metamaterial loops used to demonstrate negative refraction earlier in this thesis can also be used to create an AMC surface can be utilized as an electrically close antenna backplane [46]. Conventional metallic backplanes will cause

destructive interference if a dipole antenna, horizontally oriented with respect to surface, is placed less than λ/2 from the metallic backplane. However, just as studies have shown that utilize electromagnetic band-gap (EBG) surfaces to provide zero-phase reflection [29, 47, 30, 48], the AMC backplane can be placed electrically close ($d << \lambda/2$) to the dipole antenna and still provide constructive interfere. A good antenna backplane is measured by the maximum realized gain in the direction of intended propagation as well as the front-to-back ratio of the main beam. This work intends to improve on the performance of previous results and also utilize the CLLs in additional manners to enhance the performance of a standard dipole antenna by loading it with CLLs similar to that as done by Erentok and Ziolkowski [46, 9], shown in Figure 4.1.

In addition, Erentok and Ziolkowski state that the two-CLL-deep based metamaterial block, shown in Figure 4.2, acts as an artificial magnetic conductor (AMC) when the plane wave is incident upon the open-ended capacitive gaps of the loops[46, 9].

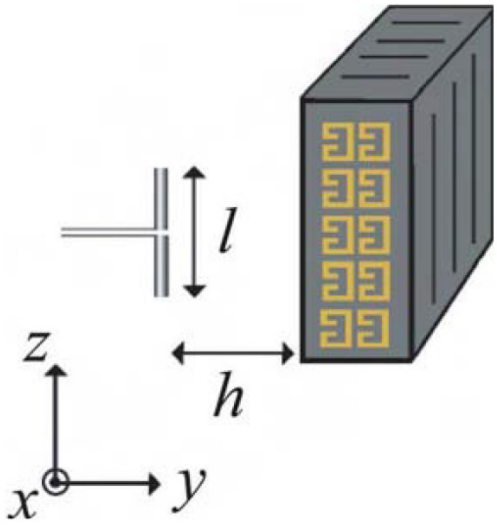

Figure 4.1: AMC Block as Electrically Close Antenna Backplane [9, 46]
(Used by permission of Wiley, publ.)

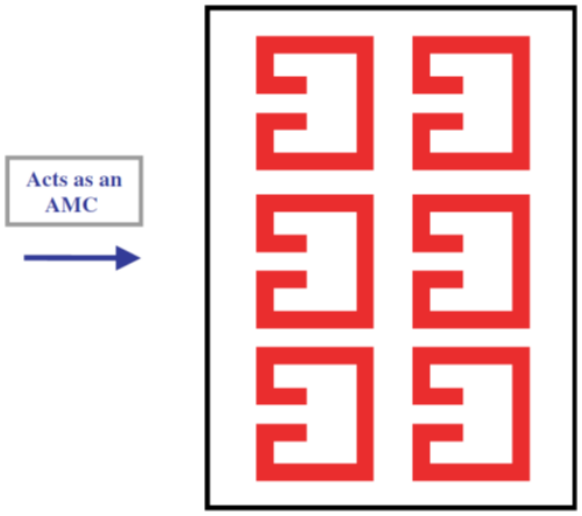

Figure 4.2: CLLs Acting as AMC Surface [9]
(Used by permission of Wiley, publ.)

4.4 Characterization of CLL Block

4.4.1 Propagating Towards Open Ends of Loops

Simulation in this chapter will begin by characterizing the performance of the CLL surface as presented by Erentok [46] using the PEC/PMC infinite array simulation. This takes the array of six CLLs, as shown below, and arrays it infinitely in the horizontal and vertical directions, shown in Figure 4.3. This infinite array is an effective medium from which we will extract the constitutive parameters.

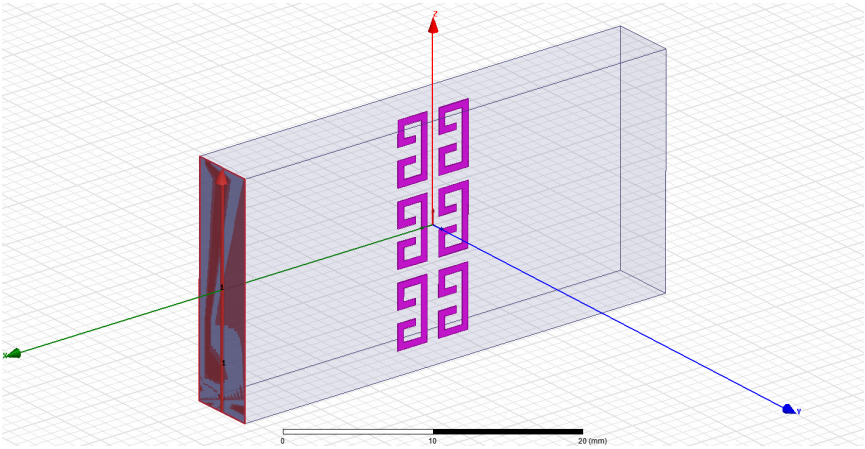

Figure 4.3: Open-ended CLL Block Simulated in HFSS

The S-parameters from the CLL surface, shown in Figure 4.4 and Figure 4.5, exhibit a reflective resonant region between approximately 10.2GHz and 16.0GHz. Outside of this band, the metallic surface consisting of CLLs is highly transmitting. This sort of AMC surface could be potentially used as a frequency band reject metasurface.

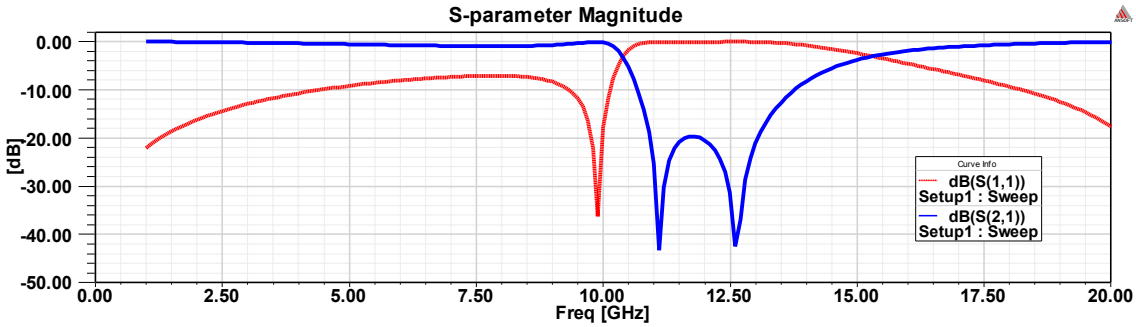

Figure 4.4: S-parameter Magnitude of Open-ended CLL Block Simulated in HFSS

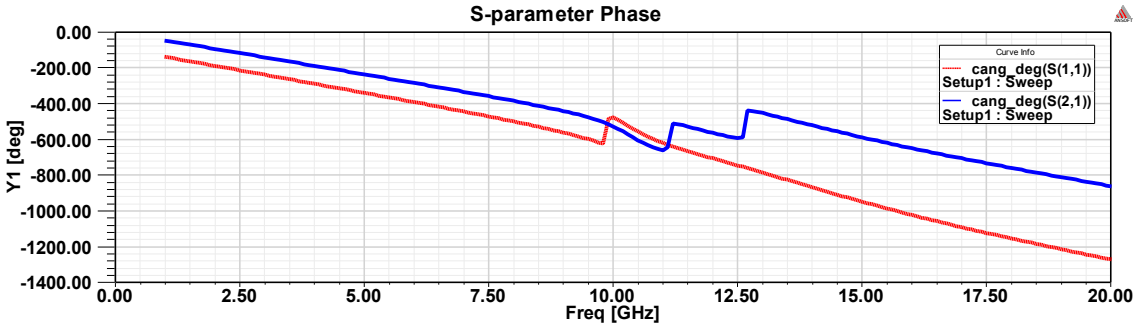

Figure 4.5: S-parameter Phase of Open-ended CLL Block Simulated in HFSS

Analyzing the constitutive parameters for this CLL metasurface, shown in Figure 4.6, the behavior is exotic with the highly reflective resonant range from approximately 10GHz to

14GHz. Within this region, the impedance is near zero, ε is negative, μ is highly positive, and refractive index, *n*, is also elevated.

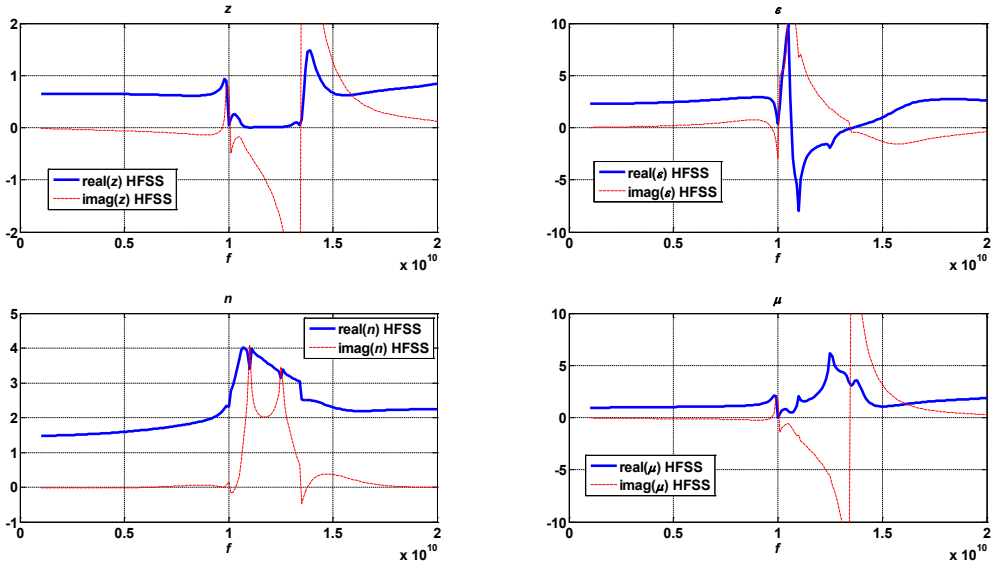

Figure 4.6: Constitutive Parameters for Open-ended CLL Block Simulated in HFSS

4.4.2 Propagating Towards Closed Ends of Loops

The CLL metasurface is also analyzed when propagating from the opposite direction for purposes of characterization as shown in Figure 4.7.

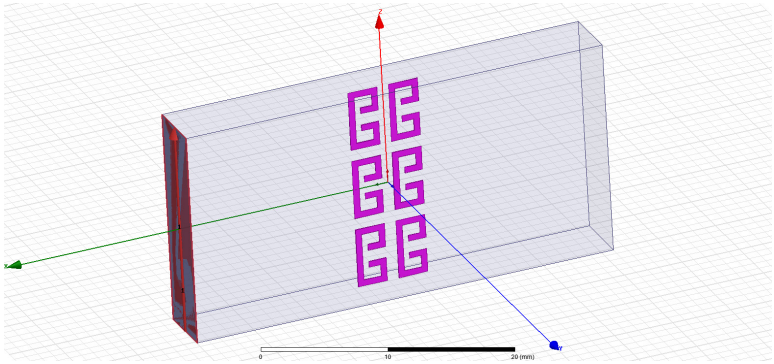

Figure 4.7: Closed-ended CLL Block Simulated in HFSS

The S-parameters for this structure, shown in Figure 4.8 and Figure 4.9, appear very similar to the previous structure; however, the constitutive parameters, shown in Figure 4.10, are a bit different. Within the resonant region, there are both negative ε and μ Lorentz responses;

however, these two negative regions are in different frequency bands, such that refractive index is always positive and $n>1$.

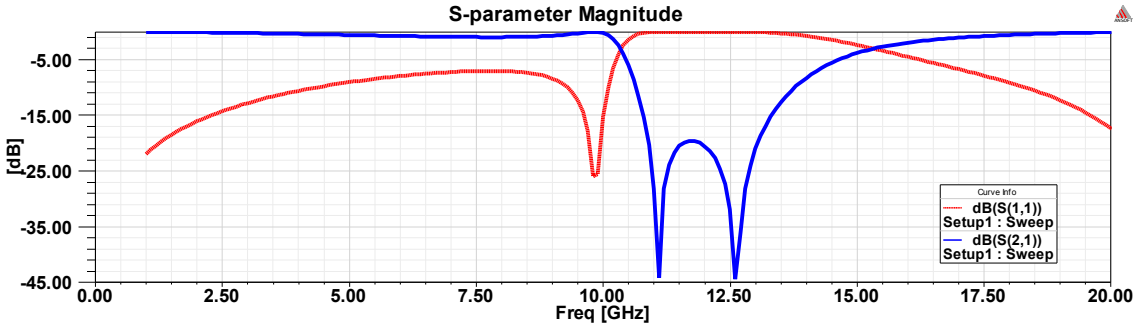

Figure 4.8: S-parameters Magnitude for Closed-ended CLL Block Simulated in HFSS

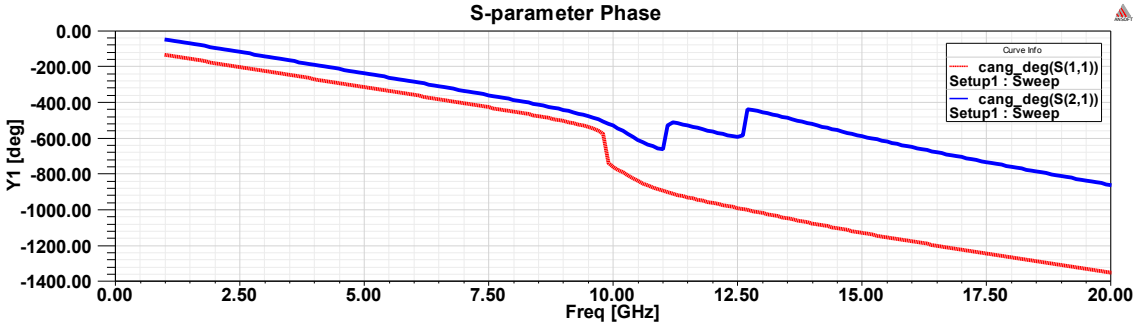

Figure 4.9: S-parameters Phase for Closed-ended CLL Block Simulated in HFSS

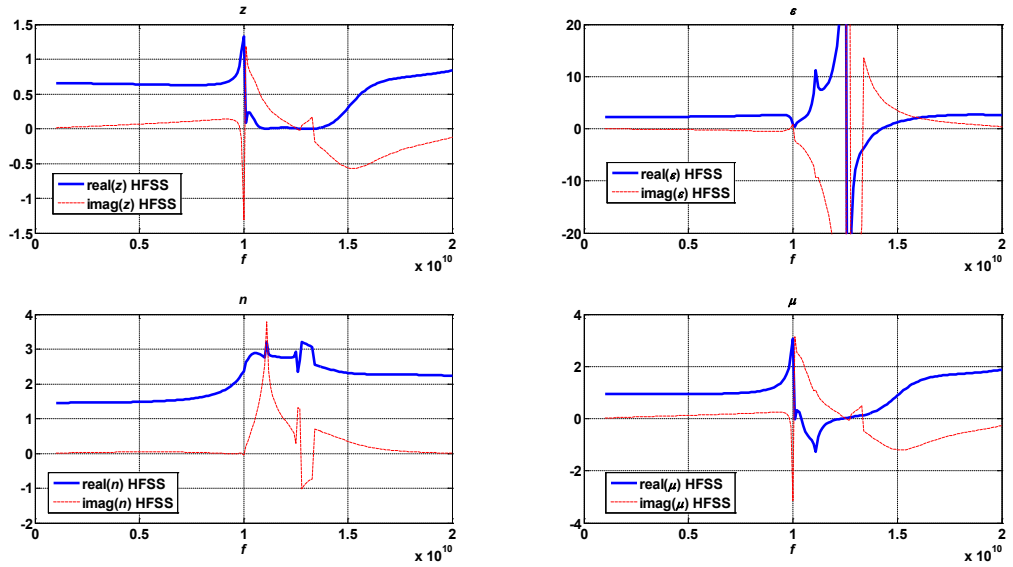

Figure 4.10: Constitutive Parameters for Closed-ended CLL Block Simulated in HFSS

4.5 Planar Dipoles in Free Space

For purposes of comparison to antennas presented later in this chapter, a 9-mm planar dipole in free space is simulated using HFSS, shown in Figure 4.11. The return loss of this antenna shows resonance at 15.4GHz, as shown in Figure 4.12. The maximum realized gain of this planar dipole, shown in Figure 4.13, is simulated to be 2.2dB as expected. In addition, the 11mm planar dipole, which is not shown, also has a simulated maximum realized gain of 2.2dB.

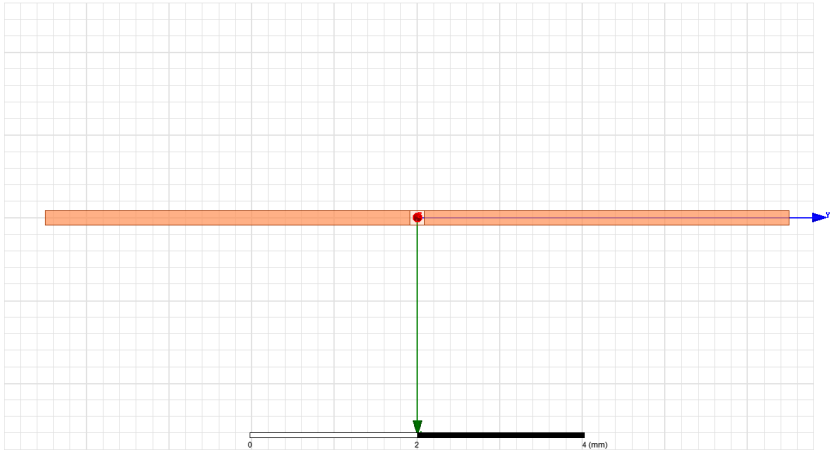

Figure 4.11: 9mm Planar Dipole in Vacuum

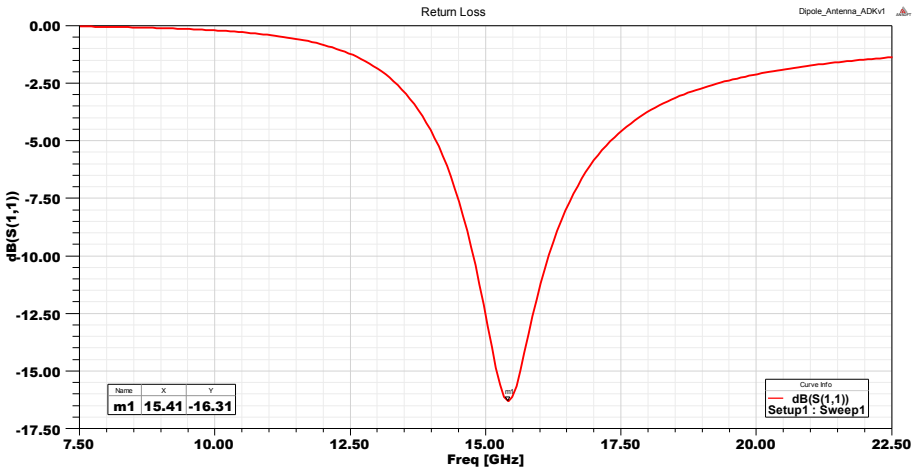

Figure 4.12: S_{11} for 9mm Planar Dipole in Vacuum

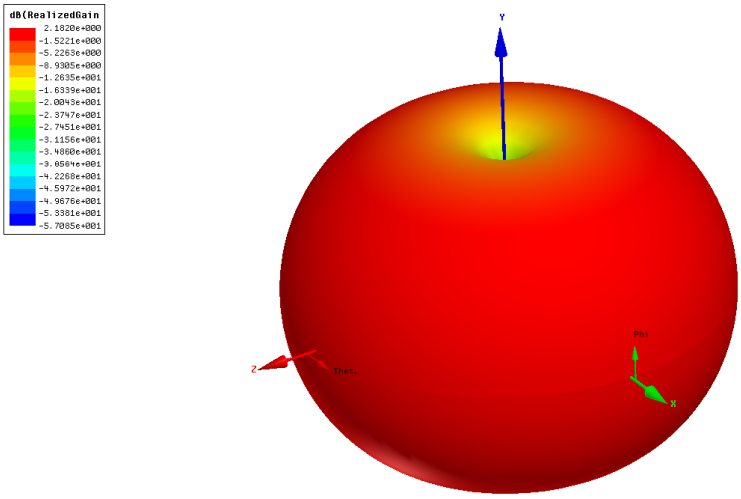

Figure 4.13: 3-D Realized Gain Pattern for 9mm Planar Dipole; Max Realized Gain: 2.2dB

4.6 Random CLLs Placed Around Dipole

To continue the theme of random CLL analysis, a radiating dipole antenna was placed in the center of a block consisting of randomly positioned and oriented CLLs, shown in Figure 4.14. This structure was simulated in HFSS to see what effect the random CLLs have on the radiating performance of the dipole antenna. CLLs at the center of the block are removed to prevent intersection with the dipole antenna. The resonance of the planar dipole antenna is 15GHz in free space.

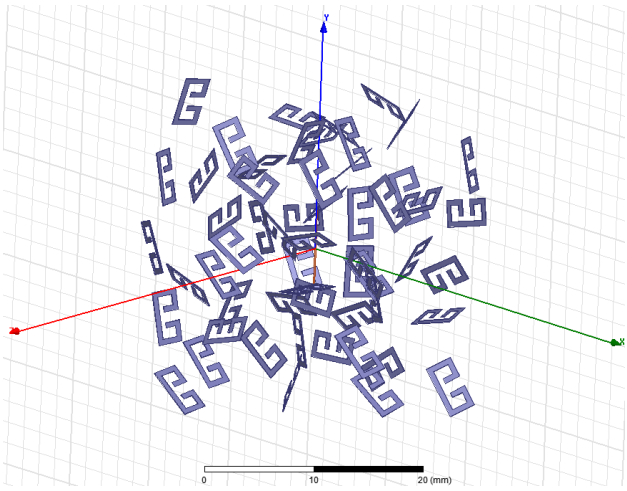

Figure 4.14: Randomly Positioned and Oriented CLLs Placed Around a Dipole Antenna

While not having a theorized application, the results of placing a dipole antenna in the center of a random block of CLLs is interesting. By placing the randomly oriented and positioned CLLs

around the planar dipole antenna, the resonance of the antenna increased from 15GHz to 18.6GHz, an increase of 3.6GHz or 24% in the resonant frequency, shown in Figure 4.15. As might have been expected from a random configuration, the normal clean donut-shaped radiation pattern of a typical dipole antenna has random fluctuations in the radiation pattern. The maximum gain of this antenna is 4.2dB, as shown in Figure 4.16, an enhancement of approximately 2dB of the maximum gain of the standard dipole. If an experiment needed a signal transmitted or received with random fluctuations in the pattern based on direction, this would be a useful structure.

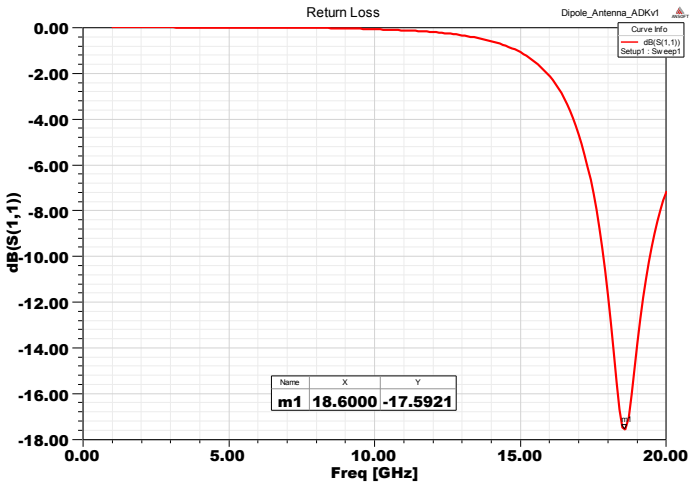

Figure 4.15: S_{11} Return Loss for Randomly Positioned and Oriented CLLs Placed Around a Dipole Antenna

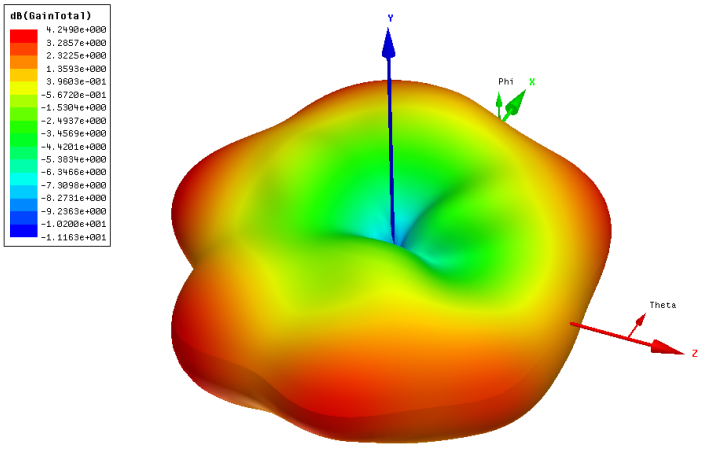

Figure 4.16: Gain Pattern for Randomly Positioned and Oriented CLLs Placed Around a Dipole Antenna

4.7 Dipole Antenna Loaded w/ Single CLL Fin Resulting in AMC-Like Performance

To resonate at a similar frequency to the CLL loops, the length of the planar dipole antenna was increased to by 11mm, shown in Figure 4.17. The resonant frequency of the 11mm planar dipole antenna alone in free space was simulated in HFSS to be f_0=12.6GHz with S_{11} return loss of -16.6dB, shown in Figure 4.18.

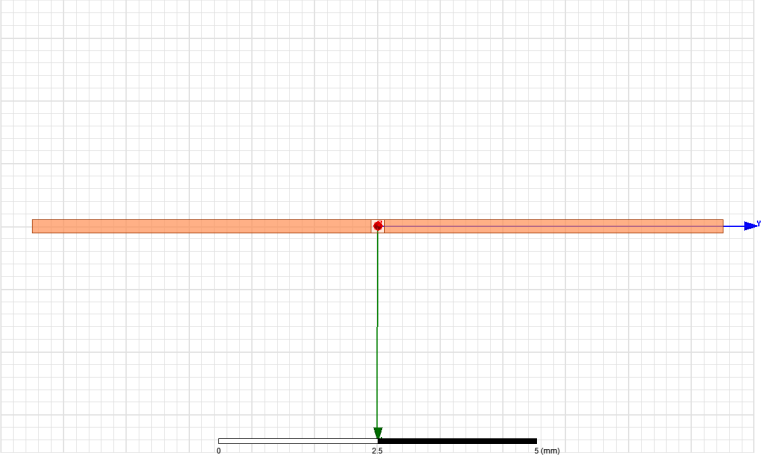

Figure 4.17: 11mm Planar Dipole in Free Space

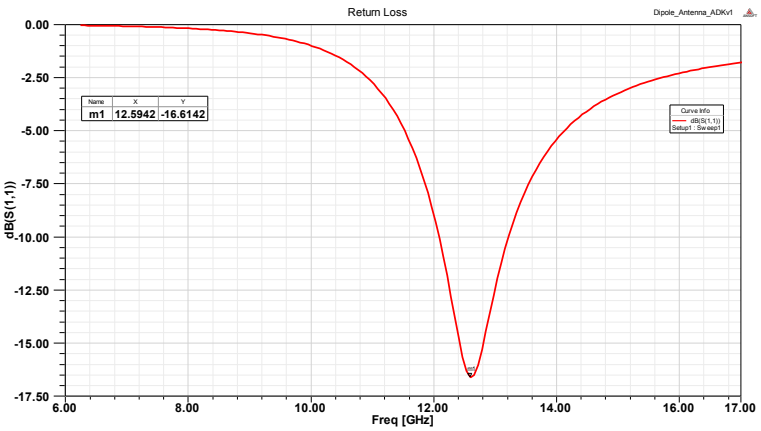

Figure 4.18: S_{11} Return Loss for 11mm Planar Dipole in Free Space

While the similar AMC structure presented by Erentok used a volumetric block of many CLLs [46], the result of the antenna presented in this section is able to demonstrate strong antenna performance as measured by realized main and front-to-back ratio while only using six thin planar CLLs, shown in Figure 4.19. This result makes the antenna much more low-profile as

it only needs a fin consisting of six CLLs rather than an entire backplane. The return loss of this antenna is shown in Figure 4.20. The maximum realized gain, shown in Figure 4.21, of this antenna is 6.1dB, resulting in a significant improvement.

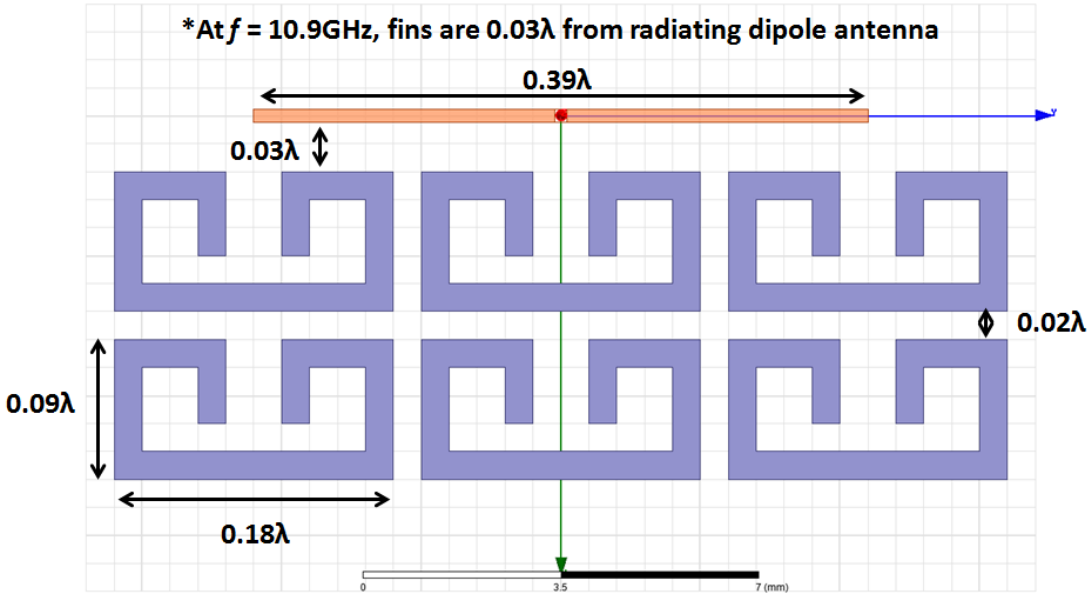

Figure 4.19: Single Open-Ended CLL Fin Placed Electrically Close to 11mm Planar Dipole

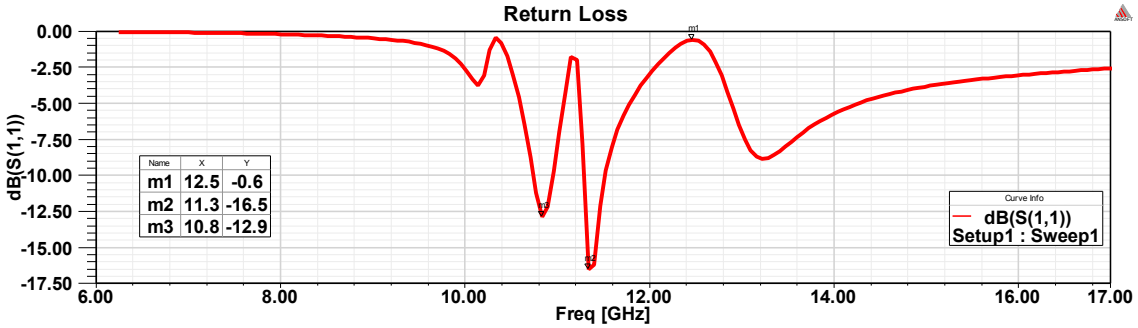

Figure 4.20: S_{11} Return Loss for Single Open-Ended CLL Fin Placed Electrically Close to 11mm Planar Dipole

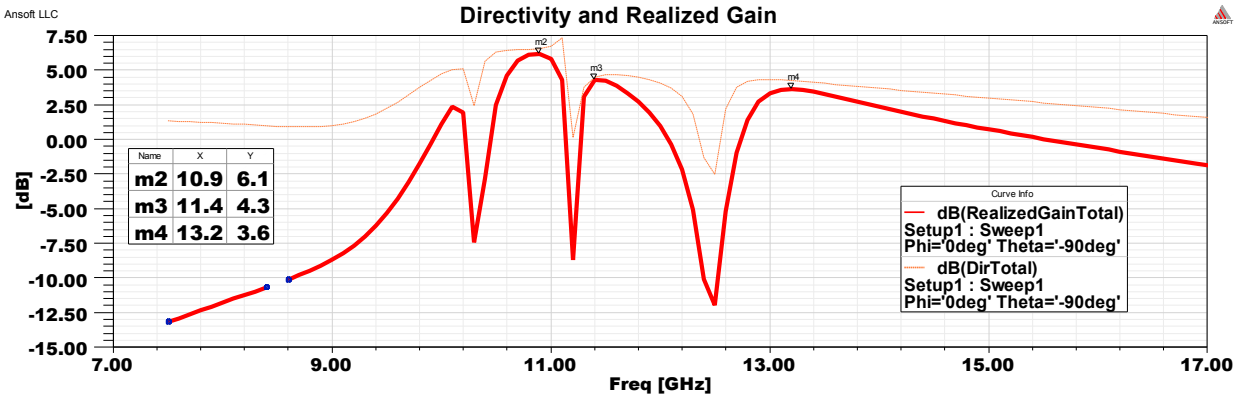

Figure 4.21: Directivity and Realized Gain vs. Frequency for Single Open-Ended CLL Fin Placed Electrically Close to 11mm Planar Dipole

The S_{11} phase reflection at the dipole antenna, shown in Figure 4.19, is calculated and shown in Figure 4.22. The phase reflection calculation is a similar calculation as done for analysis of EBG structures. Generally, phase reflections below 90° are considered improvements because they provide constructive interference with the transmitting source [30, 46].

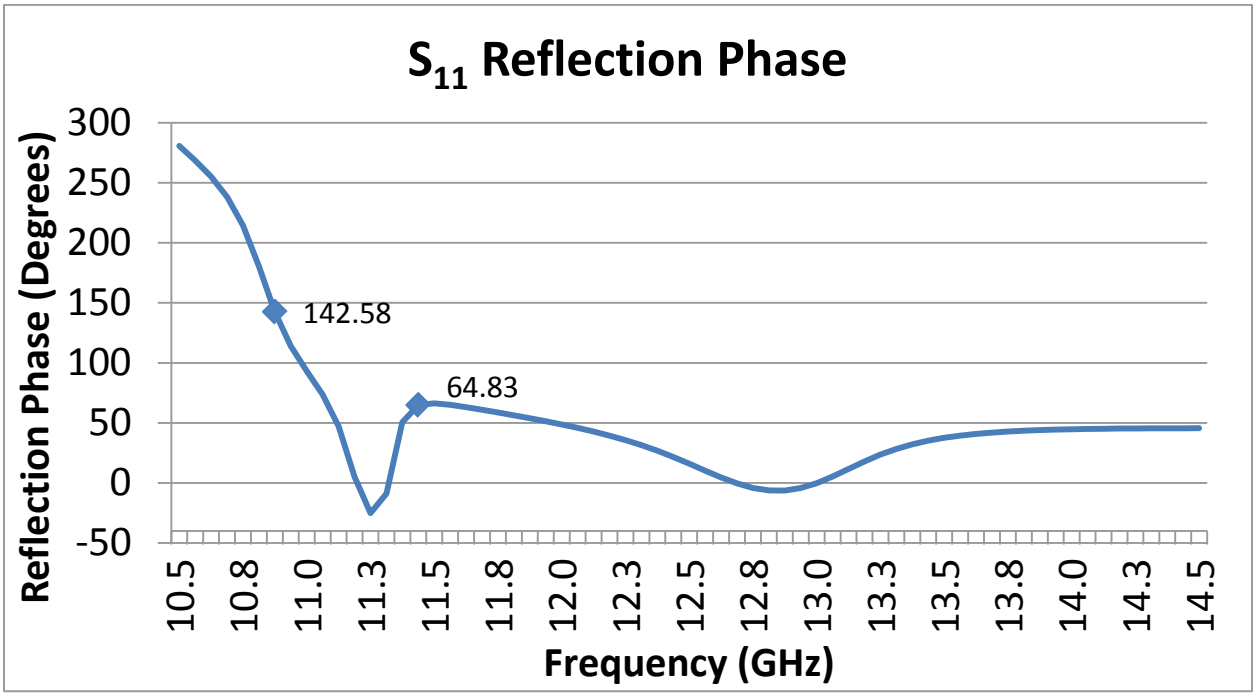

Figure 4.22: S11 Reflection Phase at the Dipole for Single Open-Ended CLL Fin Placed Electrically Close to 11mm Planar Dipole

The 3-D gain pattern for this antenna is shown in Figure 4.23. Notice that nearly all of the power is reflected to one side, similar to the case of having a continuous backplane.

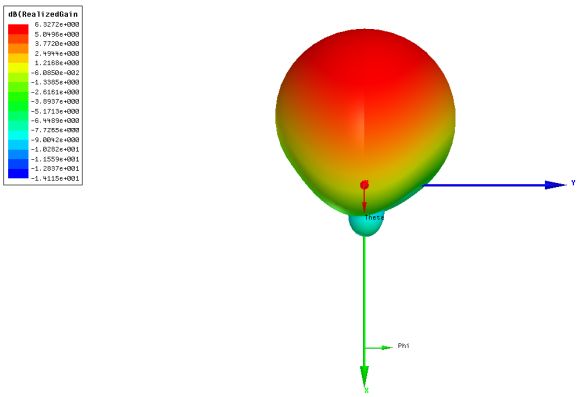

Figure 4.23: Realized Gain vs. Frequency for Single Open-Ended CLL Fin Placed Electrically Close to 11mm Planar Dipole; Max Realized Gain: 6.3dB at 10.9GHz

4.8 Dipole Loaded CLLs Operating Above Resonant Frequency of Loops

An innovative realization in this thesis is that a structure consisting of CLL loops can be placed radially around a standard dipole antenna to make it directive in the H-plane, significantly increasing its realized maximum gain. The structure consists of pairs of radial fins around the dipole, in which each fin is a rectangular array of individual CLL elements. The distance between the dipole and the nearest edge of the CLL fin is $r=1.66mm$, which is $\sim 0.08\lambda$ at $f=20GHz$, the approximate frequency of max realized gain.

Each radial fin consists of nine CLL elements in a three-by-three array. The two radial fins in each pair are oriented in the same direction, such that the dipole faces the open end of the CLLs in one direction and the closed end in the other direction. The simplest structure, shown in Figure 2.24, consists of a planar dipole antenna on a dielectric plane with one pair of CLL fins, as described above, placed on either side of the dipole in the same plane. To further enhance the effects of the CLLs on the dipole antenna, the dielectric plane is removed, and greater multiples of radial CLL fin pairs are symmetrically placed around the axis of the dipole as shown later in the chapter in Figure 4.35.

Using HFSS, it was verified that both the forward and backward facing fins must be present to achieve the maximum enhancing effects. Neither the open-end or closed-end fins, with respect to the dipole, produce the desired enhancements alone. In addition, when all fins are either in the

open-end or closed-end orientation, with respect to the dipole, the effects of each fin cancel each other out, producing no effective enhancement.

4.8.1 Planar CLL-Loaded Dipole Antenna

The first multi-fin CLL structure analyzed is the planar antenna structure with CLL two fins surrounding dipole antenna, shown in Figure 4.24. The adaptive mesh used for full-wave simulation of this structure in HFSS is shown in Figure 4.25 and Figure 4.26. The S_{11} return loss of this two-fin planar CLL-loaded dipole antenna shows a resonance of -19.2dB at 19.3GHz, shown in Figure 4.27. The resonance of the CLL loops is much weaker with strength of -2.8dB at 12.4GHz. The 3-D realized gain pattern at the resonant frequency of 19.3GHz showed a maximum realized gain of 4.4 dB, shown in Figure 4.28. This gain pattern shows distinct main lobes, both pointing into a single hemisphere, with a realized gain of 4.4 dB. To improve the performance of this loaded antenna structure, it would be desirable to squeeze the two separate main lobes into a single directive high-gain lobe.

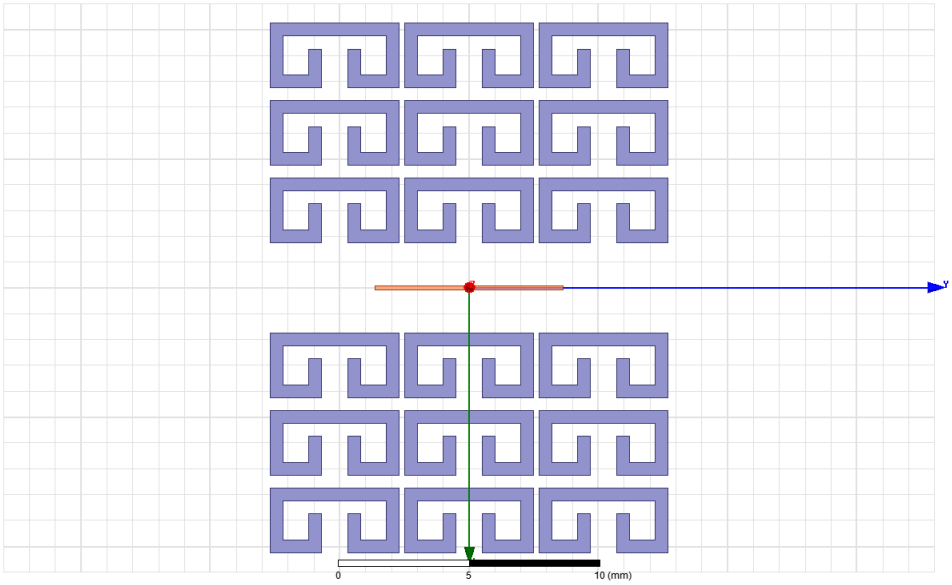

Figure 4.24: Planar Antenna Structure w/ CLL Fins Surrounding Dipole Antenna

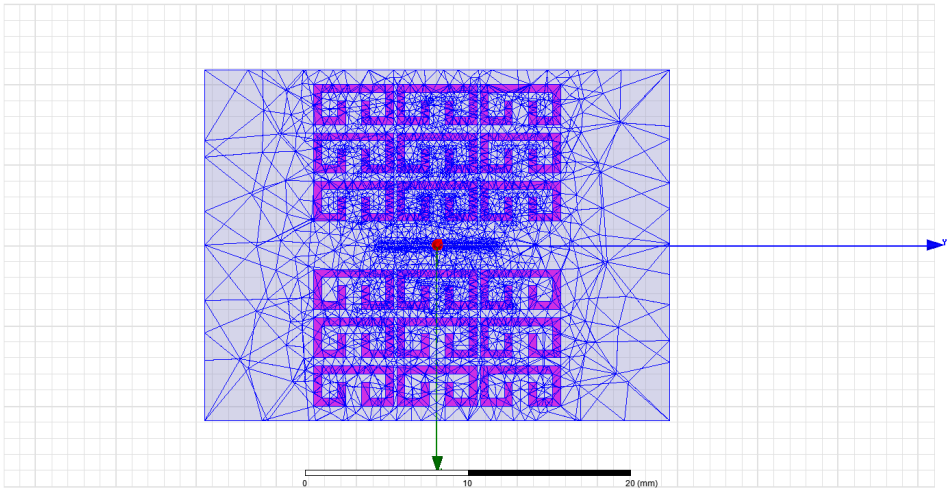

Figure 4.25: HFSS Adaptive Meshing of Planar Antenna Structure w/ CLL Fins Surrounding Dipole Antenna

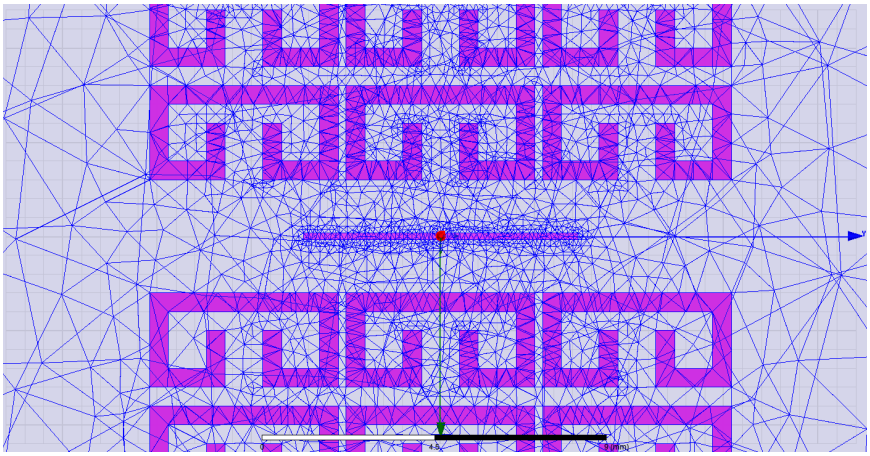

Figure 4.26: HFSS Adaptive Meshing of Planar Antenna Structure w/ CLL Fins Surrounding Dipole Antenna (Zoomed-In on Dipole)

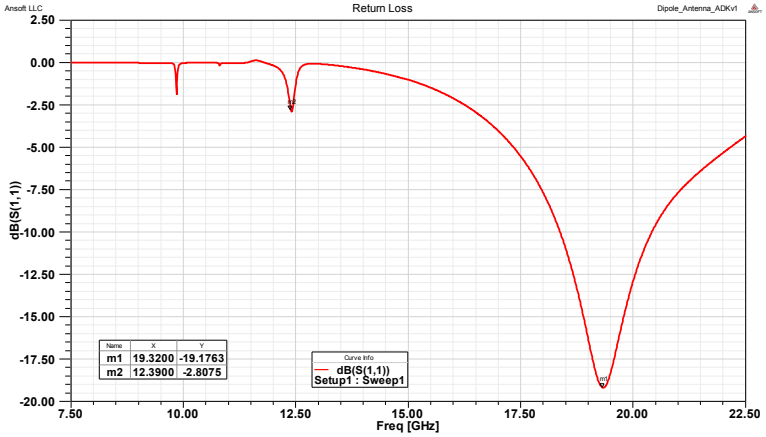

Figure 4.27: S_{11} Return Loss of Planar CLL-Loaded Dipole Antenna

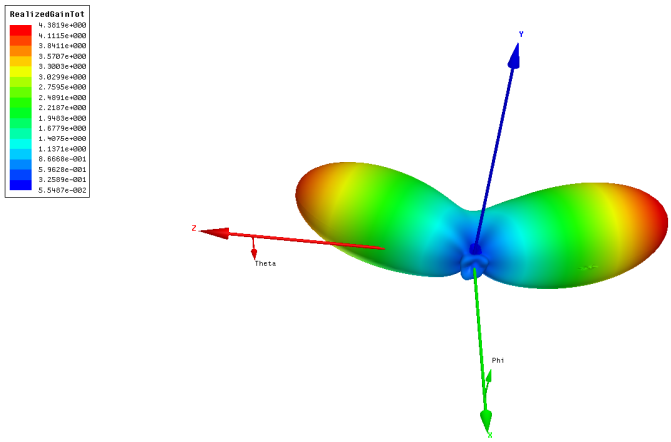

Figure 4.28: 3-D Realized Gain Pattern; Max Realized Gain: 4.4 dB

Table 1 summarizes the gain of CLL-loaded dipole antenna based on fin orientation. The fin combination that provides the greatest gain enhancement for a two-fin planar structure has one fin oriented with the open ends of the loops facing the dipole, and the opposite fin has the closed ends of the loops facing the dipole, shown in Figure 4.24. In this case, the open-ended fin acts as a director and the closed-end fin acts as a reflector. Intuitively, the reflector-reflector and director-director combinations each provide symmetry that results in a destructive effect that reduces gain enhancement compared to the director-reflector (open-end and closed-end orientation) combination.

Table 2 summarizes an analysis of fin dimension on the CLL-loaded dipole antenna performance. The data shows that increasing the number of director and reflector fins increases the maximum gain of the antenna. However, adding additional directors and reflectors comes at a cost of linearly increasing the size of the antenna apertures, which may be a significant issue for low-profile antennas.

Characterization of Planar Fins

Resonant Frequency	Fin 1 Orientation (Facing Antenna)	Fin 2 Orientation (Facing Antenna)	Maximum Gain (dB)	S11 Return Loss (dB)
19.3 GHz	Open	Closed	6.5	-19.2
16.5 GHz	Open	Open	2.7	-15.7
15.5 GHz	Closed	Closed	4.0	-7.6

Table 1: Gain of CLL-Loaded Dipole Antenna Based on Fin Orientation

As CLL Fin Spacing ↓, Maximum Antenna Gain ↑

Resonant Frequency	# Horizontal CLLs	# Vertical CLLs	Max Gain (dB)	S11 Return Loss (dB)
15.5GHz	3	3	5.8dB	-30.2dB
14.7 GHz	2	3	4.4 dB	-28.0 dB
15.6 GHz	5	3	6.3 dB	-28.5 dB
15.6 GHz	2	5	4.1 dB	-33.3 dB
15.5 GHz	1	3	4.0 dB	-27.1 dB

Table 2: Analysis of Fin Dimension on Antenna Performance

As # of Horizontal Fins ↑, Maximum Antenna Gain ↑

4.8.2 Four Radial CLL Fins Surrounding Dipole Antenna

In an attempt to further enhance the gain, additional CLL loading fins were added around the dipole antenna, shown in Figure 4.29. With only two fins, the antenna resulted in two main beams, as was shown in Figure 4.28. The goal is to add additional fins to push the two major lobes into a single highly directive main lobe. In the 4-fin structure, shown in Figure 4.29, the reflector and director fins are each copied and the copied fins rotated 90^{o} degrees around the radial (vertical) axis. This configuration results in two directors and two reflectors. The S_{11} return loss for 4-fin CLL-loaded dipole antenna indicates a resonance of -15.7dB at 19.8GHz, shown in Figure 4.30. Note that the resonant frequency of the CLL-loaded dipole antenna has increased with addition of more CLL fins. The 3-D realized gain pattern for 4-fin CLL-loaded dipole antenna indicates a maximum realized gain of 7.8dB at 19.8GHz, shown in Figure 4.31.

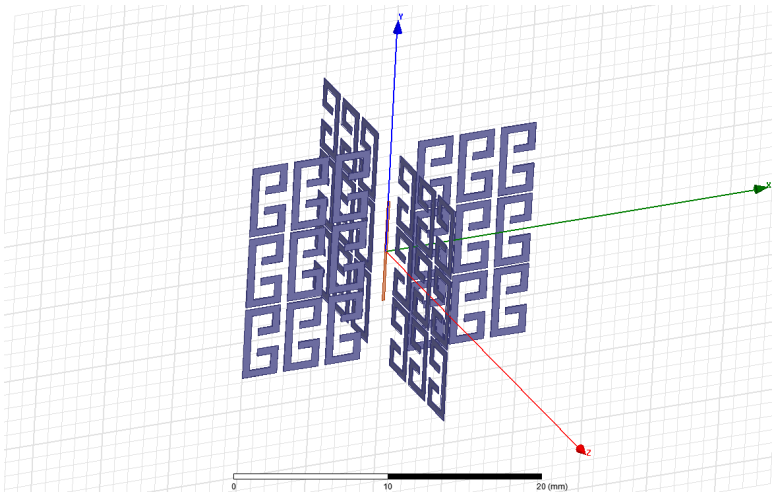

Figure 4.29: 4-fin CLL-Loaded Dipole Antenna

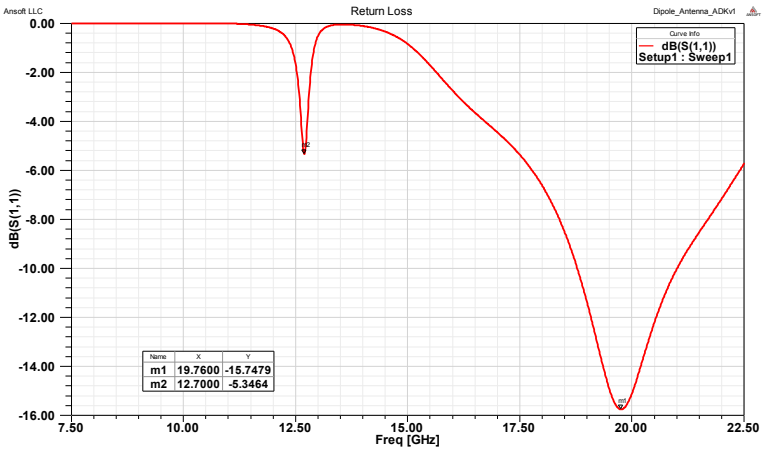

Figure 4.30: S_{11} Return Loss for 4-fin CLL-Loaded Dipole Antenna

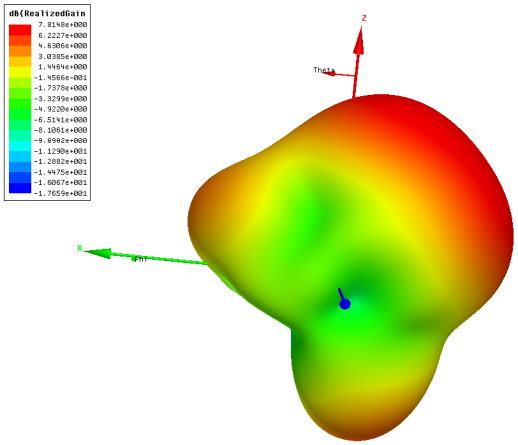

Figure 4.31: Realized Gain Pattern for 4-fin CLL-Loaded Dipole Antenna; Max Realized Gain is 7.8dB at 19.8GHz

4.8.3 Eight Radial CLL Fins Surrounding Dipole Antenna

With the success of increasing maximum realized gain by increasing the number of radial CLL fins from two to four, the next logical step is to place eight evenly spaced radial CLL fins surrounding the dipole antenna, shown in Figure 4.32. This loaded antenna has four director fins in one hemisphere and four reflectors on the opposite side of the dipole in the other hemisphere. Increasing the number of radial CLL fins continues to increase the resonant frequency of the loaded antenna. The S11 return loss for eight fin CLL-loaded dipole antenna is -32.5dB at the resonant frequency of 20.8GHz, shown in Figure 4.33. The 3-D realized gain pattern for this structure, shown in Figure 4.34, indicates a maximum realized gain of 6.0dB at 20.8GHz. While the realized gain of the eight CLL fin structure is real than that of the four fin structure, the eight fin structure has a higher directivity, indicating that this structure could be better impedance matched. However, the radiation pattern shows a much more directive antenna beam, which is one of the desired goals.

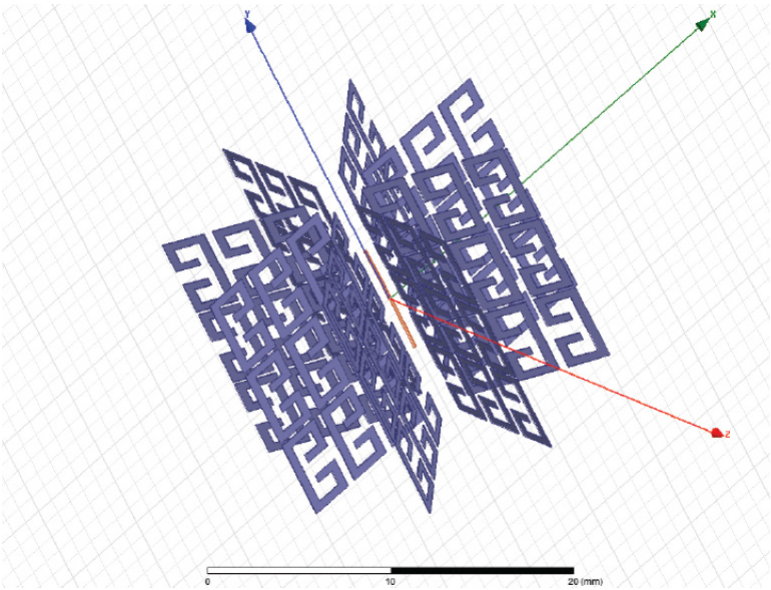

Figure 4.32: 8-fin CLL-Loaded Dipole Antenna

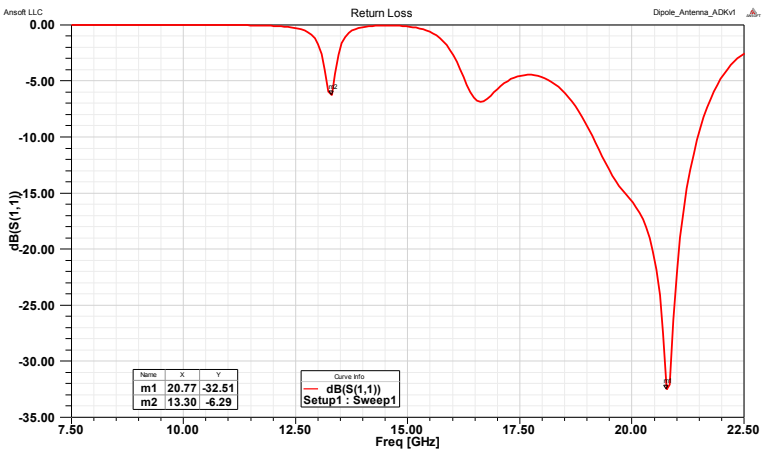

Figure 4.33: S_{11} Return Loss for 8-fin CLL-Loaded Dipole Antenna

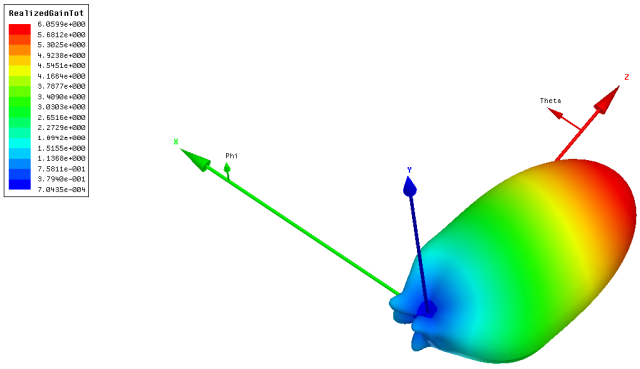

Figure 4.34: Realized Gain Pattern for 8-fin CLL-Loaded Dipole Antenna; Max Realized Gain is 6.0dB at 20.8GHz

4.8.4 Twelve Radial CLL Fins Surrounding Dipole Antenna

Similar to the structure with eight radial CLL fins, this structure has twelve radial CLL fins surrounding the dipole antenna, shown in Figure 4.35, with the objective of further increasing directivity and maximum realized gain of the main beam. Again, the S_{11} return loss for twelve fin CLL-loaded dipole antenna, shown in Figure 4.36, indicates an elevated resonance compared to the standard dipole antenna. While multiple resonances exist for this antenna, the strongest resonance is -16.1dB at 20.5GHz. The 3-D realized gain pattern for twelve fin CLL-loaded dipole antenna indicates a maximum realized gain of 9.0dB at 20.5GHz, shown in Figure 4.37.

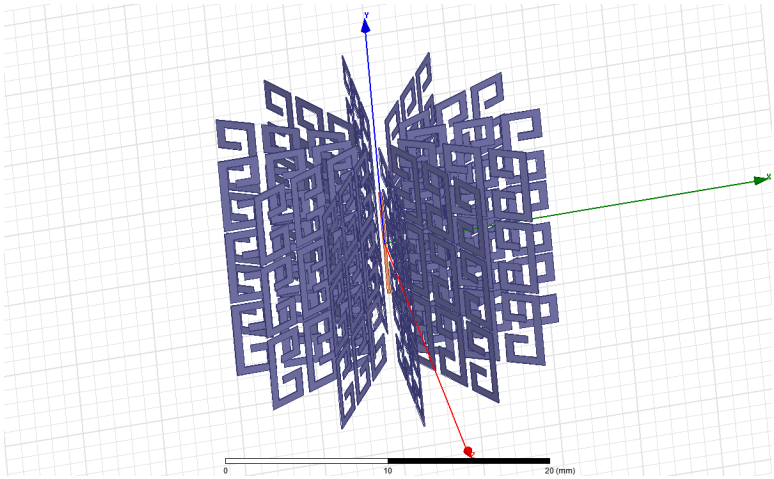

Figure 4.35: 12-fin CLL-Loaded Dipole Antenna

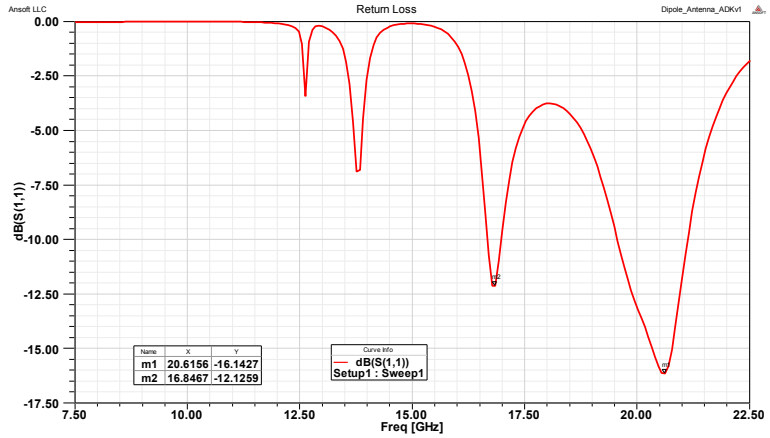

Figure 4.36: S_{11} Return Loss for 12-fin CLL-Loaded Dipole Antenna

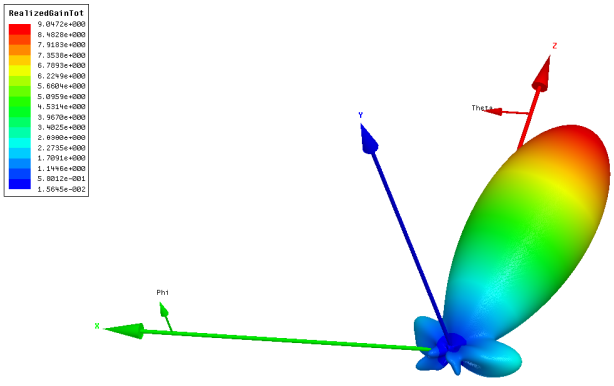

Figure 4.37: Realized Gain Pattern for 12-fin CLL-Loaded Dipole Antenna; Max Realized Gain is 9.0dB at 20.5GHz

Table 3 below summarizes the antenna performance of the radial CLL-loaded fin structures presented in this chapter so far. Notice that as the number of CLL fins increases, the maximum gain and realized gain of the antenna tend to also increase. Additionally, directivity of the main beam continues to increase as the number of CLL fins increases.

# of CLL Fins	Max Gain (dB)	Gain Improvement (dB)	Realized Gain (dB)	3-dB BW (deg)	Frequency of Max Gain (GHz)	Front-to-Back Ratio (dB)
0	2.2	0	2.2	n/a	15.3	0
2	5.4	3.2	4.4	165.1^{o}	19.3	9.3
4	6.9	4.7	6.8	95.7^{o}	19.7	3.2
8	7.8	5.7	6.0	88.9^{o}	20.8	10.7
12	9.7	7.5	9.0	48.3^{o}	20.5	12.4

Table 3: HFSS Simulation Results for Structures Based on # of CLL Fins

As # of CLL Fins ↑, Maximum Antenna Gain ↑

4.9 Improved Design: Continuous Fin Loaded Dipole Antenna

Simulation results indicated that maximum realized gain of the CLL-loaded dipole structure tends to improve as the spacing between the adjacent fins was decreased. Taking this concept to the extreme, a hybrid antenna design was simulated, as depicted in Figure 4.38, where adjacent CLLs were intersected and joined together creating semi-continuous CLL-like columns instead of an array of CLLs. We will refer to this structure as the continuous fin dipole structure. Interestingly, it was discovered that this structure results in very favorable performance, outperforming the planar CLL-loaded dipole antennas previously presented in this thesis. Results will be further explained below.

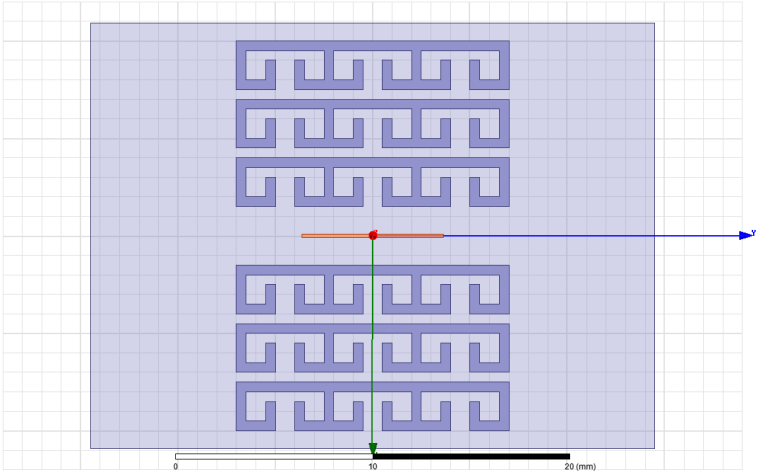

Figure 4.38: Continuous Fin Dipole Antenna

As shown in Figure 4.39 of S_{11} return loss, the bandwidth of this design is noticeably wider than previous designs. The S_{11} return loss is below -9.0dB between 12.3GHz and 17.0GHz, a band of 4.7GHz or ~32% bandwidth. Similarly, this antenna outperforms the conventional dipole ($G_{realized}$>2.2dB) from 12.6GHz to 17.9GHz, a band of 5.3GHz or ~35% bandwidth. By this measure, the performance enhancement bandwidth of the continuous fin dipole presented here is greater than that of conventional Yagi-Uda antenna designs. This will be discussed further in the next chapter.

The 3-D gain pattern for this antenna is shown in Figure 4.40. As shown in Figure 4.41, the maximum realized gain for this antenna is 8.5dB at 17.1GHz. The S_{11} return loss at this frequency is approximately -9.0dB. As a result, simply by placing these continuous fins on-plane around a conventional planar dipole antenna, the maximum realized gain can be enhanced by over 6.0dB. As with the previous designs, the fins can be rotated radially around the dipole to produce a mechanically scanned beam.

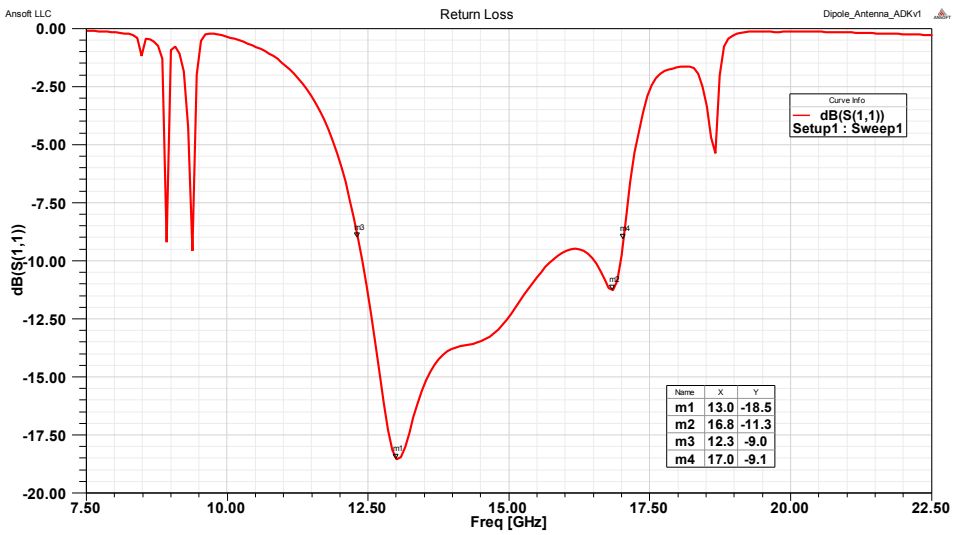

Figure 4.39: S_{11} Return Loss for Continuous Fin Dipole Antenna

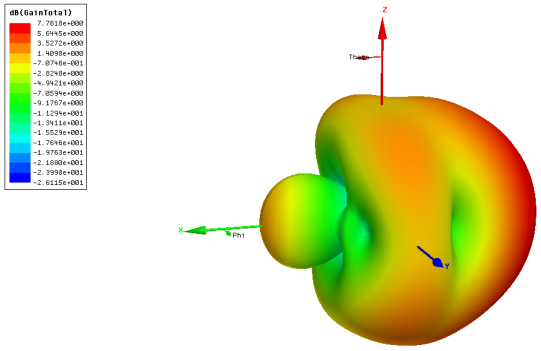

Figure 4.40: Improved Planar Structure; Max Realized Gain: 8.5 dB at 17.1 GHz

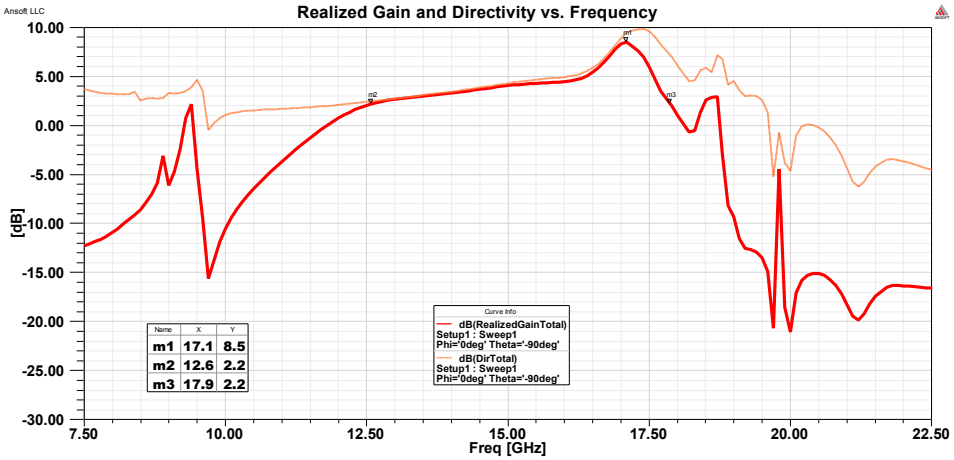

Figure 4.41: Plot of Directivity and Realized Gain vs. Frequency for Multiple Cuts

4.10 Other Variants of CLL-Loaded Dipoles

Several other orientations of CLLs placed around the dipole antenna were simulated in search of other variations of the antenna enhancement structure. The two variations of the CLL-loaded dipole antenna shown below provide interesting results; however, the enhancements observed are not as strong as previously shown designs. The objective for these simulations was to rule out possible design variations.

4.10.1 Variation A of CLL-Loaded Dipole Antenna

Some variations of the CLL-loaded dipole antenna were simulated to compare performance. The first variation, shown in Figure 2.43, has all of the CLL faces perpendicular to the dipole antenna. The return loss of this antenna, shown in Figure 4.43, has a resonance at 17.2GHz. At this frequency, the maximum gain is 4.35dB, as shown in Figure 4.44. This antenna structure is useful because it takes the standard dipole radiation pattern and squishes it in elevation, resulting in an omnidirectional antenna with approximately 4.35dB gain.

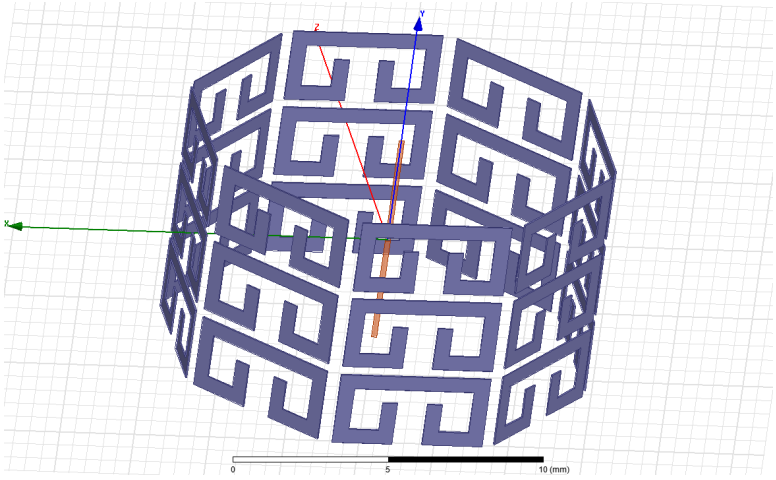

Figure 4.42: Variation A of CLL-Loaded Dipole Antenna

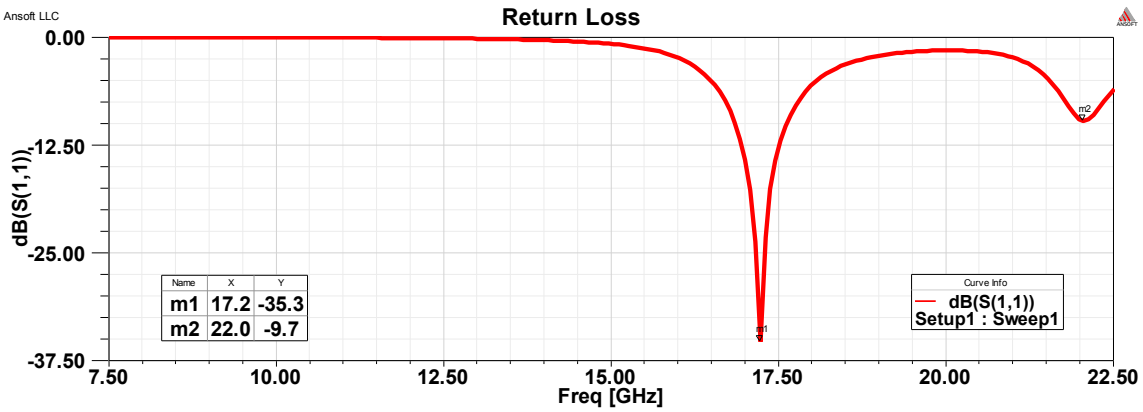

Figure 4.43: S_{11} Return Loss of Variation A of CLL-Loaded Dipole Antenna

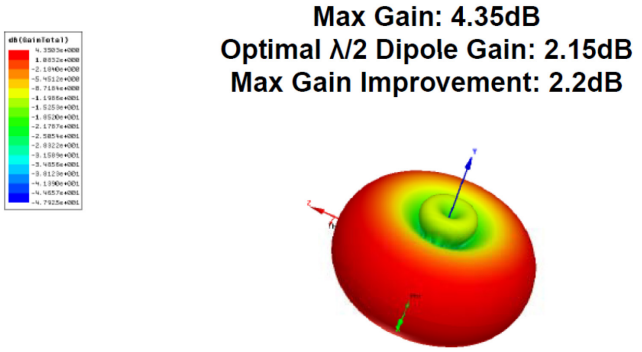

Figure 4.44: Gain Pattern of Variation A of CLL-Loaded Dipole Antenna

4.10.2 Variation B of CLL-Loaded Dipole Antenna

Another logical orientation of CLL fins that was simulation was with open ends of the CLL loops pointing downward as seen in Figure 4.45. The particular orientation of individual CLLs is the same relative to the incoming wave as that in the periodic unit cell analysis done in Chapter 2 of this thesis. In that chapter, we previously showed that an infinite array of unit CLLs of this type exhibited negative magnetic permeability over a given frequency range as well as exhibiting a high-μ frequency band. The return loss of this antenna is shown in Figure 4.46.The main drawback of this structure in terms of engineering a directive beam enhanced gain antenna is that the structure is symmetric across the y-axis, shown in Figure 4.47. Due to this symmetry, it has no physical mechanism to potentially restrict any less than a hemisphere.

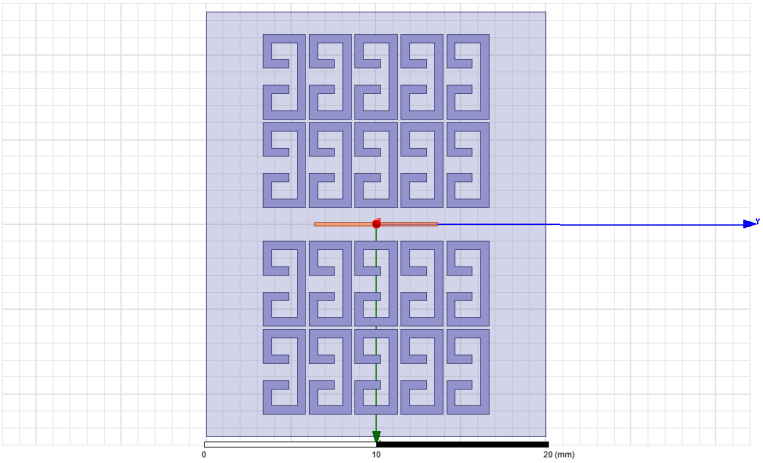

Figure 4.45: Variation B of CLL-Loaded Dipole Antenna

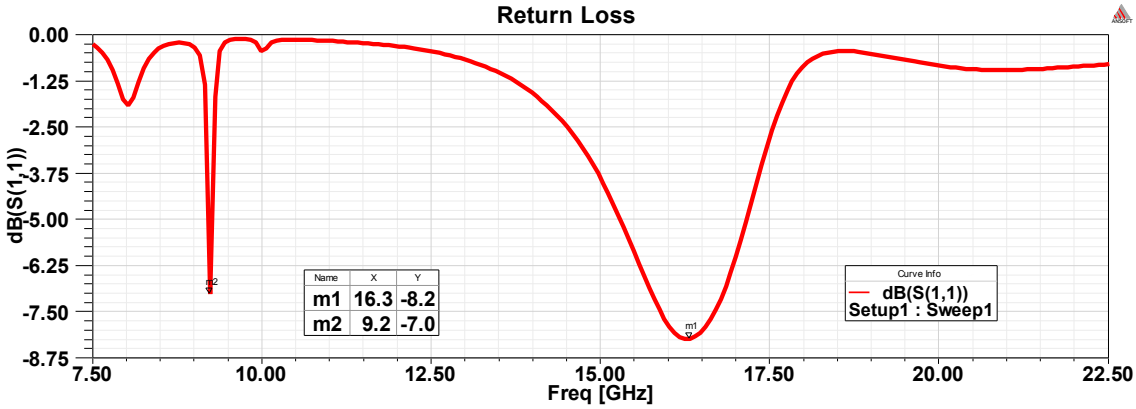

Figure 4.46: S_{11} Return Loss of Variation B of CLL-Loaded Dipole

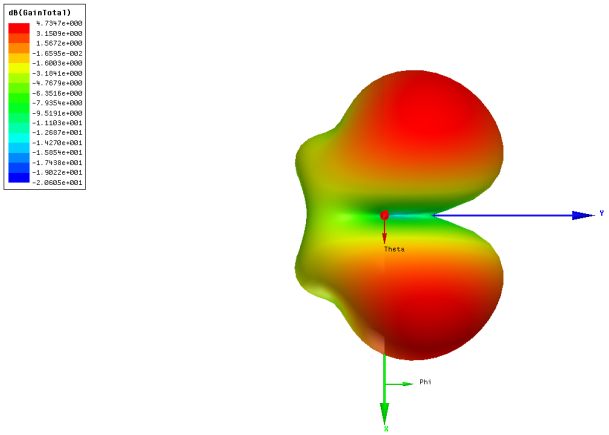

Figure 4.47: 3-D Gain Pattern; Max Gain: 4.7 dB at 16.2 GHz

4.11 Physically Measured Data

A planar version of the CLL-loaded dipole antenna was fabricated for physical testing. Due to fabrication capabilities, the antenna was scaled to resonate near 1.5GHz. The HFSS depiction is shown in Figure 4.48 and a photo of the fabricated antenna is shown in Figure 4.49. Physical measurements were taken and compared to HFSS simulations for that structure, as shown in Figure 4.50 and Figure 4.51. There was very good agreement in the S11 return loss plot the H-plane gain pattern. Measure data also showed a strong front-to-back ratio, as shown in Figure 4.52. More testing needs to be done; however, this physical proof of concept was successfully experimentally verified.

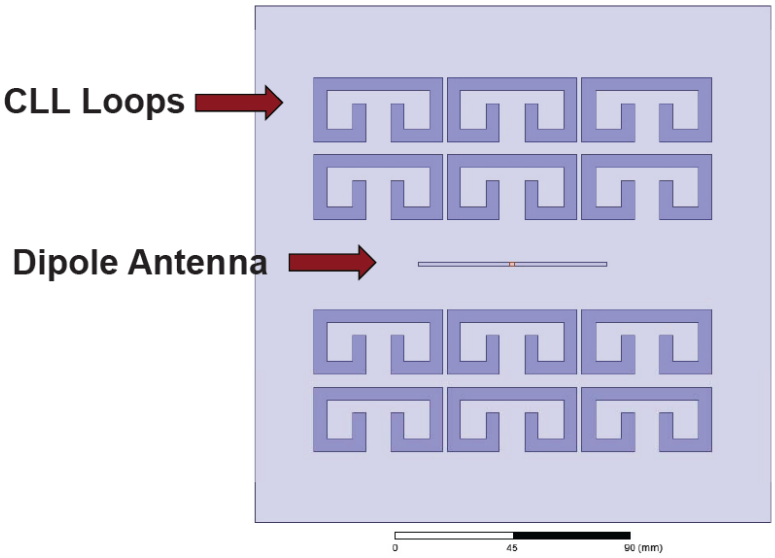

Figure 4.48: HFSS Depiction of Measured CLL-Loaded Dipole Antenna

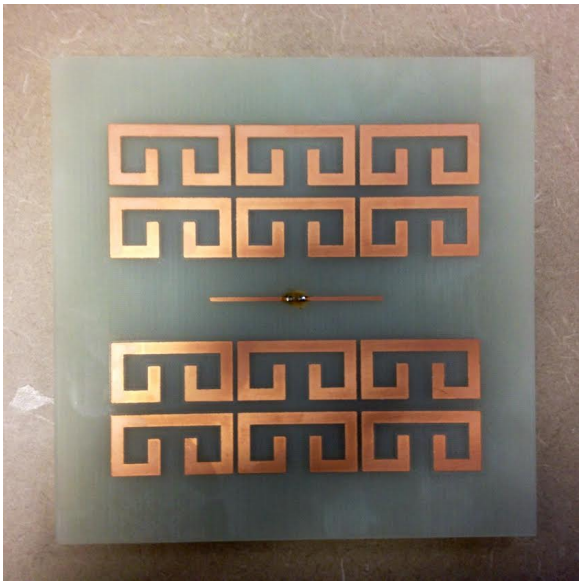

Figure 4.49: Photo of Physically Measured Antenna

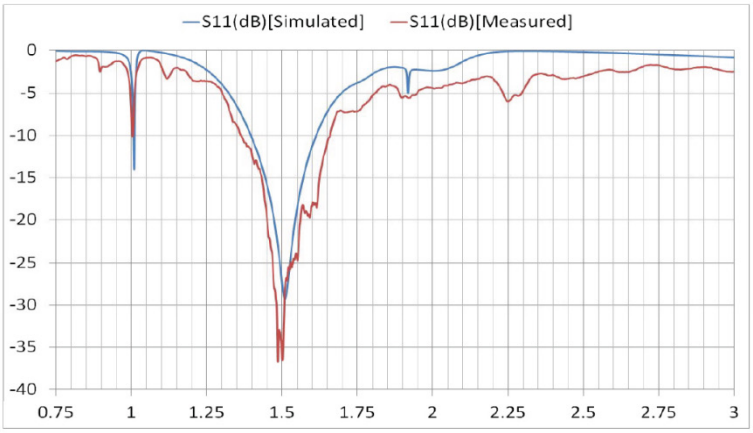

Figure 4.50: S_{11} Return Loss for Simulated vs. Measured CLL-Loaded Dipole Antenna

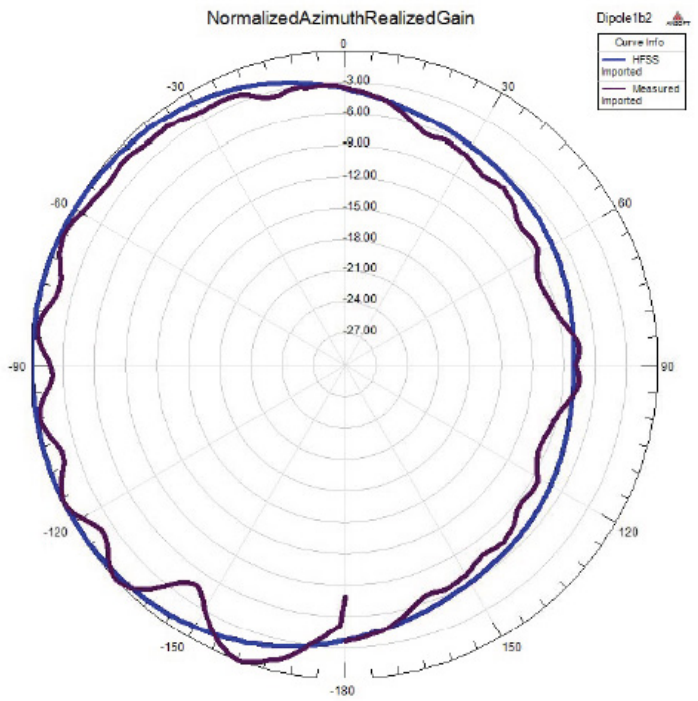

Figure 4.51: Realized Gain Pattern for Simulated vs. Measured CLL-Loaded Dipole Antenna

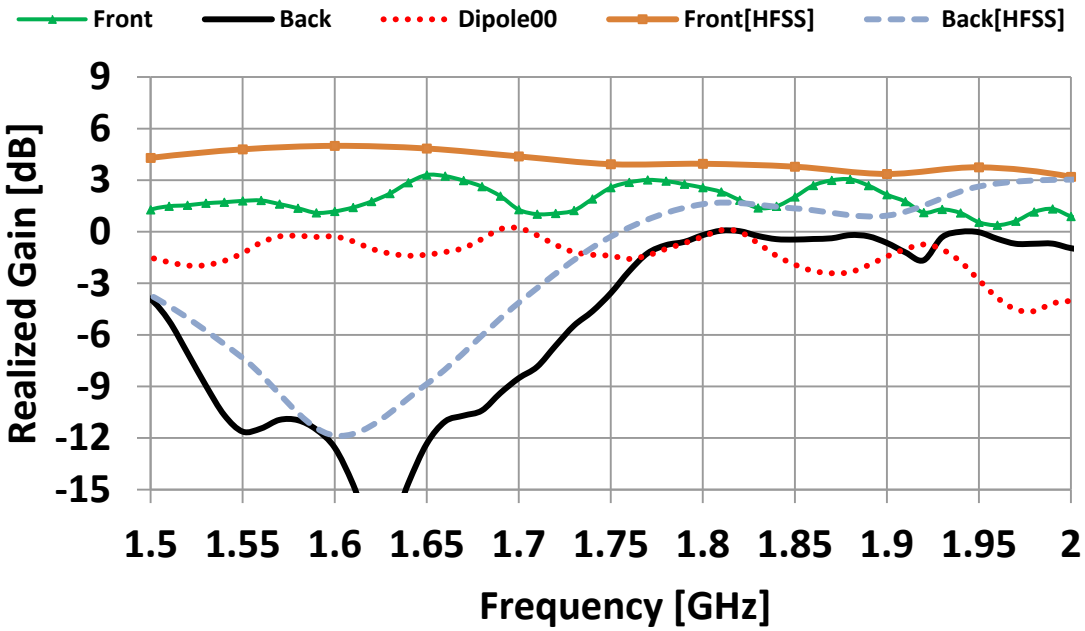

Figure 4.52: Realized Gain for Simulated vs. Measured CLL-Loaded Dipole Antenna

4.12 Conclusion

Beginning within the frame of AMC design using CLL-based metamaterials at microwave frequencies, an innovative metamaterial structure was developed to enhance a standard dipole

antenna by making it directive and with high realized gain. This study showed that a strong gain enhancement can be realized by placing a single planar fin consisting of six CLLs electrically close to the dipole rather than using a large volumetric block of backplane as done in previous studies.

In addition, while many previous studies have focused on creating planar metamaterial structures for low-profile antennas, this study also presents an innovative radial arrangement of CLL loops around a dipole antenna that create a directive antenna beam based on the reflection and transmission coefficients of the radial CLL fins. While this study utilized a dipole antenna, it is believed that this type of structure can be generalized to enhance a broader class of antennas, including wide-band antennas or monopoles.

The interaction of waves transmitted by the antenna with the CLL fins is of particular interest. Future work will seek to investigate the precise mechanisms for transmission and reflection of the fin structures based on orientation and will also investigate the limit at which increasing the number of radial CLL fins will no longer increase directivity of the transmitted beam.

Chapter 5: Comparison of CLL-Loaded Dipole Antenna Structures to Yagi-Uda Antenna

5.1 Introduction

It has been recognized that the CLL-loaded dipole antenna presented in the previous chapter draws comparisons to the Yagi-Uda antenna, depicted in Figure 5.1. Both antenna structures consist of a single driven linear dipole antenna with other parasitic radiating elements whose currents are induced by mutual coupling. Yagi-Uda antennas operate by using mutual coupling between standing-wave current elements to produce a traveling-wave unidirectional pattern. The Yagi-Uda antenna was first described in English in 1926 by Professor H. Yagi and (then) Instructor S. Uda at Tohoku University [49]. The design of the Yagi-Uda antenna achieves a very substantial increase in the antenna's directivity and gain compared to a simple dipole. This antenna operates by having the parasitic elements in the forward beam act as radiation directors while those in the rear act as radiation reflectors [50]. Typical Yagi-Uda antennas are built to operate only as end-fire arrays, which are precisely tuned such that a row of director elements will act as a traveling wave antenna.

To achieve the end-fire beam formation, the parasitic elements in the direction of the beam are somewhat smaller in length than the feed element [50]. Generally, the driven element is resonant with its length slightly less than $\lambda/2$ (usually 0.45–0.47λ) whereas the lengths of the directors should be slightly shorter (about 0.4 to 0.45λ) and the reflector slightly longer (about 0.48-0.50 λ). In many cases, the director elements are not exactly the same length or diameter. The separation between the directors is typically 0.2 to 0.25λ, and it is not necessarily uniform for optimum designs. The linear dipole Yagi-Uda array, such as the one depicted in Figure 5.1, is commonly used in industry and is widely used for broadcast television reception.

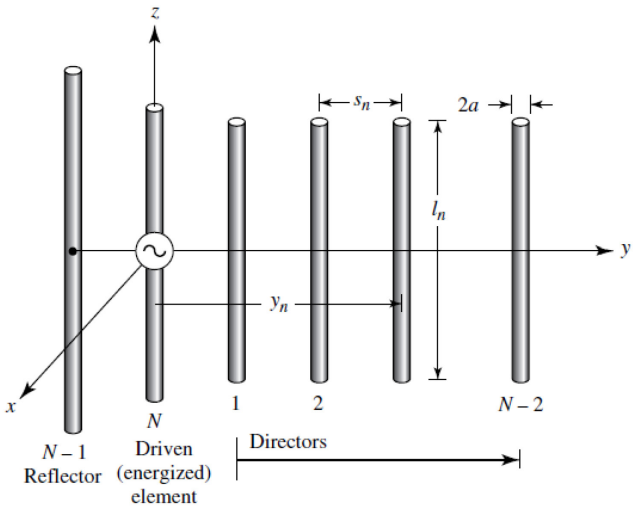

Figure 5.1: Conventional Yagi-Uda Antenna Array [50]

5.2 Operation of the Yagi Antenna

As described by Balanis, since the length of the each director is smaller than its corresponding resonant length, the impedance of each is capacitive and its current leads the reduced emf [50]. Conversely, the impedance of the longer reflector is inductive and the phases of the currents lag those of the induced emfs. In addition, the total phase of the currents along the directors and reflectors is not determined solely by the length of the element, but also by the spacing between each adjacent element. If the parasitic elements are given lengths slightly less than their corresponding resonant lengths, they will operate as directors because they form an array with currents that are approximately equal in magnitude with an equal progressive phase shifts, resulting in a traveling wave in the direction of the directors. Similarly, a properly spaced element slightly longer in length than the driven element will act as a reflector by causing a phase shift in the opposite direction. When the directive and reflective elements are properly spaced, the summation of the radiating fields from all of the elements are in-phase in one direction and out of phase in the other direction, depicted in Figure 5.2.

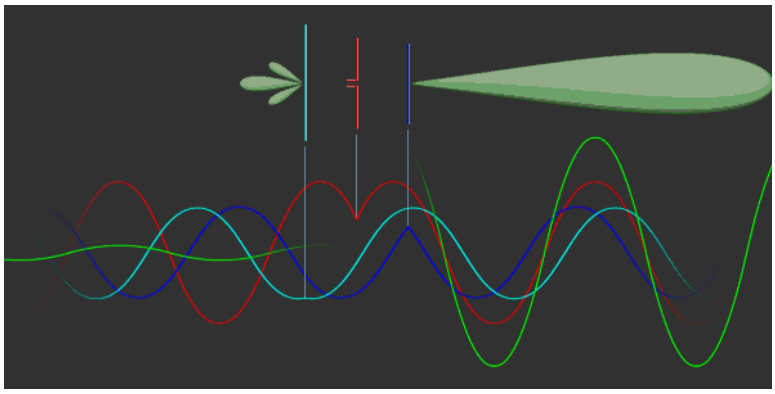

Figure 5.2: Depiction of the Individual and Summed Waves Transmitted by a 3-element Yagi-Uda Antenna [51]

It is also noted by Balanis that a single reflecting element is generally used because very little performance enhancement is gained with the Yagi-Uda antenna by having multiple reflectors [50]. As described above, considerable improvements can be realized in the antenna gain by increasing the number of directors. However, as the number of director elements on the Yagi-Uda antenna becomes large, the marginal improvement of adding each additional element in terms of realized gain begins to diminish. This reduction in performance enhancement creates a practical limit on the number of directors used due to total physical length considerations.

The lengths and diameters of the directors and reflectors, as well as their respective spacing, determine the optimum characteristics of the Yagi-Uda antenna. Generally, numerical methods are used to optimize the lengths and spacing of each element to maximize the realized gain.

According to Balanis, the reflector spacing and size have negligible effects on the forward gain and large effects on the backward gain (front-to-back ratio) and input impedance, and they can be used to control or optimize antenna parameters without affecting the gain significantly [50]. The feeder length and radius have a small effect on the forward gain but a large effect on the backward gain and input impedance. The size and spacing of the directors have a large effect on the forward gain, backward gain, and input impedance, and they are considered to be the most critical elements of the array.

While the Yagi-Uda antenna provides an impressive amount of directivity and gain, it also has several drawbacks. Usually, Yagi-Uda arrays have low input impedance and relatively narrow bandwidth of about ~2% [50]. In addition, this antenna is very sensitive to the length and spacing of each element as discussed above. Non-optimal element length and spacing values will result in an impedance mismatch and a drastic reduction in realized gain.

The performance of the Yagi-Uda antenna can be analyzed in detail using a rigorous integral equation method of moment technique to calculate the complex current distributions on all of the elements and the electric field distributions radiated by the elements. This data can be used to calculate the far-field radiation patterns, input impedance, bandwidth, front-to-back ratio, and other relevant parameters. Methods of analysis used by Balanis are based on Pocklington's integral equation [50]. This theory solves for the total electric field generated by an electric current source radiating in free-space, as seen in equation 5.1 below. A similar analytical method could be used to analyze the CLL-loaded dipole structure in future works.

$$\int_{-l/2}^{+l/2} I(z')\left(\frac{\partial^2}{\partial z^2}+k^2\right)\frac{e^{-jkR}}{R}dz' = j4\pi\omega\varepsilon_0 E_z \tag{5.1}$$

$$R = \sqrt{(x-x')^2+(y-y')^2+(z-z')^2} \tag{5.2}$$

In the previous chapter, it was shown that the CLL-loaded dipole antenna structure uses its surrounding CLL fins as directors and reflectors of the radiated fields from the driven dipole. It was shown that this was the case when the fins consisted of an array of discrete CLLs as well as when the CLLs were joined together to make vertically continuous radiation fins acting as reflectors and directors. Well established analytical and numerical results from the Yagi-Uda antenna provide an opportunity and a framework to better understand the CLL-loaded dipole antenna that began as a metamaterial exploration. One of the most important insights from comparing the CLL-loaded dipole antenna to the Yagi-Uda antenna is that there is still much future work that can be done either analytically or numerically to optimize the spacing and sizes of the CLL fins around the dipole to further enhance the directivity and realized gain. Methods such as a detailed perturbation analysis or genetic algorithm could be used in future works to optimize the performance of the CLL-loaded dipole. One major distinction between the two designs is that the Yagi-Uda only works as planar structure, but cannot be radially arrayed to further increase the gain. While the optimized Yagi-Uda antenna of similar aperture size outperforms the maximum directivity of the CLL-loaded dipole presented in this paper presents an innovative design, not known to be previously realized in published literature, which still has much opportunity for optimization and some distinct advantages over the Yagi-Uda antenna.

As shown in the previous chapter, it is possible to enhance the gain of the planar CLL-loaded dipole structure by adding additional pairs of CLL fins radially around the vertical axis of the dipole. In addition to having the ability to increase the maximum gain of the antenna structure by

increasing the length of the CLL fin in the radial direction away from the dipole, the ability to increase maximum gain by transforming the planar antenna structure to a multi-fin three dimensional structure provides an additional mechanism not available to the Yagi to enhance gain. Another advantage of the CLL-based structure is that the parasitic (non-fed) director and reflector elements can be placed much closer to the driven dipole element without degrading transmission performance of the antenna. The Yagi-Uda antenna requires that parasitic elements typically be spaced 0.2-0.3*λ away from the driven element; however, the discrete and continuous CLL fins can be placed <λ/40 from the driven dipole and still provide significant realized gain. It has also been observed through the observation of tweaking and perturbing different spacing and length parameters that the CLL-loaded dipole antenna is much less sensitive to these parameters than a comparable Yagi-Uda antenna. Another advantage of the CLL-loading fins compared to the Yagi-Uda is that the CLL fins can be placed around a range of different dipole lengths and still achieve enhanced realized gain, while the parasitic and driven Yagi elements must all have precise lengths and spacing to achieve strong performance.

5.3 Simulation of Conventional Yagi-Uda Antennas

5.3.1 Planar Dipole (7.27mm) Yagi-Uda w/ 0.4λ Aperture Length

In this section, the results for a standard planar Yagi-Uda antenna are shown with one director and one reflector as shown in Figure 5.3. The distance between the farthest director and the reflector is 0.4λ. The dimensions and spacing of each element was determined by published data by Balanis [50]. The return loss is shown in Figure 5.4. The maximum realized gain of this antenna is 8.0 dB at 18.2 GHz as shown in Figure 5.5 and Figure 5.6.

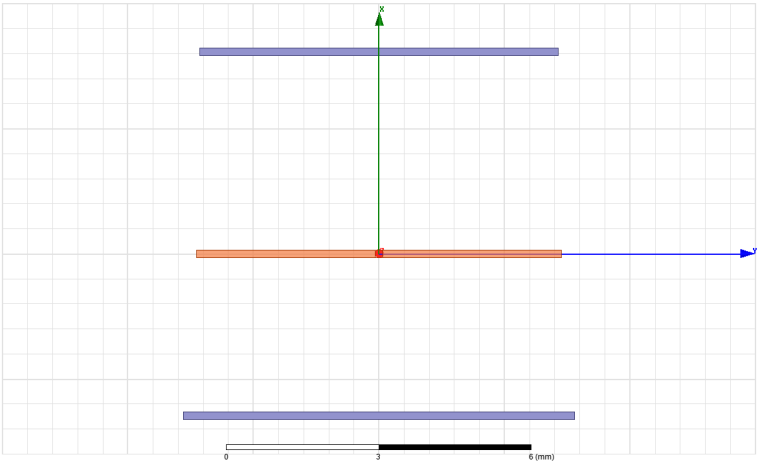

Figure 5.3: Planar Dipole (7.27mm) Yagi-Uda w/ 0.4λ Aperture Length

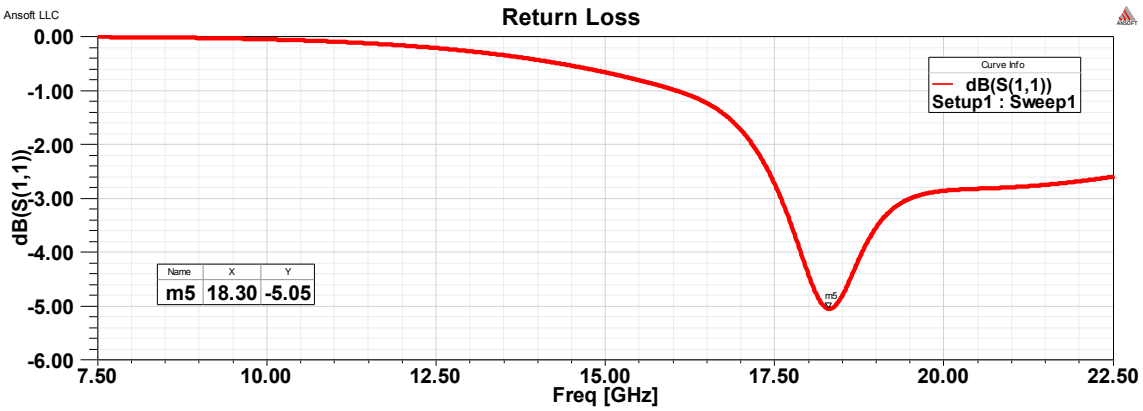

Figure 5.4: S_{11} Return Loss Planar Dipole (7.27mm) Yagi-Uda w/ 0.4λ Aperture Length

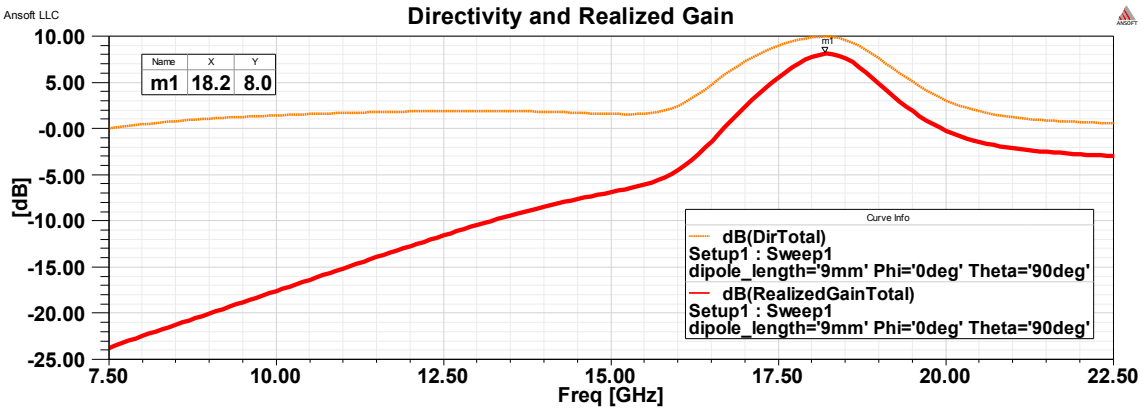

Figure 5.5: Directivity and Realized Gain vs. Frequency for Planar Dipole (7.27mm) Yagi-Uda w/ 0.4λ Aperture Length

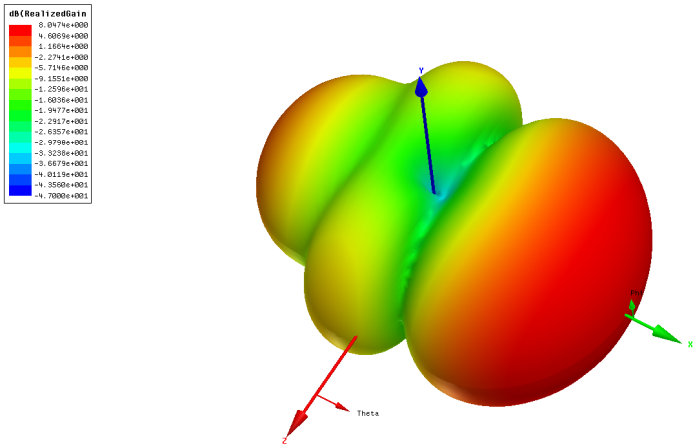

Figure 5.6: Realized Gain for Planar Dipole (7.27mm) Yagi-Uda w/ 0.4λ Aperture Length; Max Realized Gain: 8.0 dB at 18.2 GHz

5.3.2 Planar Dipole (7.27mm) Yagi-Uda w/ 0.8λ Aperture Length

In this section, the results for a standard planar Yagi-Uda antenna are shown with three directors and one reflector as shown in Figure 5.7. The distance between the farthest director and the reflector is 0.8λ. The dimensions and spacing of each element was determined by published data by Balanis [50]. The return loss is shown in Figure 5.8. The maximum realized gain of this antenna is 10.0 dB at 18.5 GHz as shown in Figure 5.9 and Figure 5.10.

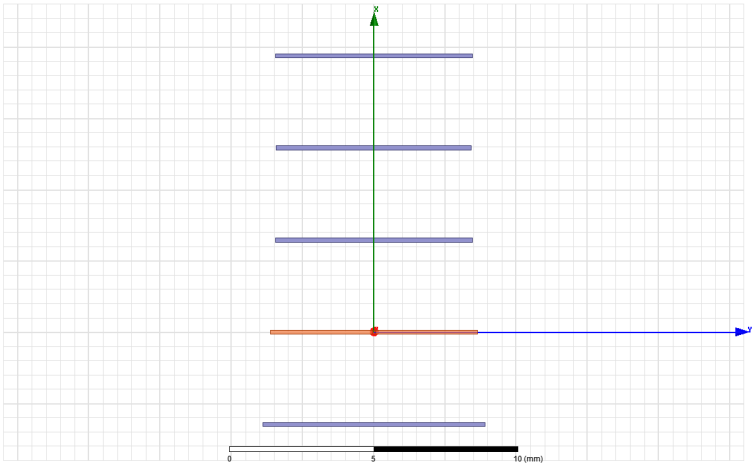

Figure 5.7: Planar Dipole (7.27mm) Yagi-Uda w/ 0.8λ Aperture Length

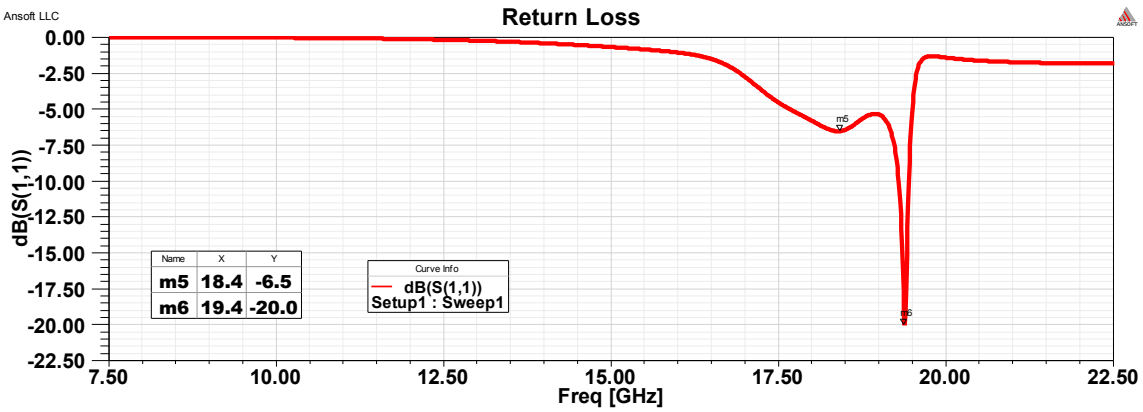

Figure 5.8: S_{11} Return Loss Planar Dipole (7.27mm) Yagi-Uda w/ 0.8λ Aperture Length

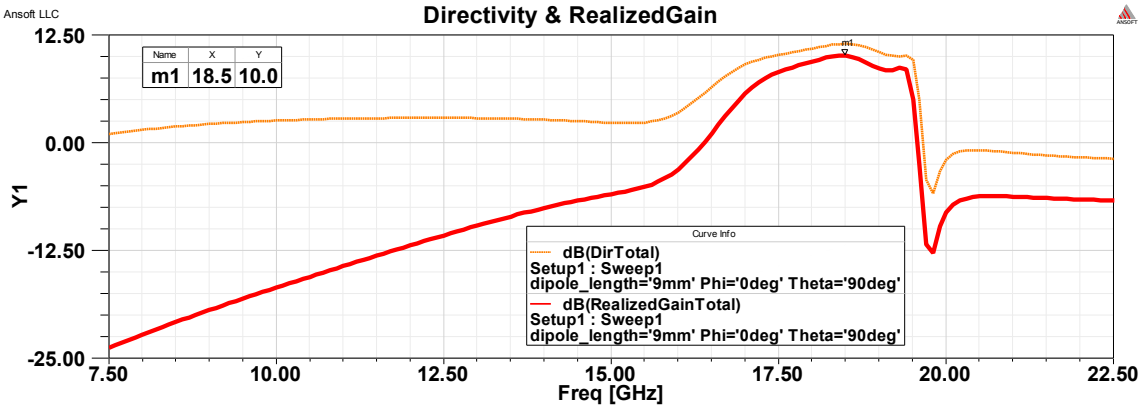

Figure 5.9: Directivity and Realized Gain vs. Frequency for Planar Dipole (7.27mm) Yagi-Uda w/ 0.8λ Aperture Length

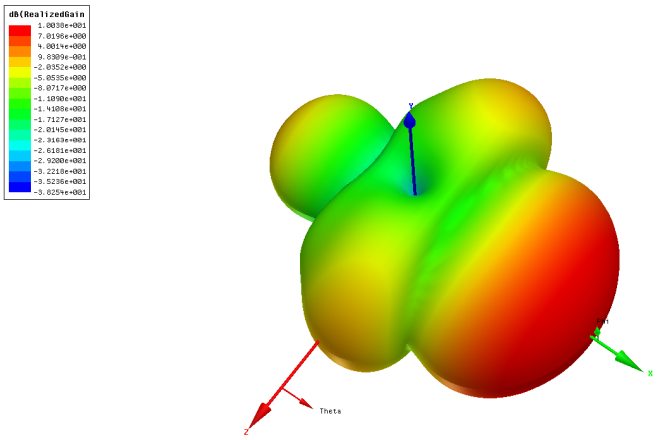

Figure 5.10: Realized Gain for Planar Dipole (7.27mm) Yagi-Uda w/ 0.8λ Aperture Length; Max Realized Gain: 10.0 dB at 18.5 GHz

5.3.3 Planar Dipole (7.27mm) Yagi-Uda w/ 1.2λ Aperture Length

In this section, the results for a standard planar Yagi-Uda antenna are shown with four directors and one reflector as shown in Figure 5.11. The distance between the farthest director and the reflector is 1.2λ. The dimensions and spacing of each element were determined by published data by Balanis[50]. The return loss is shown in Figure 5.12. The maximum realized gain of this antenna is 11.7 dB at 18.6 GHz as shown in Figure 5.13 and Figure 5.14.

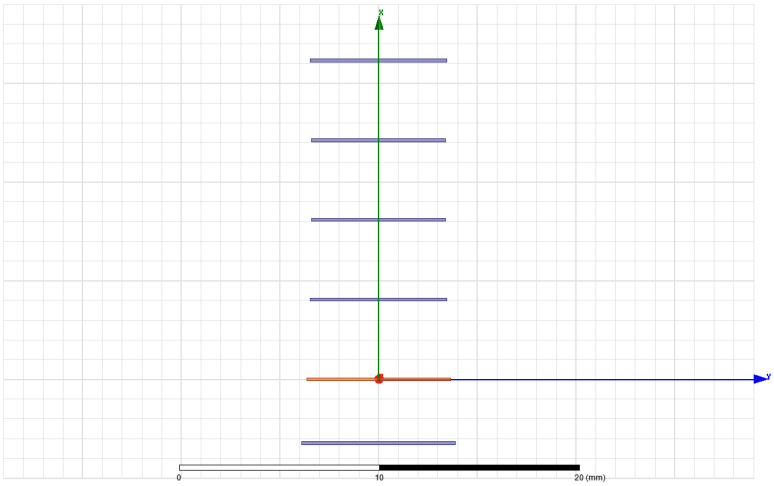

Figure 5.11: Planar Dipole (7.27mm) Yagi-Uda w/ 1.2λ Aperture Length

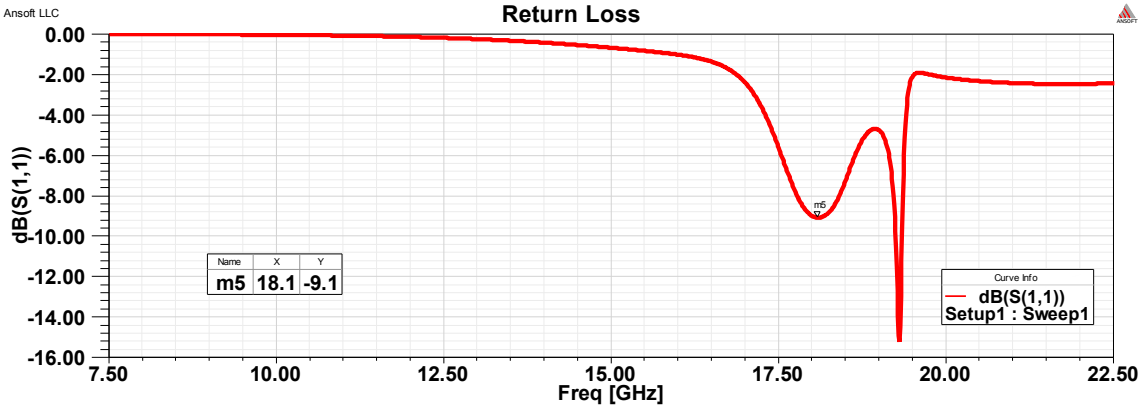

Figure 5.12: S_{11} Return Loss Planar Dipole (7.27mm) Yagi-Uda w/ 1.2λ Aperture Length

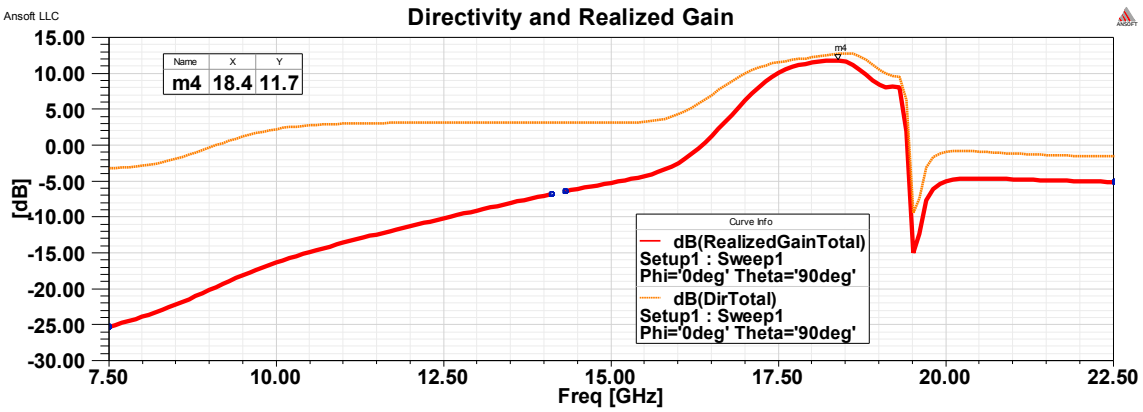

Figure 5.13: Directivity and Realized Gain vs. Frequency for Planar Dipole (7.27mm) Yagi-Uda w/ 1.2λ Aperture Length

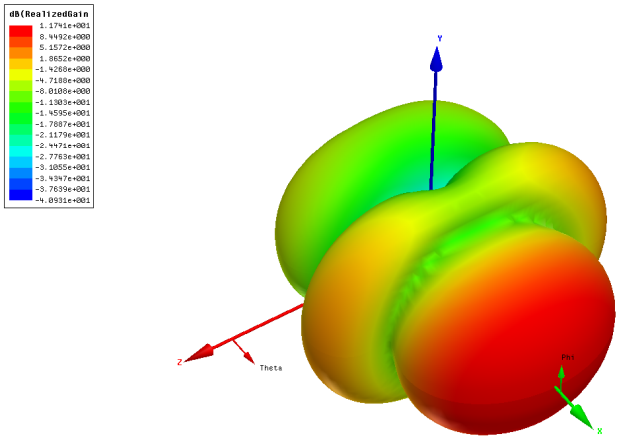

Figure 5.14: Realized Gain for Planar Dipole (7.27mm) Yagi-Uda w/ 1.2λ Aperture Length; Max Realized Gain: 11.7 dB at 18.6 GHz

Table 4 shows a summary of the performance of various Yagi-Uda antennas that were simulated to compare to the various CLL-loaded fin antenna designs.

# of Directors	Aperture Length	Dipole Length (mm)	Operating Freq. (GHz)	Max Realized Gain (dB)	Return Loss (dB)
0	N/A	7.27	19.0	**2.6**	-15.1
1	0.4λ	7.27	18.2	**8.0**	-5.1
3	0.8λ	7.27	18.5	**10.0**	-6.5
4	1.2λ	7.27	18.3	**11.7**	-9.1
0	N/A	9.0	15.4	**2.3**	-16.3
1	0.4λ	9.0	14.8	**8.2**	-5.7
3	0.8λ	9.0	14.8	**9.8**	-5.8
4	1.2λ	9.0	14.9	**11.3**	-9.3

Table 4: Summary of Conventional Yagi-Uda Antenna Results

5.4 Size Comparison to CLL-Loaded Dipole Antenna

One method of sized comparison used in comparing different Yagi-Uda designs [50] is to measure the distance from the reflector to that of the furthest director, giving a measure of aperture length. We will use this measure to compare the size of the CLL-loaded dipole antennas to that of the Yagi-Uda. Optimally, an antenna with a smaller aperture distance and greater maximum realized gain than the conventional Yagi-Uda antenna is desired. However, the Yagi-Uda antenna has been optimized as a result of many studies over the years, making this a very challenging task. A size comparison between one of the CLL-loaded dipoles and the single director, single reflector Yagi-Uda antenna is shown in Figure 5.15.

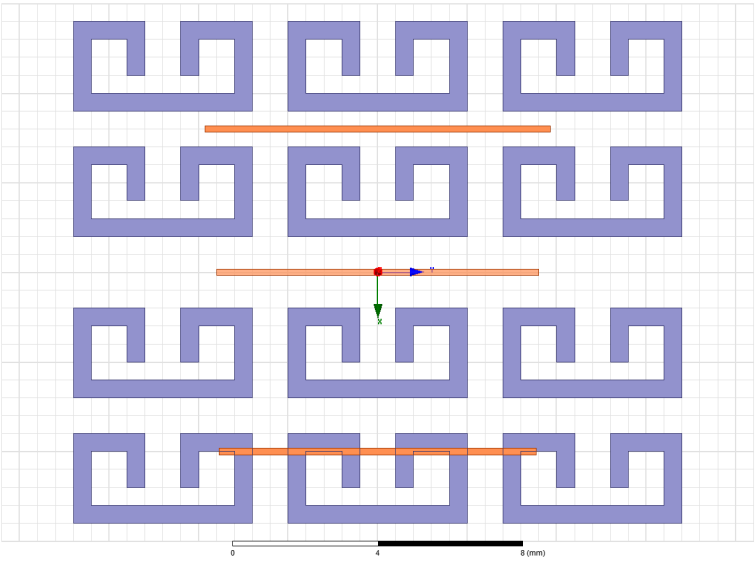

Figure 5.15: Overlay of 0.4λ Yagi-Uda Antenna and Planar CLL-Loaded Dipole for Size Comparison

5.5 Analysis and Conclusion

In this chapter, it was shown that CLLs can provide antenna enhancement in two distinctively different manners. First, it was shown that a single thin CLL fin consisting of only six CLLs can be placed electrically close to a dipole antenna rather than using a larger volumetric block or backplane surface. This miniaturized lower profile design still provides over 4dB enhancement in the maximum realized gain compared to the standard dipole antenna. This method of performance occurs when the free-space resonance of the dipole matches the free space resonance of the open-ended CLL loops. The operation of the loops can be classified as a metamaterial effect, and it is believed that the loops provide an AMC-like response.

The second method, where loaded CLLs are placed electrically close to the dipole antenna to create both planar and radial reflectors and directors, operates at a frequency where the free space resonance of the λ/2 dipole is several GHz above that of the CLL loops. The combined resonance of the dipole and the CLL loops together in this manner increases the resonant frequency of the radiating structure approximately 30% above that of the same dipole in free space. Since this structure operates noticeably above the resonate region of the CLL loops, this method of operation should be considered as a single fed parasitic array, similar to the Yagi-Uda antenna, rather than as a metamaterial antenna.

Currently, the Yagi-Uda antenna outperforms the CLL load fin designs presented in this work in terms of maximum realized gain. However, there are a few advantages of the CLL-loaded dipole antenna that should be noted. The Yagi-Uda antenna has been studied many times since it was first invented in the 1920s, and the spacing and sizes of each reflector and director have been very carefully fine-tuned. The CLL fin dipole antenna structures presented in this work have not yet been fine-tuned for performance enhancement to the same degree, so there is still much room for antenna optimization. There are still many fin size and spacing variations that have yet to be tested. However, the initial performance is promising. The radial 12-fin dipole antenna and the planar continuous fin dipole antenna showed the strongest antenna performance and are in the ball park of the Yagi-Uda antenna.

In addition, the performance of the Yagi-Uda antenna is very sensitive to the spacing and sizes of each director and reflector due to careful impedance matching issues. However, our CLL fin has been shown to be more robust in terms of size and spacing tolerance of the director and reflector fins. Our simulations have shown that the CLL-loaded dipole antennas have a much more directive main beam with lower side lobes and back lobes compared to the simulated Yagi-Uda antennas using various numbers of directors.

Most importantly, this thesis presents an innovative concept of radially placing the CLL fins around the dipole at an electrically close distance to increase directivity and maximum realized gain of the antenna. While there is obviously some limit, this study has shown that maximum gain increases and beamwidth becomes more directive as more evenly spaced directors and reflectors are added around the dipole antenna. The same concept of radially arraying reflectors and directors was applied to the Yagi-Uda antenna; however, gain was reduced compared to the planar case rather than enhanced. Hopefully, this innovative radially array gain enhancement effect can be utilized to give a dipole antenna radially loaded with metallic elements a greater performance than the rival Yagi-Uda design.

Chapter 6: Conclusions and Future Work

6.1 Thesis Summary

The early chapters of this thesis have shown that engineered electromagnetic metamaterials have been able to open the door to new exotic material responses, such as negative index of refraction, not previously seen in conventional materials. The ability to precisely tune and control a medium's effective constitutive parameters opens the door for many novel devices and engineering applications that were previously impossible.

It was shown that the CLL is a robust unit-inclusion that provides a strong magnetic response near its resonant frequency, resulting in a negative permeability over a frequency band. Multiple metamaterial configurations utilizing the CLL were shown to characterize its performance. The CLL can be frequency scaled and used in place of the more popular SRR in many previously designed material structures. It was demonstrated in simulation that a periodic array of CLL must be paired with continuous metal wire rather than cut metal wire to achieve a negative index of refraction. Interestingly, it has been shown that the CLL can demonstrate a negative index of refraction at two different frequency regions, based on whether the inclusions are oriented perpendicular or parallel to the incident wave respectively. The largest drawback to conventional metamaterial designs is their inherent narrow bandwidth and high loss.

Randomized metamaterial structures were generated and simulated in HFSS for material characterization. While negative or less than one permittivity or permeability parameters were not able to be shown, the metamaterials were characterized and shown to operate as a bandstop RF filter that transmits power outside of a narrow highly lossy frequency band based on the resonance of the loops. These structures would be useful for blocking a particular desired frequency in communications or radar applications. The S-parameter magnitude response of the randomized structures tends to stay fairly consistent, despite the random seed value.

In the later chapters of this work, the performance of planar dipole antennas were analyzed when being loaded with electrically close CLL elements. It was shown that a small number of electrically close CLLs fins can effectively produce a lower-profile AMC-like antenna backplane providing strong gain enhancement.

In addition, it was shown in HFSS simulations that the CLLs can be used above resonance to create reflector and director fins, providing gain enhancement as a single-fed parasitic array. These fins can enhance the dipole even when placed very electrically close to the radiating element. It was demonstrated in an innovative manner that these CLL fins can be radially arrayed around a standard radiating dipole to transform the omnidirectional donut gain pattern into a highly directive main beam with low side lobes and a dramatically enhanced maximum gain. In the planar configuration, it was shown that the CLLs can be joined together to further enhance the maximum gain of the antenna. A frequency scaled version of the CLL-loaded dipole antenna was fabricated and physically measured in an anechoic chamber. The physical measurements were fairly consistent with simulation data, and the physical antenna demonstrated a strong front-to-back ratio. The demonstrated designs were compared and contrasted to the similar Yagi-Uda antenna.

The main goal was to characterize CLLs and random metamaterial structures while also using CLLs and metamaterials to enhance antenna performance and improve antenna design. While this work has created many new questions that have yet to be answered, major steps forward have been taken in both the metamaterial characterization and antenna enhancement areas. This lays the groundwork for a potential future Ph.D work to extend and perform a more complete theoretical analysis of the work presented in this thesis. Hopefully, results from this work can be used to better understand and help create improved engineered materials and next-generation devices.

6.2 Future Work

Future work from this study can take several directions. As with many studies in metamaterials and electromagnetics, reducing loss and increasing bandwidth for all applications would be desired. Metamaterials can also be enhanced by making their performance more isotropic. For the antenna applications, greater maximum gain and increased bandwidth are the major areas of focus. One goal is to further improve and optimize the dipole enhanced CLL antenna operating as a parasitic array to further enhance realized antenna gain and directivity. A major achievement would be to create a CLL-based parasitic array design that surpasses performance of the conventional Yagi-Uda antenna. Another goal is to improve AMC performance of the CLL loops when placed electrically close to an antenna resonating at a similar frequency to that of the loops.

To better understand the electromagnetic response of random metamaterial structures, a detailed analytical formulation of random metamaterials is needed. Further, improved methods of simulation for these electrically large random structures are needed in a manner that increases accuracy and is less computationally expensive. Currently, high performance machines can only manage to simulate relatively small quasi-random structures in a reasonable amount of time.

Lastly, it is hoped that the work on CLLs can be extended to applications using CLLs for transformation optics applications to engineer novel impedance-varying metasurfaces and enhanced AMCs.

Reference List:

[1] D. R. Smith, W. J. Padilla, D. C. Vier, S.C. Nemat-Nasser, and S. Schultz, "Composite medium with simultaneously negative permeability and permittivity," *Phys. Rev. Lett.*, vol. 84, pp. 4184–4187, May 2000.

[2] D. R. Smith and N. Kroll, "Negative refractive index in left-handed materials," *Phys. Rev. Lett.*, vol. 85, pp. 2933–2936, Oct. 2000.

[3] Kafesaki, M., Koschny, T., Penciu, R. S., Gundogdu, T. F., Economou, E. N., & Soukoulis, C. M. (2005). Left-handed metamaterials: detailed numerical studies of the transmission properties. *Journal of Optics A: Pure and Applied Optics*, *7*(2), S12.

[4] Pendry, J. B., & Smith, D. R. (2004). Reversing light with negative refraction. *Physics Today*, *57*, 37-43.

[5] Pendry, J. B., Holden, A. J., Robbins, D. J., & Stewart, W. J. (1999). Magnetism from conductors and enhanced nonlinear phenomena. *Microwave Theory and Techniques, IEEE Transactions on*, *47*(11), 2075-2084.

[6] Hand, T. H. (2009). *Design and applications of frequency tunable and reconfigurable metamaterials* (Doctoral dissertation, Duke University).

[7] Balanis, C. A. (2012). *Advanced engineering electromagnetics* (Vol. 111). John Wiley & Sons.

[8] Pozar, D. M. (2009). *Microwave engineering*. John Wiley & Sons.

[9] Engheta, N., & Ziolkowski, R. W. (Eds.). (2006). *Metamaterials: physics and engineering explorations*. John Wiley & Sons.

[10] Smith, D. R., & Pendry, J. B. (2006). Homogenization of metamaterials by field averaging. *JOSA B*, *23*(3), 391-403.

[11] Rumpf, R. (2014, Spring). Lecture #13: Metamaterials. *ECE 5390 Special Topics: 21st Century Electromagnetics*. Lecture From UTEP, El Paso, TX

[12] Ziolkowski, R. W., & Erentok, A. A metamaterial description of a volumetric artificial magnetic conductor. In *Proceedings of the 2004 URSI International Symposium on Electromagnetic Theory* (pp. 188-190).

[13] F. Auzanneau and R. W. Ziolkowski, "Microwave signal rectification using artificial composite materials composed of diode loaded, electrically small dipole antennas," *IEEE Trans. Microwave Theory Tech.*, vol. 46, no. 11, pp. 1628–1637, Nov. 1998.

[14] Ziolkowski and F. Auzanneau, "Ziolkowski and F. Auzanneau, "Passive artificial molecule realizations of dielectric materials".

[15] W. Ziolkowski, "Two time-derivative Lorentz material (2TDLM) formulation of a Maxwellian absorbing layer matched to a lossy media".

[16] Rotman, W. (1962). Plasma simulation by artificial dielectrics and parallel-plate media. *Antennas and Propagation, IRE Transactions on*, *10*(1), 82-95.

[17] Pendry, J. B., Holden, A. J., Stewart, W. J., & Youngs, I. (1996). Extremely low frequency plasmons in metallic mesostructures. *Physical review letters*, *76*(25), 4773.

[18] Vier, D., Fredkin, D. R., Simic, A., Schultz, S., & Tanielian, M. (2005). Experimental confirmation of negative phase change in negative index material planar samples. *Applied Physics Letters*, *86*(24), 241908.

[19] Chen, X., Grzegorczyk, T. M., Wu, B. I., Pacheco Jr, J., & Kong, J. A. (2004). Robust method to retrieve the constitutive effective parameters of metamaterials. *Physical Review E*, *70*(1), 016608.

[20] Smith, D. R., Vier, D. C., Koschny, T., & Soukoulis, C. M. (2005). Electromagnetic parameter retrieval from inhomogeneous metamaterials. *Physical Review E*, *71*(3), 036617.

[21] Larouche, S. (2008). Constitutive Parameter Retrieval From S-parameters. *Proprietary MATLAB Source Code*. Duke University, Durham, NC

[22] Shelby, R. A., Smith, D. R., & Schultz, S. (2001). Experimental verification of a negative index of refraction. *science*, *292*(5514), 77-79.

[23] Kong, J. A., MIT, "Characterization of Left-Handed Materials - 6.635 Lecture Notes. Massachusetts".

[24] Alù, A., & Engheta, N. (2003). Pairing an epsilon-negative slab with a mu-negative slab: resonance, tunneling and transparency. *Antennas and Propagation, IEEE Transactions on*, *51*(10), 2558-2571.

[25] D. R. Smith, D. C. Vier, N. Kroll, and S. Schultz, "Direct calculation of the permeability and permittivity for left-handed metamaterials," *Appl. Phys. Lett.*, vol. 77, pp. 2246–2248, Oct. 2000.

[26] R. A. Shelby, D. R. Smith, S. C. Nemat-Nasser, and S. Schultz, "Microwave transmission through a two-dimensional, isotropic, left-handed metamaterial," *Appl. Phys. Lett.*, 78, pp. 489–491, Jan. 2001.

[27] Pendry, J. B. (2004). Negative refraction. *Contemporary Physics*, *45*(3), 191-202.

[28] Wilson, J. D., "Wikimedia Commons via NASA Glenn Research Center," [Online]. Available: http://upload.wikimedia.org/wikipedia/commons/f/fb/Metarefraction.svg. [Accessed 22 03 2014].

[29] Sievenpiper, D., Zhang, L., Broas, R. F., Alexopolous, N. G., & Yablonovitch, E. (1999). High-impedance electromagnetic surfaces with a forbidden frequency band. *Microwave Theory and Techniques, IEEE Transactions on*, *47*(11), 2059-2074.

[30] Feresidis, A. P., Goussetis, G., Wang, S., & Vardaxoglou, J. C. (2005). Artificial magnetic conductor surfaces and their application to low-profile high-gain planar antennas. *Antennas and Propagation, IEEE Transactions on*, *53*(1), 209-215.

[31] Parker, E. A. (1991, April). The gentleman's guide to frequency selective surfaces. In *17th QMW Antenna Symposium* (pp. 1-18). London, UK, Queen Mary and Westfield College.

[32] Koschny, T., Markoš, P., Economou, E. N., Smith, D. R., Vier, D. C., & Soukoulis, C. M. (2005). Impact of inherent periodic structure on effective medium description of left-handed and related metamaterials. *Physical Review B*, *71*(24), 245105.

[33] Koschny, T., Kafesaki, M., Economou, E. N., & Soukoulis, C. M. (2004). Effective medium theory of left-handed materials. *Physical review letters*, *93*(10), 107402.

[34] Smith, D. R., Schultz, S., Markoš, P., & Soukoulis, C. M. (2002). Determination of effective permittivity and permeability of metamaterials from reflection and transmission

coefficients. *Physical Review B*, *65*(19), 195104.

[35] Singh, R., Lu, X., Gu, J., Tian, Z., & Zhang, W. (2010). Random terahertz metamaterials. *Journal of Optics*, *12*(1), 015101.

[36] Jacobsen, K. W., Norskov, J. K., & Puska, M. J. (1987). Interatomic interactions in the effective-medium theory. *Physical Review B*, *35*(14), 7423.

[37] Gollub, J., Hand, T., Sajuyigbe, S., Mendonca, S., Cummer, S., & Smith, D. R. (2007). Characterizing the effects of disorder in metamaterial structures. *Applied Physics Letters*, *91*(16), 162907.

[38] Karkkainen, K., Sihvola, A., & Nikoskinen, K. (2001). Analysis of a three-dimensional dielectric mixture with finite difference method. *Geoscience and Remote Sensing, IEEE Transactions on*, *39*(5), 1013-1018.

[39] Sihvola, A. H. (Ed.). (1999). *Electromagnetic mixing formulas and applications* (No. 47).

[40] Gittleman, J. I., & Abeles, B. (1977). Comparison of the effective medium and the Maxwell-Garnett predictions for the dielectric constants of granular metals. *Physical Review B*, *15*, 3273-3275.

[41] Doyle, W. T. (1989). Optical properties of a suspension of metal spheres. *Physical review B*, *39*(14), 9852.

[42] Feynman, R. P., Leighton, R. B.; Sands, M (1989). *Feynman Lectures on Physics*. Vol. 2, chap. 32 (Refractive Index of Dense Materials)

[43] Draine, B. T., & Goodman, J. (1993). Beyond Clausius-Mossotti-Wave propagation on a polarizable point lattice and the discrete dipole approximation. *The Astrophysical Journal*, *405*, 685-697.

[44] Ziolkowski, R. W., & Erentok, A. A metamaterial description of a volumetric artificial magnetic conductor. In *Proceedings of the 2004 URSI International Symposium on Electromagnetic Theory* (pp. 188-190).

[45] Rana, F. (2007, Fall). Lecture #25: Guided Waves in Parallel Plate Metal Waveguides. *ECE 303*. Lecture conducted from Cornell University, Ithica, NY

[46] Erentok, A., Luljak, P. L., & Ziolkowski, R. W. (2005). Characterization of a volumetric metamaterial realization of an artificial magnetic conductor for antenna applications. *Antennas and Propagation, IEEE Transactions on*, *53*(1), 160-172.

[47] Kern, D. J., Werner, D. H., Monorchio, A., Lanuzza, L., & Wilhelm, M. J. (2005). The design synthesis of multiband artificial magnetic conductors using high impedance frequency selective surfaces. *Antennas and Propagation, IEEE Transactions on*, *53*(1), 8-17.

[48] Lee, D., Erentok, A., & Ziolkowski, R. W. (2005, July). Integration of a Printed Dipole Antenna With a CLL-Based Volumetric Metamaterial AMC Block. In *Antennas and Propagation Society International Symposium, 2005 IEEE* (Vol. 2, pp. 2-5). IEEE.

[49] Uda, S., & Mushiake, Y. (1954). *Yagi-Uda Antenna*. Research Institute of Electrical Communication, Tohoku University.

[50] Balanis, C. A. (1997). *Antenna theory and design*.

[51] C. Wolff, "Radartutorial.eu: Yagi Antenna," [Online]. Available: http://www.radartutorial.eu/06.antennas/an08.en.html. [Accessed 01 04 2014].